Nonlinear mechanics of multimaterial thermoviscoelastic architected materials with snap-through instabilities

A Dissertation

Presented to

The Academic Faculty

by

Kaikai Che

In Partial Fulfillment

of the Requirements for the Degree

Doctor of Philosophy in the

George W. Woodruff School of Mechanical Engineering

Georgia Institute of Technology

December 2018

Nonlinear mechanics of multimaterial thermoviscoelastic architected materials with snap-through instabilities

Approved by: (pending approval)

Dr. Julien Meaud
Advisor, Committee Chair
School of Mechanical Engineering
Georgia Institute of Technology

Dr. H. Jerry Qi
School of Mechanical Engineering
Georgia Institute of Technology

Dr. Alper Erturk
School of Mechanical Engineering
Georgia Institute of Technology

Dr. Massimo Ruzzene
School of Aerospace Engineering
Georgia Institute of Technology

Dr. Julian Jose Rimoli
School of Aerospace Engineering
Georgia Institute of Technology

Date Approved: Aug. 24^{th}, 2018

Acknowledgements

I would like to express my deepest appreciation to my advisor, the committee chair Professor Julien Meaud, who have continuously provided support and help for the past four years. Dr. Meaud is one of the smartest people that I know. When I had difficulties encountered in my research, he can always provide valuable insights and directions for me to solve these problems. He is a serious, enthusiastic, and energetic scholar. From Dr. Meaud, I learnt the spirit of adventure in regard to research and scholarship. During the past month, he provided valuable review and discussions about this dissertation. Without his persistent help and insightful guidance, this dissertation would not have been possible all in one month.

I would like to thank Professor H. Jerry Qi for the use of the experimental facilities in his lab and discussions of my research. I wold also want to thank my committee members, Professor Alper Erturk, Professor Massimo Ruzzene and Professor Julian Jose Rimoli for their valuable discussions and suggestions about this dissertation.

I want to thank Kashyap Alur for the help of python scripts, Jiangtao Wu and Chao Yuan for the help of 3D printing, MTS experiments and their useful discussions. I would like to thank Elisa Boatti for the help with MTS/TestWorks and the software for the video processing. I also want to thank the members of the lab, Charlsie Lemons, Thomas Bowling and Haiqi Wen for the valuable discussions and advices during the group meetings.

I also thank my friends for providing support. I deeply thank my parents, sisters and my girlfriend. Without their consistent support, I would not be able to finish my graduate study. I love them so much.

Table of Contents

List of Tables

List of Figures

Summary

Architected materials have unusual and interesting properties that are typically unachievable using conventional materials. Many researchers have previously focused on the design and analysis of architected materials with snap-through instabilities. This thesis aims to investigate the influence of geometric parameters, temperature and time on the snap-through buckling of one-dimensional (1D) thermoviscoelastic architected materials for applications as reconfigurable architected materials. Rigorous theoretical models of a unit cell with snap-through instabilities are first developed for both the cases of elastic and thermoviscoelastic constitutive models. These theoretical models are utilized to analyze the influence of geometric design, temperature and strain rate on the mechanics of the unit cell. With the understanding of the nonlinear mechanics of the unit cells, strategies (such as introducing small geometric variations in the unit cell design or varying the temperature) are proposed and implemented to tune the snapping sequences of architected materials made of unit cells with snap-through instabilities. With the help of the theoretical model, FEA simulations and experiments, temperature is utilized to tune the snapping sequence of these multimaterial architected materials after their fabrication. Furthermore, it is shown that a time-dependent snapping behavior can be observed in a viscoelastic architected material that has snap-through instabilities. The influence of geometric parameters and temperature on this time-dependent snapping is analyzed. The results provide fundamental understandings of interesting mechanical response that depends on time and temperature, which could help to design and develop reconfigurable and programmable architected materials with tunable

properties.

Chapter 1

Introduction

1.1 Overview

Smart materials whose material properties and architectures can be reconfigurable are the focus of active studies[1,4,2,5]. This dissertation concentrates on one new type of reconfigurable architected material, which is a multilayer viscoelastic architected material with snap-through instabilities. In order to better understand the nonlinear mechanics of this type of architected materials with thermo-viscoelastic material, the mechanics of architected materials with elastic constituent model was analyzed as the first step. With the help of a theoretical model and FEA simulations, the relationship between applied force and deformation of elastic architected materials with snap-through instabilities was established. The configuration switching in these materials was studied and tuned by geometric variations, which was validated by experiments on 3D printed samples. With these understandings about this architected material with elastic material, a theoretical model with viscoelastic constitutive model was further developed to study the effects of viscoelasticity on the mechanical response of these architected materials. Parameters of temperature and geometric design were employed to control and tune the buckling response of these architected materials. Moreover, the time-dependent snapping of a single layer viscoelastic architected

material was also investigated. The understanding about the buckling properties of these architected materials with snap-through instabilities paves a way for researchers to design new reconfigurable and switchable architected materials for novel applications.

1.2 Background

1.2.1 Architected materials

The techniques of additive manufacturing have enabled and facilitated the design and analysis of structures with a periodic architecture (often called architected materials or metamaterials)[9]. Their effective properties are not derived from the intrinsic bulk properties of the constituent materials, but from the newly designed microarchitecture[10]. The periodicity of architected materials enables some uncommon properties that are not seen in natural or conventional materials[11,12]. For example, acoustic architected materials can exhibit unusual acoustic behavior, such as the ability to guide or stop elastic wave propagation along a desired path[13,14,15,16]. Other interesting and unconventional properties of architected materials include negative bulk modulus[17,18,19,20], negative Poisson's ratio[21,22,23,24,25], high specific energy absorption[26,27,28,29,4,30,31], or negative (dynamic) mass[17,20,32,33].

However, the functionality of an architected material is limited if its properties are not tunable after its fabrication. Some recent studies have developed tunable architected materials by exploiting elastic instabilities that can cause configurational changes in the microarchitecture of these architected materials[34]. Buckling and post-buckling problems have been studied for decades[35,36], but it has only been used recently to enhance architected materials' functionality by introducing reversible and repeatable configurational changes. For example, Mullin *et al.*[37] utilized reversible elastic instabilities to cause pattern transformation for one designed periodic structure with circular holes. Under uniaxial compression loading, the structure can have a dramatic configuration transformation even with very small strain change. This property provides the materials' opportunity in applications as optical switches.

The reconfiguration and buckling of various types of architected materials and cellular materials have been studied. For example, Bertoldi *et al.*[38] systematically analyzed the mechanics of deformation-induced configuration transformations for periodic structures with holes of different shapes. Recently, it has been shown that honeycombs, one of the most commonly studied architecture for 2D cellular materials[35], have a very diverse range of buckling modes depending on the geometry of the unit cell (triangular, rectangular, hexagonal, etc), direction of the applied loads and level of hierarchy[39,40]. Pal *et al.*[41] developed a continuum model to analyze phase transitions for a 2D hexagonal lattice under large deformations. Rimoli and Pal[42] also studied the mechanics of 3D tensegrity lattices from truncated octahedron unit cells. With nonlinear geometric effects and buckling related to the unit cell, their design demonstrated high strength with low density.

These interesting pattern transformations introduced by elastic instabilities have found applications as tunable acoustic metamaterials[40] and auxetic materials[43]. For example, Bertoldi and Boyce[44,45] studied the wave propagation properties of a type of elastomeric materials with periodic holes. The results demonstrated that the materials' pattern transformations triggered by elastic instabilities are able to tune and change bandgaps. Besides potential applications in wave propagation, this type of periodic microstructure with holes also exhibits a negative Poisson's ratio because of a pattern transformation induced by elastic instabilities[46]. By exploiting buckling to induce pattern transformation, Babaee *et al.*[22] and Liu *et al.*[47] designed different types of metamaterials that also demonstrate auxetic behavior. With phase transitions caused by buckling, Pal *et al.* and Salahshoor*et al.* also investigated the wave propagation[48] and material symmetry[49] in 3D tensegrity metamaterials. Many other researchers also utilized reversible changes in the microarchitecture geometry due to elastic instabilities to design structures that are able to tune the bandgaps in acoustic[50,51,52,53,54] and photonic[55,56] metamaterials. All these previous studies give valuable insights about the mechanics and potential application of reconfigurable architected materials with elastic instabilities. However, most of the designs require external load to

maintain the deformed configurations. Due to this, the functionality of these reconfigurable metamaterials may be limited for certain practical situations. Thus, it is necessary to exploit some approaches, like shape memory effect[57] or multistability[54,58] to design a reconfigurable material that can remain in a deformed configuration after removal of external stimulus.

Besides elastic instabilities, different types of stimuli, like temperature[59], magnetic field[60,61], or ambient pressure[62] have been used to tune reconfigurable architected materials to obtain multifunctional properties. Moreover, some researchers[63,64] utilized water to actuate the geometric reconfigurations of 3D printed materials. All these studies reveal important findings about reconfigurable materials.

1.2.2 Architected materials with snap-through instability

While there are many approaches to obtain reconfigurable architected materials, this work focuses on reconfigurable architected materials with snap-through instabilities. A snap-through instability is a kind of elastic instability in which a structure instantaneously jumps from one configuration to another configuration when an applied stimulus reaches a critical level[65]. This kind of snap-through behavior is related to a unstable region of negative stiffness, which does not resist but actually assists the deformation[66]. The fundamental mechanics and potential applications of snap-through instabilities have been studied for a long time[67,68,69,70]. Using modal superposition method, Qiu *et al.*[69] developed a theoretical model and analyzed the relationship between applied force and deformation of a initially curved beam. They derived the corresponding mathematical expressions to describe the relationship between force and deformation. Interestingly, the results show that the force-deformation relation is only dependent on one geometric constant Q, which is the ratio between the initial height (h in Fig. 1.1a) and thickness (t in Fig. 1.1a) of the beam. Based on different values of Q, a clamped-clamped beam as shown in Fig. 1.1a can be monostable, *i.e.* it returns to its undeformed configuration after removal of the load, or bistable, *i.e.*, it has two states corresponding to a local minimum in the strain energy such that the element

can remain in a deformed configuration even after removal of the load. The differences between these two types of elements are clearly demonstrated by their force vs displacement and strain energy vs displacement curves (Fig. 1.1b-c). From Fig. 1.1b, the unstable region of negative stiffness is from point I to point II. If the element is compressed in a force control manner, it would jump from the local peak in the force (point I, referred as critical force) to the point with the same force value (point III). This means the system cannot follow the static equilibrium path and has to jump to the stable region where it can bear loading above the critical force. The two equilibrium positions of a bistable element are shown as point ① and ② in Fig. 1.1b (where $f = 0$, $du/dd = 0$); while for a monostable element, there is only one local equilibrium position shown as point ① in Fig. 1.1c.

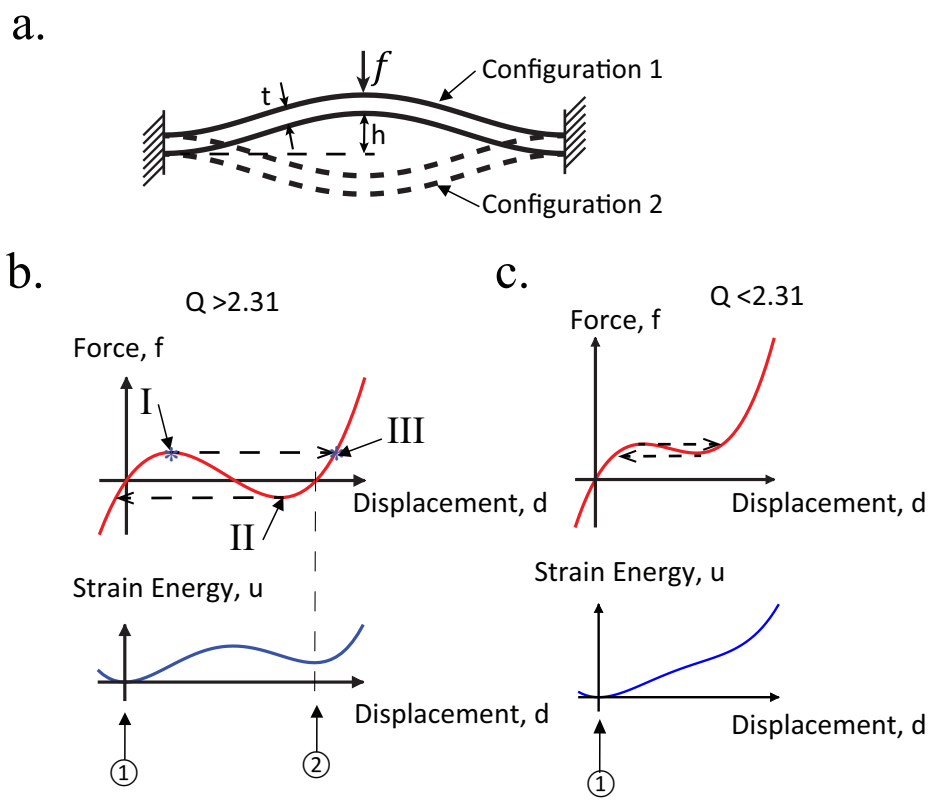

FIG. 1.1. a. A clamped-clamped beam element, dashed lines represent the other configuration of this beam. b. Force vs displacement and strain energy vs displacement for a bistable element (points ① and ② are stable equilibrium positions correspond to minima in the strain energy). c. Force vs displacement and strain energy vs displacement for a monostable element (point ① is a stable equilibrium position corresponds to a minimum in the strain energy).

Many new designs of architected materials with snap-through instability have been proposed and analyzed[4,3,1,71,2]. For example, Restrepo *et al.*[1] (Fig. 1.2a) and Correa *et al.*[3] (Fig. 1.2c) developed architected materials that are made up of multiple unit cells that each includes an initially curved beam. Through the elastic snap-through of a high number of unit cells arranged in series, this kind of architected material can exhibit large hysteresis loops in response to cyclic loads. Because of these hysteresis loops, these architected materials dissipate a large amount of mechanical energy. In contrast to traditional honeycombs that rely on plastic energy dissipation, the deformation can be fully recovered in these architected materials. While some of the proposed architected materials with snap-through instabilities are monostable (for example the negative stiffness honeycombs designed by Correa *et al.*[3]), other designs are multistable, *i.e.*, they have multiple stable configurations obtained because their building blocks are bistable. For example, Shan *et al.*[4] (Fig. 1.2d) developed multistable architected materials using bistable tilted beams. These architected materials can achieve large deformations and offer significant energy absorption capacity due to the ability of the material to trap elastic energy in a stable deformed configuration in response to an impact. Haghpanah *et al.*[2] (Fig. 1.2b) investigated another design for multistable architected materials, based on bistable structural elements designed to be considerably stronger than previous designs. Frenzel *et al.*[5] (Fig. 1.2e) designed a programmable reusable light-weight shock absorber that can either self-recover or have multiple stable equilibria by utilizing the inner elements' buckling. While these previous studies focus on multistable architected materials in response to compressive loads, Rafsanjani et al.[71] showed that the design of architectures that exhibit multistability in response to tensile loads is possible. Wu *et al.*[72] presented modular, engineered structures that have multiple stable states. They systematically discussed the the parameters that can be used to tailor the structures' functionality. Ren *et al.*[6] designed and analyzed architected materials with similar curved beam as in the research of Qiu *et al.*[69], Restrepo *et al.*[1] and Correa *et al.*[3]. In this research, they explored unidirectional, bidirectional and tridirectional metamaterials with negative stiffness (Fig.

1.2f). They theoretically and numerically investigated the the architected materials' quasi-static and dynamic response behavior. The results demonstrated the potential application of these architected materials in energy absorption and vibration isolation.

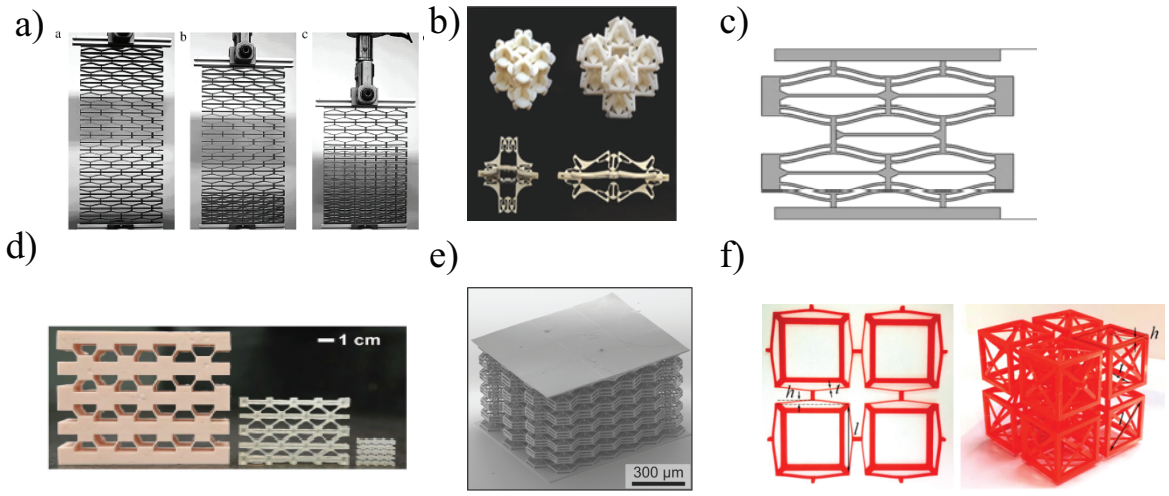

FIG. 1.2. Architected materials with snap-through instability. a) Restrepo et al., 2015[1]. b)Haghpanah et al., 2016[2]. c) Correa et al., 2015[3]. d) Shan et al., 2015[4]. e) Frenzel et al., 2016[5]. f) Ren et al., 2018[6]. (Reuse permissions obtained from providers.)

Materials with periodic structures could have important applications in wave propagation. These materials are commonly called acoustic metamaterials or phononic materials[73]. Compared with traditional phononic materials that cannot be changed after fabrication, reconfigurable phononic materials could be used to switch the direction of wave propagation[74,75] and reversibly tune the bandgaps[52]. Many researchers utilized elements with snap-through instability to design phononic materials and study their wave propagation properties[76,77,78,54,79]. For example, Nadkarni *et al.*[76] studied the wave propagation properties of a periodic chain consisting of bistable elements. Using analytical and numerical solutions, they demonstrated that three different regimes of wave propagation exist depending on the wave amplitudes. In response to large wave amplitude, interesting nonlinear phenomena are observed, such as unidirectional propagation of transition waves[80] or the ability of waves to propagate over large distances despite the presence of dissipation mechanisms[77]. Frazier and Kochmann[78] recently showed that nonlinear waves of sufficiently large amplitude

can propagate and transmit energy within the linear band gap frequencies of 1D chains of bistable elements. Meaud and Che[54] demonstrated that multistable architected materials can be used as reconfigurable phononic crystals with broadband phononic band gaps; switching from one stable configuration to another one allows to switch on/off the propagation of elastic waves. One advantage of reconfigurable metamaterial made of bistable unit cells is that the system is able to remain in a deformed stable configuration after removal of the external stimulus. With similar unit cells as in Correa *et al.*[3], Goldsberry and Haberman[79] studied the wave propagation of a negative stiffness honeycomb. Their results showed that this kind of negative stiffness honeycomb exhibits high tunability and anisotropy because of switchable configurations induced by buckling instabilities.

1.2.3 Mechanical properties of polymers

As in many of the previously mentioned works on architected materials[31,55,71], the considered architected materials in this work are fabricated using polymers. Unlike elastic materials whose stress-strain relationship is not related to temperature, polymers are thermoviscoelastic materials, which are not only temperature-dependent, but also time-dependent[81]. Under cyclic loading, hysteresis loop is observed in a polymer's stress-strain curve (as shown in Fig. 1.3a). When a polymer is applied a small harmonic oscillating stress, the measured resulting strain will exhibit some lag due to viscoelastic effects. The stress $\sigma(t)$ and strain $\epsilon(t)$ are expressed as the following expressions[82],

$$\sigma(t) = \sigma^* e^{i\omega t} \tag{1.1}$$

$$\epsilon(t) = \epsilon^* e^{i\omega t} = |\epsilon^*| e^{i(wt-\delta)} \tag{1.2}$$

where $i^2 = -1$, ω is the angular frequency, σ^* is the complex magnitude of stress, ϵ^* is the complex magnitude of strain, and δ is the phase shift between stress and strain.

This renders a complex dynamic modulus E^*, which is expressed as the following expression,

$$E^* = \frac{\sigma^*}{\epsilon^*} = E' + iE'' \tag{1.3}$$

where E' is the storage modulus (measure of the energy stored), and E'' is the loss modulus (measure of the energy lost). The tangent of the phase shift δ between stress $\sigma(t)$ and strain $\epsilon(t)$ (called the loss tangent or loss factor) can be expressed as,

$$\tan\delta = \frac{E''}{E'} \tag{1.4}$$

Creep and relaxation are two transient properties of viscoelastic materials[82]. Creep corresponds to an increase of the strain in viscoelastic material over time when a step of constant stress is applied. Relaxation corresponds to a time-dependent decrease of stress in viscoelastic materials when a step constant strain with amplitude ϵ_0 is applied (as shown in Fig. 1.3b). The relaxation modulus is defined as the ratio between stress and strain, which can be expressed as,

$$E(t) = \frac{\sigma(t)}{\epsilon_0} \tag{1.5}$$

where $\sigma(t)$ is the stress, and ϵ_0 is the magnitude of the step strain.

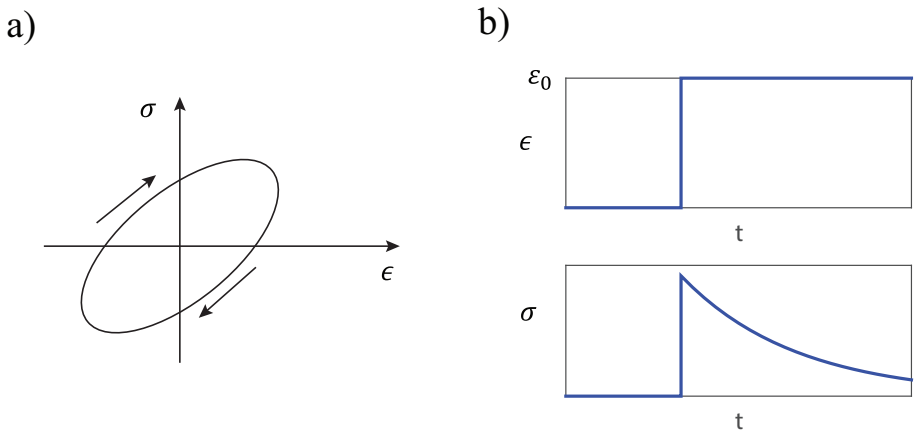

FIG. 1.3. a) Hysteresis loop of linear viscoelastic materials b)Viscoelastic materials' transient property Relaxation: stress and strain versus time.

The storage modulus, loss modulus and $\tan\delta$ can be characterized by Dynamic Material Analysis (DMA) through applying a sinusoidal deformation to the material at a single or at multiple frequencies, and recording the material's response. One DMA result of a polymer DM9895 (one material that was used in this research)[83] is shown in Fig. 1.4a-b. As shown in Fig. 1.4a, the storage modulus decreases and the material becomes softer as temperature increases. As demonstrated in Fig. 1.4c, due to the relaxation of the viscoelastic polymer, the relaxation modulus drops as time passes. Moreover, with higher temperature, the relaxation modulus decreases faster. The temperature and time-dependent properties of polymers offer opportunities for tunability in architected materials, in which modulus could be tuned by temperature or strain rate (meaning the stiffness of these materials can be tailored) .

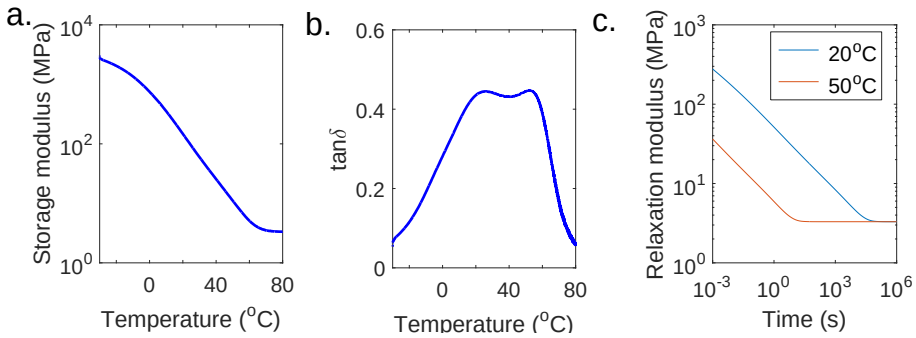

FIG. 1.4. a. Storage modulus vs temperature of DM9895. b. *tanδ* vs temperature of DM9895. c. Relaxation modulus vs time of DM9895 at two different temperatures. (The frequency used in DMA test is 1Hz)

The shape memory effect is another important property of polymers. Shape memory polymers are able to memorize temporary shapes and return to their initial shapes with exposure of external stimuli, such as temperature[83], pressure[84], light[85] or magnetic field[86]. Since its discovery, it has been used in a wide range of applications, such as self-folding structures[63], smart robot[87], biomedical devices[88,89]. For thermal shape memory polymers, Fig. 1.5 gives the process (heating, deformation, cooling) of shape memory effects. The polymer initially stays at its permanent shape after fabrication. An external force is applied at a temperature above the glass transition temperature, T_g (the temperature at which polymer experiences transition from a hard 'glassy' state into a viscous or rubbery state[90])

to deform the polymer. After being deformed, the polymer is cooled to lower temperature to locked the temporary shape. When the polymer is heated at temperature over T_g, it will recover to its memorized initial shape. Some researchers utilized shape memory effects in polymers to lock the buckled shape of architected materials by mechanical loading then release such locked shape[57,87]. While the polymers used in this research are shape memory polymers, the shape memory effect is not exploited; the results of this research are based on the fact that the stiffness of polymer is temperature and time-dependent.

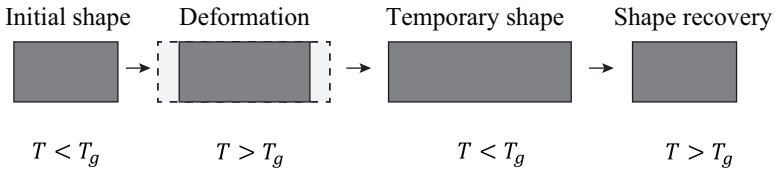

FIG. 1.5. Schematic of shape memory effect.

1.2.4 Buckling of viscoelastic composites and architected materials

Buckling of viscoelastic materials is more complex than elastic materials due to the time-dependent and temperature-dependent properties of polymers. For example, elastic architected materials with snap-through instabilities are either bistable or monostable. However, the distinction between monostable and bistable behaviors becomes blurry for the case of viscoelastic architected materials. Because of the time-dependent property, a viscoelastic structure can be pseudo-bistable[91], which means the structure will remain in a nominally unstable equilibrium before returning back to its initial state after certain time period. The advantage of these pseudo-bistable structures is that it removes the actuation requirement to return to its original configuration. Using pseudo-bistability, programmable self-recovery structures were designed and analyzed based on structures with snap-through instabilities. For example, Santer[7] demonstrated that there is a temporary stable state for a hemispherical cap in deformed configuration. Due to the material's viscoelasticity effect, this temporary bistability may be lost after certain time and the structure suddenly jumps to the initial configuration (see Fig. 1.6a). Brinkmeyer *et al.*[91] investigated the pseudo-bistability phe-

nomenon in a spherical dome by FEA simulations (see Fig. 1.6b) and experiments . Then Brinkmeyer *et al.*[8] employed a discrete truss model to systematically analyze the principles of pseudo-bistability phenomenon and study the effects of geometry and boundary condition on the pseudo-bistability, especially their influence on the recovery time.

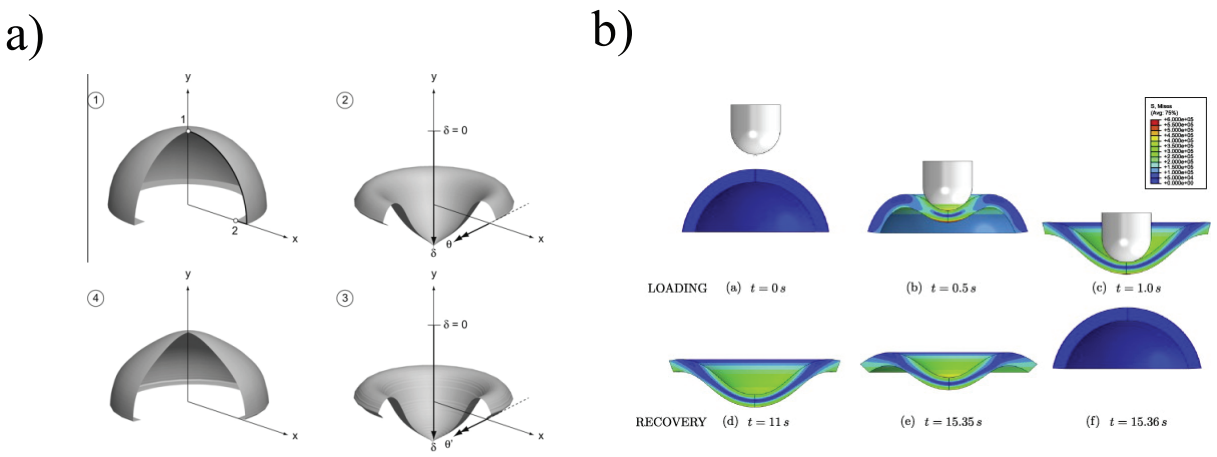

FIG. 1.6. Examples with pseudo-bistability. a) Santer, 2010[7]. b) Brinkmeyer *et al.*, 2012[8].

Beside the time-dependent buckling of viscoelastic materials, previous work has also shown that the buckling of viscoelastic materials is rate-dependent. Huang and Suo developed theoretical models for the buckling modes and growth rate for wrinkling instabilities of a compressed elastic film on a viscous layer[92,93]. Alur *et al.* analyzed the finite deformation mechanics of viscoelastic layered composites that consist of alternating layers of a stiff elastic constituent and layers of a soft viscoelastic constituent[94,95]. The numerical results from[94,95] and experiments from[96] demonstrate that the buckling modes of viscoelastic layered composites can switch from a wrinkling mode to a longwave buckling instability as the strain rate is varied.

1.3 Objectives and outline

These previous works all provide important understandings on the mechanics of architected materials with snap-through instabilities and give valuable insights about time-dependent

and rate-dependent properties of buckling in viscoelastic materials. This work mainly aims to obtain controllable and programmable architected materials with switchable configurations and to study the parameters that can influence the configuration switching of the architected materials with snap-through instabilities. With reconfigurable properties and negative stiffness, these kind of architected materials may have many interesting and promising applications in energy absorption and impact absorber. Moreover, due to pseudo-bistability behavior, these materials can be employed to design self-deployed robots used in aerospace engineering or bio-medicine fields. Also these materials can be utilized as phononic and acoustic materials to tune and guide wave propagation.

The objective of my work is to study the fundamental mechanics of one kind of tunable thermoviscoelastic architected materials with snap-through instabilities. This study would help to expedite the applications of this novel material design. Most of previous work on architected materials with snap-through instabilities have not considered the influence of viscoelasticity. However, 3D printing using viscoelastic polymers is commonly used to fabricate architected materials. This dissertation addresses the following research questions: What is the effects of viscoelasticity on the materials' response of 3D printed designs? How can temperature and time affect the buckling of these architected materials? Can a general design criterion generated for the mechanical response in these archtected materials with snap-through instabilities? In order to answer these questions, theoretical models of a unit cell with both elastic constitutive model and viscoelastic constitutive model were developed to help to study the buckling mechanics of architected materials with snap-through instabilitie. Based on the understandings of the mechanics of the unit cell, the snapping response of architected materials made of these unit cells with snap-through instabilities was further investigated. The controlling parameters that can be utilized to tune the mechanical response of these architected materials were identified and analyzed. The results from analytical model were validated by FEA simulations and experiments.

This dissertation is organized as the following:

Chapter II describes the theoretical model of architected materials with snap-through instabilities for both elastic material case and thermoviscoelastic material case.

Chapter III discusses the design and mechanics of elastic architected materials with a deterministic snapping sequence. In this section, some variations in the geometric parameters of unit cells are utilized to tune the snapping sequence of architeced materials with snap-through instabilities.

Chapter IV presents viscoelastic multistable architected materials with temperature-dependent snapping sequence. In this section, a novel concept of mutimaterial viscoelastic architected materials is proposed. The snapping sequence of this mutimaterial architected materials is tuned by temperature.

Chapter V analyzes time-dependent snapping of thermoviscoelastic architected materials with snap-through instabilities. The conditions for observing pseudo-bistable behavior within a single layer of pseudo-bistable unit cells with viscoelastic material is studied.

Chapter VI gives the summary of this dissertation and proposes a few directions for future work.

Chapter 2

Mechanics of unit cells with snap-through instabilities

2.1 Introduction

The specific kind of architected materials that were investigated in this thesis is shown in Fig. 2.1a. The architected material is made up of multiple unit cells (that are similar to the building block in the works of Restrepo *et al.*[1] and Correa *et al.*[3]). The geometrical parameters of each unit cell are shown in Fig. 2.1b. The unit cell consists of thick horizontal and vertical elements and a thin curved part. Due to the presence of an unstable regime of negative stiffness (as discussed in Section 1.2.2 of Chapter 1), this kind of architected material exhibits snap-through instabilities once the applied force reaches a critical value under force control condition. Similarly to previous studies[4,1], these architected materials are called one-dimensional (1D) architected materials because the loading is intended to be only in the y-direction.

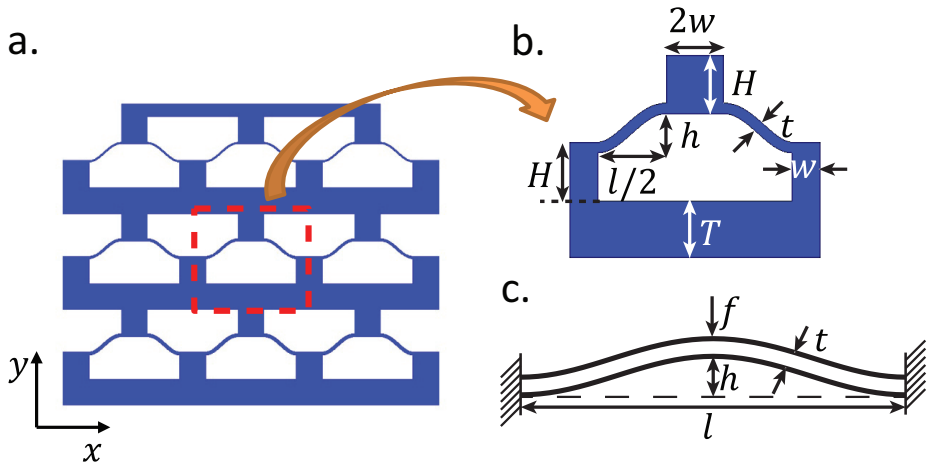

FIG. 2.1. Schematic of 1D architected material. a. An example of a 1D architected material with 3 rows, each with 3 unit cells. b. Geometrical parameters of a single unit cell. c. Simplified clamped-clamped beam model of the unit cell (a transverse force, f, is applied at the midpoint of the beam).

In order to have a better understanding of the nonlinear mechanics of this kind of architected materials, a rigorous theoretical model of the unit cell was first developed. The first developed model is based on a elastic constitutive model; while this model ignores the viscoelasticity of 3D printed materials, it gives considerable insight into the mechanics of these architected materials. With the understanding of analytical model with elastic material, a more complex theoretical model for the unit cell with thermoviscoelastic material was then developed. In this chapter, these theoretical models of the unit cells are presented for both an elastic and thermoviscoelastic constitutive models.

2.2 Theoretical model of unit cell with elastic constitutive model

2.2.1 Theory

2.2.1.1 Governing equation

The analytical model of the unit cell is established based on the model of Qiu *et al.*[69], developed for a single initially curved beam. The curved part of the unit cell is modeled as an initially curved clamped-clamped Euler-Bernoulli beam, while other parts of the unit cell are assumed to be rigid (Fig. 2.1c). A transverse force, f, is applied at the midpoint of the beam. The governing equation for this beam is:

$$EI\left(\frac{d^4w}{dx^4}-\frac{d^4w_0}{dx^4}\right)+p\frac{d^2w}{dx^2}=-f\delta(x-\frac{l}{2}) \tag{2.1}$$

where w is the lateral deflection of the beam, $w_0(x)$ is the initial shape of the beam , E is the Young's modulus, I is the area moment of inertia of the beam, p is the compressive force, l is the beam span (Fig. 2.1b) and δ is the Dirac delta function.

The compressive force, p, is caused by the shortening of the beam total length and is given by

$$p=-EA\frac{\Delta s}{s_0} \tag{2.2}$$

where A is the cross-section area of the beam, Δs is the change in the beam length and s_0 is the initial beam length. The following approximations, valid for $\frac{dw}{dx} << 1$ and $\frac{dw_0}{dx} << 1$, are used:

$$\begin{aligned}\Delta s &= \int_0^l \frac{1}{2}\left[\left(\frac{dw}{dx}\right)^2-\left(\frac{dw_0}{dx}\right)^2\right]dx \\ s_0 &= l\end{aligned} \tag{2.3}$$

Due to the presence of the compression force, the governing equation in Eq. 2.1 is a nonlinear differential equation.

2.2.1.2 Initial shape of the curved part in the unit cells

While the model of Qiu *et al.*[69] did not consider the presence of imperfection and assumed that the initial shape of the curved beam only consists of the first buckling mode, higher mode imperfections (which could be caused by imperfections in the 3D printing process) were considered in this thesis.

In the case of the model without any mode imperfection, $w_0(x)$ is given by:

$$w_0(x) = \frac{h}{2} W_1(x) \tag{2.4}$$

where h is the initial apex height of the beam and $W_1(x) = 1 - \cos(2\pi x/l)$ is the first buckling mode of a clamped-clamped Euler-Bernoulli beam.

In the case of the model with higher mode imperfection, $w_0(x)$ is given by:

$$w_0(x) = \frac{h}{2} W_1(x) + \delta W(x) \tag{2.5}$$

where $\delta W(x)$ is the mode shape imperfection, which is prescribed to be given by

$$\delta W(x) = a_3 \frac{h}{2} W_3(x) \tag{2.6}$$

where $W_3(x) = 1 - \cos(4\pi x/l)$ is the third buckling mode of a clamped-clamped beam and a_3 is the mode imperfection size. The case of a model without imperfection corresponds to $a_3 = 0$, such that the model with mode imperfection is a generalization of the model without imperfection.

2.2.1.3 Solving the governing equation

The lateral deflection of the beam at the beam midpoint, d, is given by,

$$d = w_0(l/2) - w(l/2) \tag{2.7}$$

Since d corresponds to the change in the height of the unit cell when the transverse load is applied, we will refer to d as the deformation of the unit cell. The deflection of beam is decomposed into the sum of the buckling modes shapes for an initially straight clamped-clamped beam, $W_i(x)$:

$$w(x) = \sum_{i=1}^{\infty} A_i W_i(x) \tag{2.8}$$

where the expression of $W_i(x)$ is given in[69] as:

$$\left.\begin{aligned} W_i(x) &= 1 - \cos(N_i \tfrac{x}{l}) \\ N_i &= (i+1)\pi \end{aligned}\right\} i = 1, 3, 5, \ldots$$

$$\left.\begin{aligned} W_i(x) &= 1 - 2\tfrac{x}{l} - \cos(N_i \tfrac{x}{l}) + \tfrac{2}{N_i}\sin(N_i \tfrac{x}{l}) \\ N_i &= 2.86\pi, 4.92\pi, \ldots \end{aligned}\right\} i = 2, 4, 6, \ldots$$

and system of nonlinear equations for the modal amplitudes, A_i, can be obtained by a variational method. The variation of the total potential energy $\partial\pi$ is given by,

$$\partial\pi = \partial U_b + \partial U_c - \partial U_f \tag{2.9}$$

where ∂U_b, ∂U_c and ∂U_f are the variations in the bending strain energy, compression strain energy, and potential energy of the external force, respectively. These variations are given

by,

$$\begin{aligned}
\partial U_b &= \partial \left[\int_0^l \frac{EI}{2} \left(\frac{d^2w}{dx^2} - \frac{d^2w_0}{dx^2} \right)^2 dx \right] \\
\partial U_c &= -p\partial \Delta s \\
\partial U_f &= f\partial d
\end{aligned} \tag{2.10}$$

The following normalizations from [69] are introduced:

$$\begin{aligned}
\overline{x} = \frac{x}{l}, \quad \overline{w}(\overline{x}) = \frac{w(x)}{h}, \quad \overline{f} = \frac{fl^3}{EIh}, \quad \overline{d} = \frac{d}{h}, \quad B_i = \frac{A_i}{h}, \\
\overline{p} = \frac{pl^2}{EI}, \quad \overline{U}_b = \frac{U_b l^3}{EIh^2}, \quad \overline{U}_c = \frac{U_c l^3}{EIh^2}, \quad \overline{\pi} = \frac{\pi l^3}{EIh^2}.
\end{aligned} \tag{2.11}$$

Using Eqs. 2.2, 2.7, 2.8, and 2.11, the normalized deformation, $\overline{d}$, and the normalized compression force, $\overline{p}$, can be expressed as a function of the normalized modal amplitudes, B_i:

$$\overline{d} = 1 - 2 \sum_{i=1,5,9,13.,\ldots} B_i \tag{2.12}$$

$$\overline{p} = 12Q^2 \left[\frac{N_1^2 + a_3^2 N_3^2}{16} - \sum_{i=1}^{\infty} \frac{B_i^2 N_i^2}{4} \right] \tag{2.13}$$

where $Q = h/t$. Moreover, the variation in the total potential energy, $\partial\overline{\pi}$, can be expressed as:

$$\begin{aligned}
\partial\overline{\pi} = &\left(\frac{N_1^4 - \overline{p}N_1^2}{2} B_1 - \frac{N_1^4}{4} + 2\overline{f} \right) \partial B_1 \\
&+ \left(\frac{N_2^4 - \overline{p}N_2^2}{2} B_2 \right) \partial B_2 \\
&+ \left(\frac{N_3^4 - \overline{p}N_3^2}{2} B_3 - \frac{a_3 N_3^4}{4} \right) \partial B_3 \\
&+ \sum_{i=4,6,7,\ldots} \left(\frac{N_i^4 - \overline{p}N_i^2}{4} \right) \partial B_i^2 \\
&+ \sum_{i=5,9,13,\ldots} \left(\frac{N_i^4 - \overline{p}N_i^2}{2} B_i + 2\overline{f} \right) \partial B_i
\end{aligned} \tag{2.14}$$

The theorem of minimum potential energy, $\partial\overline{\pi} = 0$, leads to the following system of nonlinear equations:

$$\begin{aligned}
\left(\frac{N_1^4 - \overline{p}N_1^2}{2}B_1 - \frac{N_1^4}{4} + 2\overline{f}\right)\partial B_1 = 0 \\
\left(\frac{N_2^4 - \overline{p}N_2^2}{2}B_2\right)\partial B_2 = 0 \\
\left(\frac{N_3^4 - \overline{p}N_3^2}{2}B_3 - \frac{a_3 N_3^4}{4}\right)\partial B_3 = 0 \\
\left(\frac{N_i^4 - \overline{p}N_i^2}{2}\right)B_i \partial B_i = 0 \text{ for } i = 4, 6, 7, ... \\
\left(\frac{N_i^4 - \overline{p}N_i^2}{2}B_i + 2\overline{f}\right)\partial B_i = 0 \text{ for } i = 5, 9, 13, ...
\end{aligned} \tag{2.15}$$

For the theoretical model of the initially curved beam, the second mode is constrained, *i.e.* only symmetric solutions were considered (because it is observed that the deformation mode of the unit cell is almost symmetric in FEA simulations), such that $B_2 = 0$.

Model with a third mode imperfection

With a 3^{rd} mode imperfection ($a_3 \neq 0$), there is only one form of solutions. The normalized modal amplitudes are given by:

$$\begin{aligned}
B_1 &= -\frac{1}{2}\frac{N_1^2}{\overline{p} - N_1^2} + \frac{4\overline{f}}{N_1^2(\overline{p} - N_1^2)} \\
B_3 &= -\frac{1}{2}\frac{a_3 N_3^2}{\overline{p} - N_3^2} \\
B_i &= \frac{4\overline{f}}{N_i^2(\overline{p} - N_i^2)}, \quad i = 5, 9, 13, \ldots \\
B_i &= 0, \quad \text{for other } i \text{ values}
\end{aligned} \tag{2.16}$$

From Eqs. 2.13 and 2.16, a quadratic equation for the normalized force, $\overline{f}$, can be derived as,

$$\alpha\overline{f}^2 + \beta\overline{f} + \gamma = 0 \tag{2.17}$$

where

$$\alpha = \sum_{i=1,5,9,13...} \frac{4(\overline{p} - N_1^2)^2}{N_i^2(\overline{p} - N_i^2)^2}$$
$$\beta = -N_1^2 \tag{2.18}$$
$$\gamma = \frac{\overline{p}(\overline{p} - N_1^2)^2}{12Q^2} - \frac{N_1^2\overline{p}(\overline{p} - 2N_1^2)}{16} + \frac{a_3^2\overline{p}(2N_3^2 - \overline{p})N_3^2(\overline{p} - N_1^2)^2}{16(\overline{p} - N_3^2)^2}$$

In order to obtain the normalized force vs normalized deformation curve, a vector is first formed for the normalized compression force, $\overline{p}$. Eq. 2.17 is solved for each entry of this vector. If the discriminant of Eq. 2.17, Δ, is negative, it means that the value of the normalized compression force is impossible. If Δ is positive, then two roots are obtained for the normalized force, $\overline{f}$. For each of these roots, the mode coefficients B_i can be obtained from Eq. 2.16 and the normalized deformation can be derived from Eq. 2.12. Thus, the value of normalized force can be plotted as a function of the normalized deformation for each root. Connecting the points obtained for each entry of the vector for $\overline{p}$ that corresponds to $\Delta > 0$, a curve $\overline{f}$ vs $\overline{d}$ is obtained for each of the two families of roots; these two curves converge to the point that corresponds to $\Delta = 0$. A single normalized force vs normalized deformation curve is obtained by connecting the two curves.

Model without imperfections

If there is no 3^{rd} mode imperfection ($a_3 = 0$), then the solutions are comprised of two forms of solutions.

- Solution 1: if $\overline{p} < N_3^2$, a solution of the same form as the case $a_3 \neq 0$ is obtained. The equations obtained in the general case can be applied by setting $a_3 = 0$.

- Solution 2: If $\overline{p} = N_3^2$, then another form of solution is obtained. In that case, the value of B_3 cannot be found directly using Eq. 2.15 while the values of all other B_i are the same as in the case $a_3 \neq 0$. Using Eq. 2.12 and the equation $\overline{p} = N_3^2$, a linear

equation that relates the normalized force, $\overline{f}$, and the normalized deformation, $\overline{d}$, is obtained:

$$\overline{f} = -\frac{-\frac{N_1^2}{N_3^2-N_1^2} + \overline{d} - 1}{\sum_{i=1,5,9,13...} \frac{1}{N_i^2(N_3^2-N_i^2)}} \tag{2.19}$$

In the model without imperfections, the normalized force vs normalized deformation curve is obtained by connecting the two forms of solutions, as described in[69]. After solving these equations, the relationships between force and deformation, strain energy and force can be derived.

2.2.2 Validation of the theoretical model of elastic unit cell

The theoretical model was validated using the nonlinear finite element analysis (FEA) in ABAQUS/Standard using the Static/General nonlinear procedure[97]. The FEA model is built with 4-node bilinear quadri-lateral plane-stress element with reduced integration (CPS4R in Abaqus) and an elastic, isotropic constitutive model. The model is simulated using displacement control, such that the vertical (y) displacement on the top edge of the unit cell is prescribed. The other boundary conditions are the following: the bottom edge of the unit cell is fixed and the top edge of the unit cell has a fixed $x-$direction displacement (as shown in Fig. 2.2).

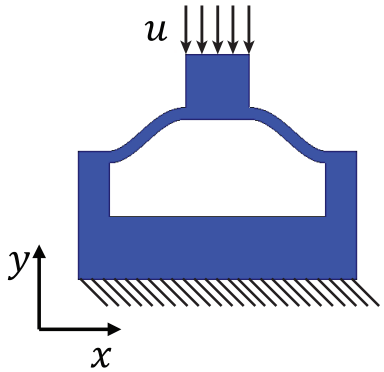

FIG. 2.2. Schematic of the unit cell model. The bottom edge is fixed, and the x direction displacement of the top edge is also fixed. The displacement u is applied on the top edge in y direction.

For a single unit cell without higher mode imperfections, the results are shown in Fig. 2.3. For a single unit cell with higher mode imperfections, the results are shown in Fig. 2.4. Results show that there is excellent agreement between the theoretical model and the FEA simulation, both in the case $a_3 = 0$ (no mode imperfection) and in the case $a_3 \neq 0$ (with modal imperfection). It can be seen in the normalized force vs. normalized deformation curve that there is one critical point whose normalized force value is $\bar{f}_{cr}$ (we will call it the critical force), from which point the beam begins to exhibit a negative stiffness. In a force control simulation, this point would correspond to the point at which the unit cell would snap through. In the normalized strain energy vs. normalized deformation curve, there is a global minimum (point I in Fig. 2.3b and 2.4b) when $\bar{d} = 0$, and a local minimum (point III in Fig. 2.3b and 2.4b) when $\bar{d} \approx 2$. These are the two stable equilibrium positions that correspond to points I and III in Fig. 2.3a and 2.4a. Moreover, there is one local maximum (point II in Fig. 2.3b and 2.4b) in the strain energy vs. deformation curve, which is an unstable equilibrium position corresponding to point II in Fig. 2.3a and 2.4a.

With higher mode imperfections, the normalized force vs deformation curve is much smoother, which is demonstrated from the comparison between Fig. 2.3a and 2.4a. Moreover, the normalized critical force and strain energy decrease for the unit cell with mode imperfections (Fig. 2.4a and 2.4b).

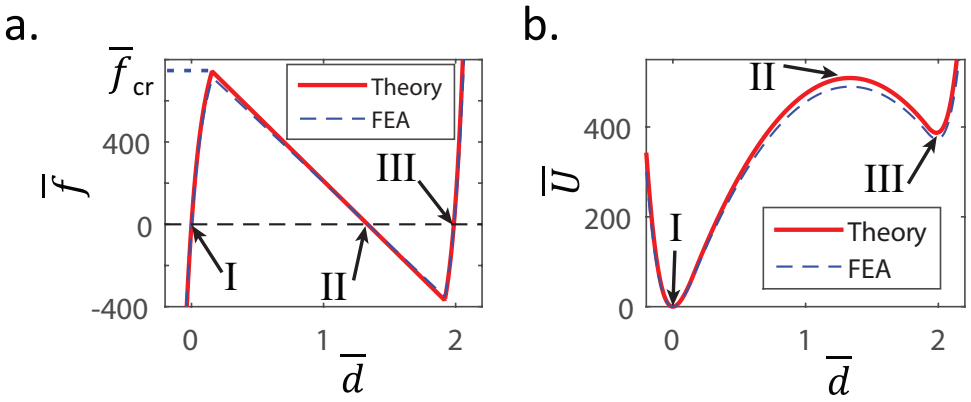

FIG. 2.3. Results of single unit cell w/o third mode imperfection ($a_3 = 0$). a. Comparison of normalized force vs. normalized deformation curves between theory and finite element model. b. Comparisons of normalized strain vs. normalized deformation curves between theory and finite element model. The geometrical parameters have the following values: $l/h = 30$, $h/t = 10$, $w = 15t$, $H = 1.5t$, and $T = 30t$.

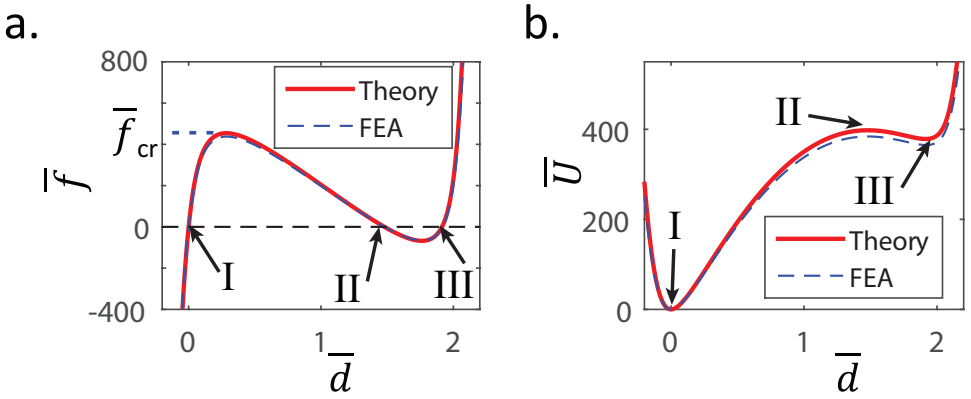

FIG. 2.4. Results of single unit cell w/ third mode imperfection ($a_3 = 0.1$). a. Comparison of normalized force vs. normalized deformation curves between theory and finite element model. b. Comparisons of normalized strain vs. normalized deformation curves between theory and finite element model. The geometrical parameters have the following values: $l/h = 30$, $h/t = 10$, $w = 15t$, $H = 1.5t$, and $T = 30t$.

2.2.3 Analysis of the mechanics of elastic unit cell

2.2.3.1 Unit cells without mode shape imperfection

After being validated by FEA simulations, the theoretical model can be employed to study the mechanics of a single unit cell made of an elastic material. Interestingly, the theoretical model shows that the normalized force and bistability of single unit cell only depend on one

non-dimensional parameter, $Q = h/t$[69]. From Fig. 2.5A, the unit cell is bistable with higher Q value (for example $Q = 4$); while it becomes monostable when Q is small (for example $Q = 1$ or $Q = 2$). For unit cells that have negative stiffness, we can examine the normalized critical force values. The relationship between normalized critical force $\bar{f}_{cr}$ and Q is shown in Fig. 2.5C. The result shows that the critical force increases initially when Q becomes bigger then converges to a maximum constant value ($\bar{f}_{cr,max} \approx 740$).

In order to analyze the effects of geometric design on the stiffness, the non-normalized force vs deformation curves are plotted in Fig. 2.5B. While the non-dimensional force only depends on Q, the non-normalized force is mainly influenced by two non-dimensional parameters, $Q = h/t$ and $P = L/t$ (where $L = l/2$). As demonstrated in Fig. 2.5B, the value of Q primarily determines whether the unit is monostable or bistable, while the value of P influences the stiffness of the unit cell. For example, the unit cell is bistable for $Q = 3$ and $P = 13.65$ since there are two points of zero force and positive slope in the force vs. deflection curve; when Q is reduced to 2.8, the unit cell is monostable since the force is always $\neq 0$ except for the initial undeformed configuration; for $Q = 3$ and $P = 15.17$, the unit cell is bistable but its stiffness in the stable deformed configuration is lower than the stiffness of unit cell with $Q = 3$ and $P = 13.65$.

More generally, the critical forces of the unit cells with different geometric designs were analyzed using the theoretical model. If the Young's modulus E, beam span l, and the beam depth b are assumed to be the same for all unit cells, then the critical force f_{cr} only relies on the initial height h and thickness t of the curved part ($f_{cr} = f_{cr}(h, t)$). The critical force contour can be obtained as the Fig. 2.5D. From this critical force contour plot, we could easily compare the relationship of the critical forces for unit cells with different geometric designs. For unit cells with constant h, the critical force increases when the thickness t increases. Moreover, the critical force is more sensitive to the value of thickness t for unit cells with smaller h. Similarly, for unit cells with constant t, the critical force increases when the value of h increases. This critical force map gives the guide for us to compare the values

of critical force for unit cells with different geometric designs.

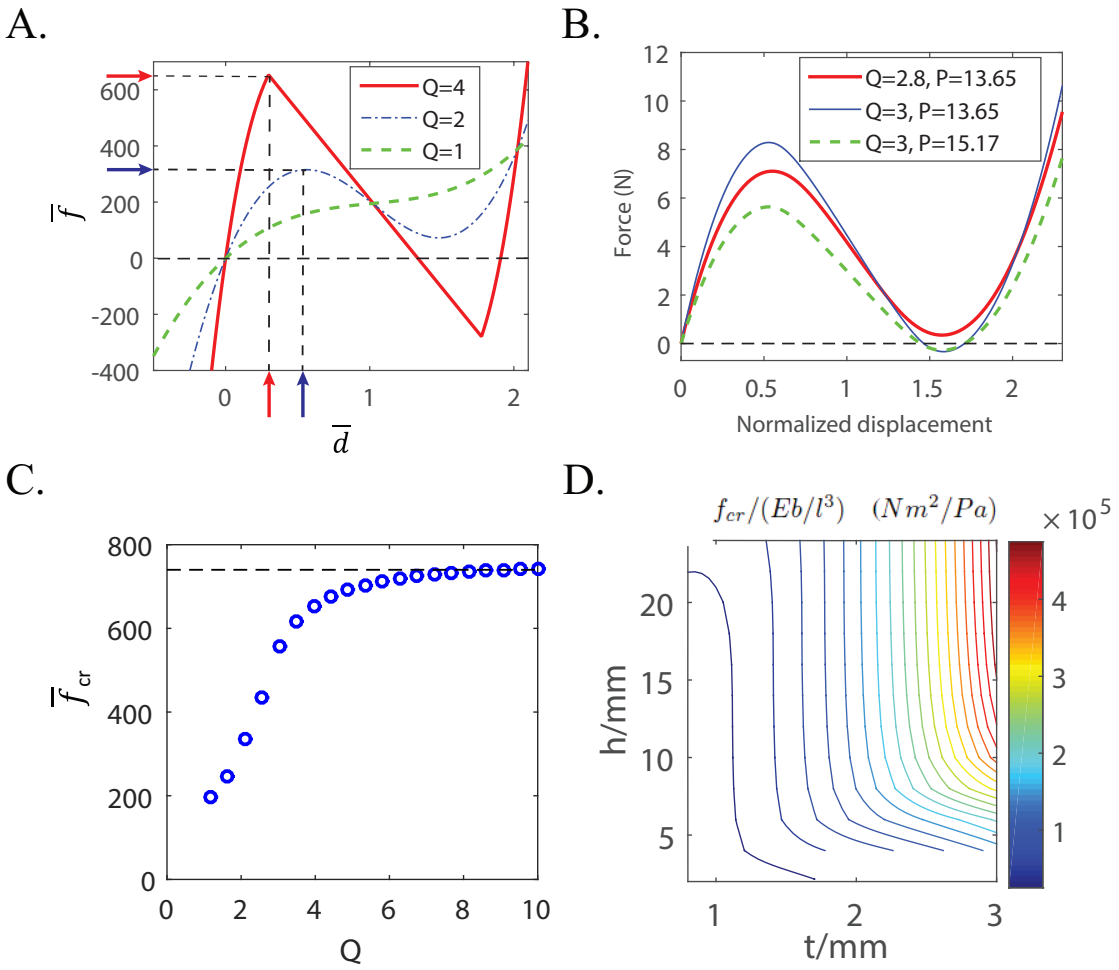

FIG. 2.5. Effects of geometric design on the mechanics of a unit cell with elastic material (all unit cells without 3^{rd} mode imperfection). A. Normalized force vs. normalized deformation curves with different Q (the vertical arrows correspond to the critical displacement $\bar{d}_{cr}$, and the horizontal arrows correspond to the critical force $\bar{f}_{cr}$). B. Force Vs. normalized deformation curves with different P and Q. C. Normalized critical force vs. Q curve. D. Contour plot of critical force with different geometric designs h and t. The geometrical parameters have the following values: $w = 5.8t$, $H = 6t$, and $T = 11.6t$ (for figure B, $t = 0.25mm$).

2.2.3.2 Unit cells with mode shape imperfection

The theoretical model can also be utilized to analyze the nonlinear mechanics of unit cells with different mode shape imperfections. The influence of a 3^{rd} mode imperfection on the normalized force vs deformation curve is shown in Fig. 2.6A. The results show that the

unit cell that is bistable when $a_3 = 0$ can become monostable as the imperfection size a_3 is increased. For example, the unit cells with $a_3 = 0$ and $a_3 = 0.1$ are bistable, while the unit cell with $a_3 = 0.25$ becomes monostable. Furthermore, the critical force of the unit cell decreases when the imperfection size a_3 increases (Fig. 2.6B).

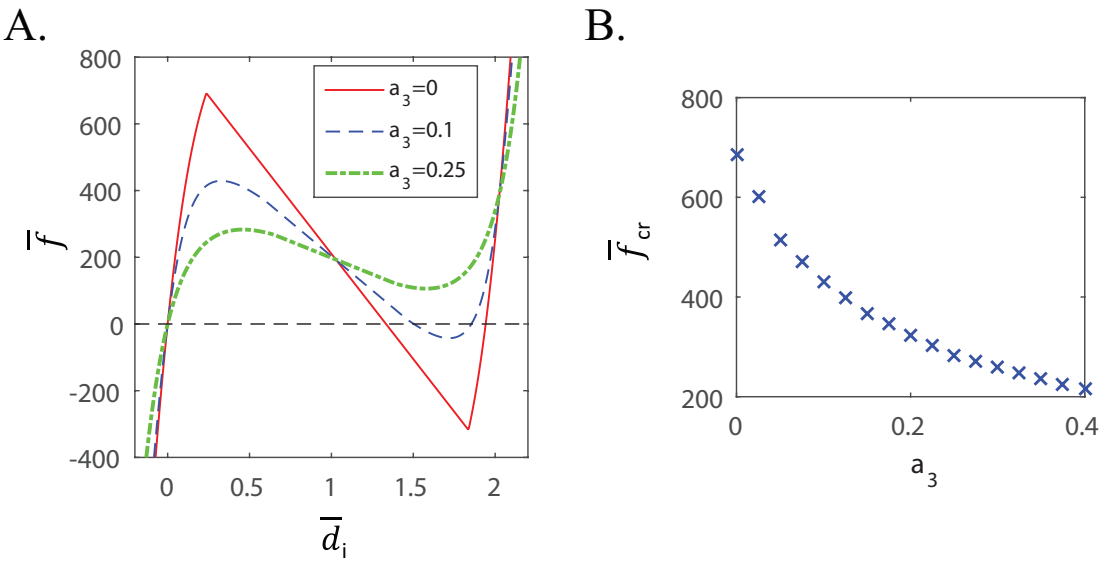

FIG. 2.6. Influence of the 3^{rd} mode shape imperfection on the mechanics of a unit cell with elastic material. A. Normalized force vs. normalized deformation curves with different a_3. B. Normalized critical force vs. a_3 curve. The geometrical parameters have the following values: $t = 0.25mm$, $Q = 5$, $H = 6t$, $P = 20$, and $T = 11.6t$.

2.3 Theoretical model of unit cell with thermoviscoelastic constitutive model

2.3.1 Theory

The theoretical model of single unit cell with an elastic constitutive model is useful to analyze the nonlinear mechanics of architected materials with snap-through instabilities. However, because most 3D printed architected materials are viscoelastic polymers, it is important to study the effects of viscoelasticity on the buckling mechanics of architected materials with snap-through instabilities. The theoretical model of most previous studies about the

nonlinear mechanics of this specific architected materials with snap-through instabilities are based on a model with elastic constitutive model. For the first time, a theoretical model with thermoviscoelastic constitutive model for this specific type of single unit cell with snap-through instabilities was developed in this section.

2.3.1.1 Governing equation

Due to viscoelasticity, the relationship between stress and strain is an integral equation. Thus, based on the governing equation for a clamped-clamped beam model with elastic constitutive model described in Section 2.2.1.1, the governing equation for a clamped-clamped beam model with viscoelastic constitutive model (Fig. 2.1c) can be expressed as,

$$I\int_0^t E(T,t-s)\frac{\partial}{\partial s}\left(\frac{\partial^4 w}{\partial x^4}\right)ds + p(t)\frac{\partial^2 w}{\partial x^2} = -f(t)\delta(x-l/2) \tag{2.20}$$

where $E(T,t)$ is the relaxation modulus, w is the lateral deflection of the beam, I is the area moment of inertial of the beam, f is the transverse force applied at the midpoint of the beam, p is the compression force, l is the beam span and δ is the Dirac delta function.

The compression force, p caused by the shortening of the beam total length, is expressed as,

$$p(t) = -\frac{A}{2l}\int_0^l\int_0^t E(T,t-s)\frac{\partial}{\partial s}\left(\frac{\partial w}{\partial x}\right)^2 dsdx \tag{2.21}$$

where A is the area of beam cross section. Due to the presence of the compression force, Eq. 2.20 is a nonlinear integro-differential equation.

The relaxation modulus $E(T,t)$ is time dependent and temperature dependent. For the Prony series model[98] schematized in Fig. 2.7, the relaxation modulus can be written as,

$$E(T,t) = E_0 + \sum_{j=1}^{m} E_j e^{-t/\tau_j(T)} \tag{2.22}$$

where t is the time, T is the temperature, E_0 is the Young's modulus of the equilibrium

branch, m is the number of viscoelastic branches, E_j (where $j = 1, .., m$) is the Young's modulus of the j^{th} nonequilibrium branch, $\tau_j(T)$ is the relaxation time constant of the j^{th} nonequilibrium branch and is temperature dependent. $\tau_j(T)$ is expressed as,

$$\tau_j(T) = \alpha(T)\tau_i^0 \tag{2.23}$$

where $\alpha(T)$ is a temperature-dependent shifting factor. Above the reference temperature, $\alpha(T)$ is given by the Williams-Landel-Ferry (WLF) equation[99,100]:

$$\log\left[\alpha(T)\right] = -\frac{C_1(T - T_M)}{C_2 + (T - T_M)} \tag{2.24}$$

where C_1 and C_2 are material constants and T_M is the WLF reference temperature. The values of the material parameters are given in Appendix A.

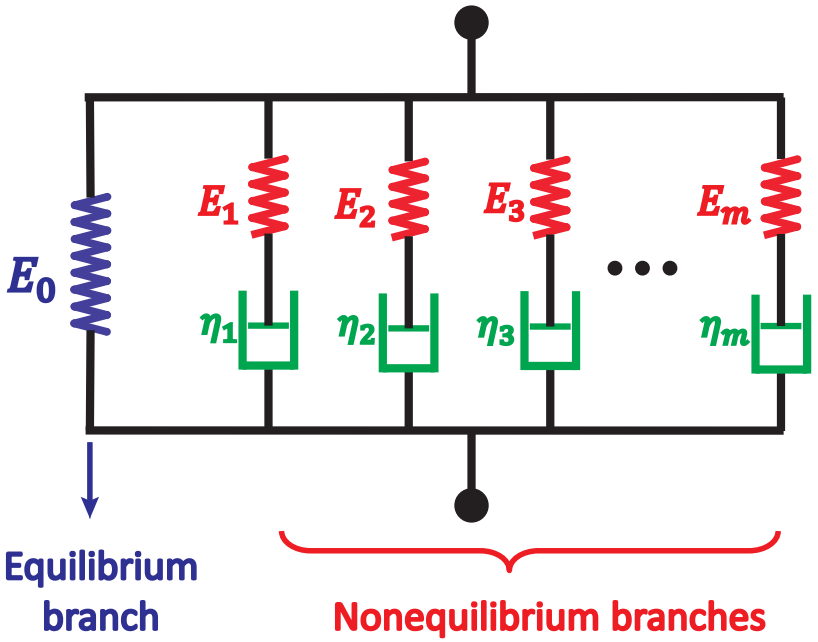

FIG. 2.7. The Prony series schematic for the viscoelastic constitutive model. E_j ($j = 0, 1, 2, \ldots, m$) represents spring stiffness, η_j ($j = 1, 2, \ldots, m$) represents the viscosity of the j^{th} branch and $\eta_j = E_j/\tau_j$, where τ_j is the time constant of the j^{th} branch.

Eqs. 2.20 and 2.21 can be rewritten as,

$$E_0 I\left[\frac{\partial^4 w(x,t)}{\partial x^4}-\frac{\partial^4 \bar{w}}{\partial x^4}\right]-I\int_0^t \frac{\partial E(T,t-s)}{\partial s}\left[\frac{\partial^4 w(x,s)}{\partial x^4}-\frac{\partial^4 \bar{w}}{\partial x^4}\right]ds \\ +p(t)\frac{\partial^2 w}{\partial x^2}=-f(t)\delta(x-l/2) \tag{2.25}$$

$$p(t)=\frac{E_0 A}{2l}\left[\left(\frac{\partial \bar{w}(x)}{\partial x}\right)^2-\left(\frac{\partial w(x,t)}{\partial x}\right)^2\right] \\ -\frac{A}{2l}\int_0^x\int_0^t \frac{\partial E(T,t-s)}{\partial s}\left[\left(\frac{\partial \bar{w}(x)}{\partial x}\right)^2-\left(\frac{\partial w(x,s)}{\partial x}\right)^2\right]dsdx \tag{2.26}$$

where $\bar{w}(x)$ is the initial shape of the beam.

2.3.1.2 Solving the governing equation

As for the elastic model, the beam shape w is decomposed into N_m mode shapes,

$$w(x,t)=\sum_{n=1}^{N_m} A_n(t)W_n(x) \tag{2.27}$$

where A_n $(n=1,2,\ldots,N_m)$ is the mode amplitude of the n^{th} mode shape, and $W_n(x)$ is the n^{th} mode shape (same as in the case with elastic constitutive model). The initial shape of the beam can also be written in the same mode superposition form as,

$$\bar{w}(x)=\sum_{n=1}^{N_m} \bar{A}_n W_n(x) \tag{2.28}$$

where $\bar{A}_n$ $(n=1,2,\ldots,N_m)$ is the initial mode amplitude of the n^{th} mode shape. For the beam studied here,

$$\bar{A}_n=\begin{cases}\dfrac{h}{2} & (n=1)\\ \dfrac{h}{2}a_3 & (n=3)\\ \dfrac{h}{2}a_n=0 & (n=2,4,\ldots,N_m)\end{cases} \tag{2.29}$$

where h is the initial apex height of the beam, a_3 is the third mode imperfection size (only the third mode imperfection was considered for the following analysis, but other higher mode imperfections are very easy to implement in the theoretical model).

Using Galerkin method[101], the above integro-differential equation (Eq. 2.25) is transformed into a set of nonlinear integral equations by multiplying $W_i(x)$ and integrating over the domain from 0 to l,

$$\begin{aligned} I\sum_{n=1}^{N_m}(A_n-\bar{A}_n)\left[E_0\int_0^l W_i(x)W_n^{(4)}(x)dx+\int_0^t\int_0^l \frac{\partial E(T,t-s)}{\partial s}W_i(x)W_n^{(4)}(x)dxds\right] \\ +p(t)\sum_{n=1}^{N_m}A_n\int_0^l\frac{\partial^2 W_n(x)}{\partial x^2}W_i(x)dx=-f_i(t)\quad \text{for } n=1,3,\ldots,N_m \end{aligned} \tag{2.30}$$

such that, at time t_M, the equation of motion for mode n can be written in the following form,

$$\begin{aligned} \left[A_n(t_M)-\overline{A}_n\right]-\frac{1}{\sum_{j=0}^{m}E_j}\sum_{j=1}^{m}\eta_j I_{n,j}(t_M) \\ -\frac{A}{4IN_n^2}A_n(t_M)\sum_{n=1}^{N_m}N_n^2\left[\overline{A}_n^2-A_n^2(t_M)\right]-\frac{A}{4IN_n^2}A_n(t_M)\frac{1}{\sum_{j=0}^{m}E_j}\sum_{n=1}^{N_m}\left[N_n^2\sum_{j=1}^{m}\eta_j J_{n,j}(t_M)\right] \\ =-F_n(t)\quad \text{for } n=1,3,\ldots,N_m \end{aligned} \tag{2.31}$$

where $I_{n,j}(t_M)$ and $J_{n,j}(t_M)$ are the following integrals,

$$I_{n,j}(t_M)=\int_0^{t_M} e^{-\frac{t_M-t}{\tau_j}}\left[A_n(t)-\overline{A}_n\right]ds \tag{2.32}$$

$$J_{n,j}(t_M)=\int_0^{t_M} e^{-\frac{t_M-t}{\tau_j}}\left[A_n^2(t)-\overline{A}_n^2\right]ds \tag{2.33}$$

Note that the time constants τ_j vary by order of magnitude (refer to Fig. 2.8), such that

integrating $I_{n,j}(t_M)$ and $J_{n,j}(t_M)$ accurately is challenging.

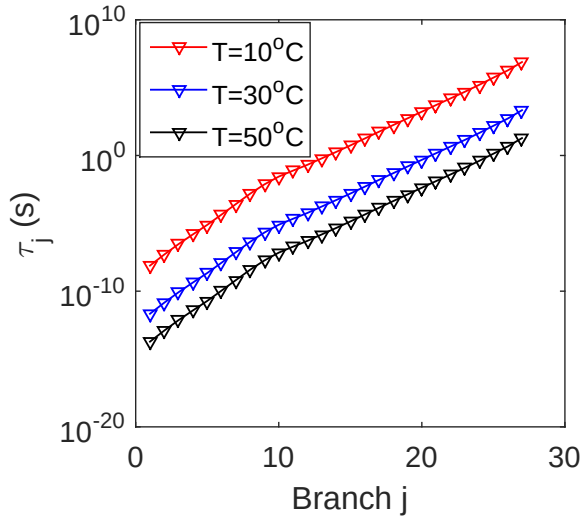

FIG. 2.8. Time constants of the digital material DM9895 used in this thesis.

In order to calculate these integrals, the interval $0 \leq t \leq t_M$ is discretized into time steps of duration Δt. $A_n(t)$ and $A_n^2(t)$ are approximated by piecewise linear functions. For $t_k \leq t \leq t_{k+1}$,

$$A_n(t) = A_n(t_k) + \frac{A_n(t_{k+1}) - A_n(t_k)}{\Delta t}(t - t_k) \tag{2.34}$$

$$A_n^2(t) = A_n^2(t_k) + \frac{A_n^2(t_{k+1}) - A_n^2(t_k)}{\Delta t}(t - t_k) \tag{2.35}$$

With these assumptions, $I_{n,j}(t_M)$ and $J_{n,j}(t_M)$ can be eventually written as,

$$I_{n,j}(t_M) = \Delta t \sum_{k=1}^{M} a_{k,j}(t_M) \left[A_n(t_k) - \bar{A}_n\right] \tag{2.36}$$

$$J_{n,j}(t_M) = \Delta t \sum_{k=1}^{M} a_{k,j}(t_M) \left[A_n^2(t_k) - \bar{A}_n^2\right] \tag{2.37}$$

where,

$$\begin{aligned} a_{1,j}(t_M) =& \frac{\tau_j}{\Delta t} e^{-\frac{t_M}{\tau_j}} \left[\frac{\tau_j}{\Delta t} e^{\Delta t/\tau_j} - (1 + \frac{\tau_j}{\Delta t}) \right] \\ a_{k,j}(t_M) =& \frac{\tau_j^2}{\Delta t^2} e^{\frac{t_k - t_M}{\tau_j}} \left[e^{\Delta t/\tau_j} - 2 + e^{-\Delta t/\tau_j} \right] \quad \text{for } k = 2, 3, \ldots, M-1 \\ a_{M,j}(t_M) =& \frac{\tau_j}{\Delta t} \left[1 - \frac{\tau_j}{\Delta t} + \frac{\tau_j}{\Delta t} e^{-\Delta t/\tau_j} \right] \end{aligned} \tag{2.38}$$

Eq. 2.38 can be implemented accurately as long as $\frac{\Delta t}{\tau_j}$ is not too small. However, if $\frac{\Delta t}{\tau_j}$ is very small, Taylor series approximations are used,

$$e^x \approx 1 + x + \frac{1}{2} x^2 \quad \text{if } x \ll 1 \tag{2.39}$$

such that, for $\frac{\Delta t}{\tau_j} < \epsilon$ (where ϵ was chosen to be $3.39e-6$ in the code), $a_{k,j}(t_M)$ can be written as,

$$\begin{aligned} a_{1,j}(t_M) =& \frac{1}{2} e^{-\frac{t_M}{\tau_j}} \\ a_{k,j}(t_M) =& 1 + e^{\frac{t_k - t_M}{\tau_j}} \quad \text{for } k = 2, 3, \ldots, M-1 \\ a_{M,j}(t_M) =& \frac{1}{2} \end{aligned} \tag{2.40}$$

Using Eqs. 2.31, 2.36 and 2.37, the following system of nonlinear equations are derived,

$$\begin{aligned} \left[1 - \Gamma \sum_{j=1}^{m} \eta_j a_{M,j} \right] \left[A_n(t_M) - \bar{A}_n - \frac{A}{4IN_n^2} A_n(t_M) \sum_{n=1}^{N_m} \left(\bar{A}_n^2 - A_n^2(t_M) \right) \right] \\ - \Gamma \left[\sum_{k=1}^{M} \left(\left(A_n(t_k) - \bar{A}_n \right) \sum_{j=1}^{m} \eta_j a_{k,j}(t_M) \right) \right. \\ \left. - \frac{A}{4IN_n^2} A_n(t_M) \sum_{k=1}^{M} \left(\sum_{j=1}^{m} \eta_j a_{k,j}(t_M) \sum_{n=1}^{N_m} N_n^2 \left(\bar{A}_n^2 - A_n^2(t_k) \right) \right) \right] \\ = -F_n(t) \quad \text{for } n = 1, 3, \ldots, N_m \end{aligned} \tag{2.41}$$

where,

- n is the mode index ($n = 1, 2, \ldots, N_m$)
- j is the Prony branch index ($j = 1, 2, \ldots, m$)
- t_M is the current time step
- A_n is the mode amplitude of mode n ($n = 1, 2, \ldots, N_m$)
- $a_{k,j}$ is the integration parameters ($k = 1, \ldots, M$; $j = 1, 2, \ldots, m$) (depending on the value of τ_j relative to ΔT, Eq. 2.38 or 2.40 is used to evaluate $a_{k,j}$)
- Γ is given by,

$$\Gamma = \frac{\Delta t}{\sum_{j=0}^{m} E_j} \tag{2.42}$$

The deformation of the beam is calculated by,

$$d(t_M) = h - 2 \sum_{n=1,5,9,13,\ldots} A_n(t_M) \tag{2.43}$$

There are $N_m - 1$ equations of the type Eq. 2.41 (because the second mode is assumed to be constrained) and 1 equation of type Eq. 2.43. There are N_m unknowns at each time step t_M: $A_1(t_M)$, $A_3(t_M)$, ..., $A_{N_m}(t_M)$ and $f(t_M)$. The system of equations was solved numerically at each time step using the $fsolve$ function in MATLAB. After solving these equations, the relationship between force and deformation can be derived.

The procedure of solving the governing equation for theoretical model with viscoelastic constitutive model is summarized as the following flowchart (Fig. 2.9).

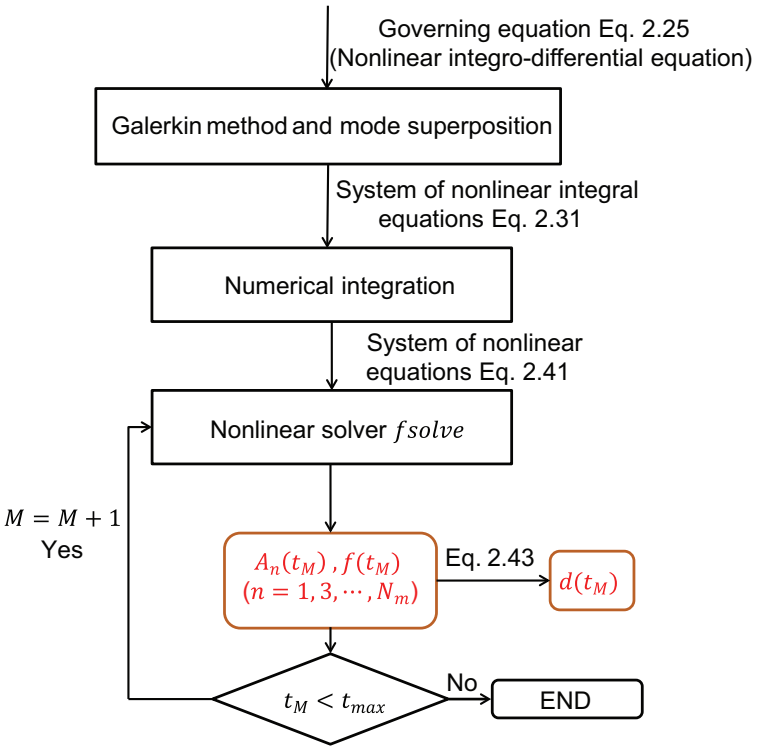

FIG. 2.9. Flowchart of solving the governing equation for theoretical model with viscoelastic constitutive model.

2.3.2 Validation of the theoretical model of viscoelastic unit cell

The theoretical model for a unit cell with viscoelastic constitutive model was validated using nonlinear finite element analysis in ABAQUS/Standard using the quasi-static analysis "General: Visco" nonlinear procedure[97]. Considering efficiency, the FEA model was built as a half beam model (shown in Fig. 2.10) with 2-node Euler-Bernoulli beam element in a plane with cubic integration (B23 in Abaqus) and a viscoelastic, isotropic constitutive model. A temperature field was defined for the whole FEA model. The model was simulated using displacement control, such that the vertical (y) displacement on the top right node of the beam was prescribed. The other boundary conditions are the following: the bottom left node of the beam was fixed and the top right node had a symmetric boundary condition, *i.e.*, it had a fixed x-direction displacement and z-direction rotation.

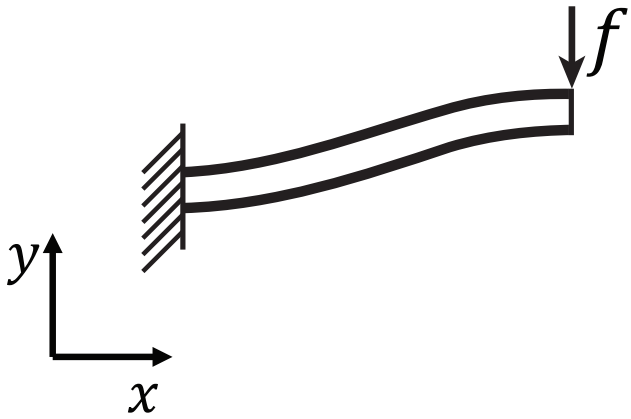

FIG. 2.10. Schematic of FEA model for single unit cell with viscoelastic constitutive model.

The force, f, and deformation, d, are normalized using the following equations,

$$\bar{f} = \frac{fl^3}{(\sum_{j=0}^{m} E_j)Ih}, \quad \bar{d} = \frac{d}{h} \tag{2.44}$$

It was found that in order to obtain converged results, the computational time was much lower for the theoretical model compared to FEA; however, the computational efficiency was not rigorously analyzed (for example, the number of mode shapes and finite elements needed to obtain a certain error tolerance was not evaluated). The value of the time step, Δt, required to achieve converged results was determined at each temperature. One convergence study result is shown in Fig. 2.11 (at room temperature $T = 20^oC$, with loading strain rate $\dot{\epsilon} = 1000s^{-1}$). The convergence criterion is defined as $\alpha \leq 1\%$, which is given by,

$$\alpha = \frac{|\bar{f}(1) - \bar{f}_{ref}(1)|}{\bar{f}_{ref}(1)} \times 100\% \tag{2.45}$$

where, $\bar{f}(1)$ is the normalized force at normalized deformation $\bar{d} = 1$, $\bar{f}_{ref}(1)$ is the reference converged normalized force at normalized deformation $\bar{d} = 1$. For this example, the time step Δt for theoretical model to obtain the converged result is $1e - 6$s.

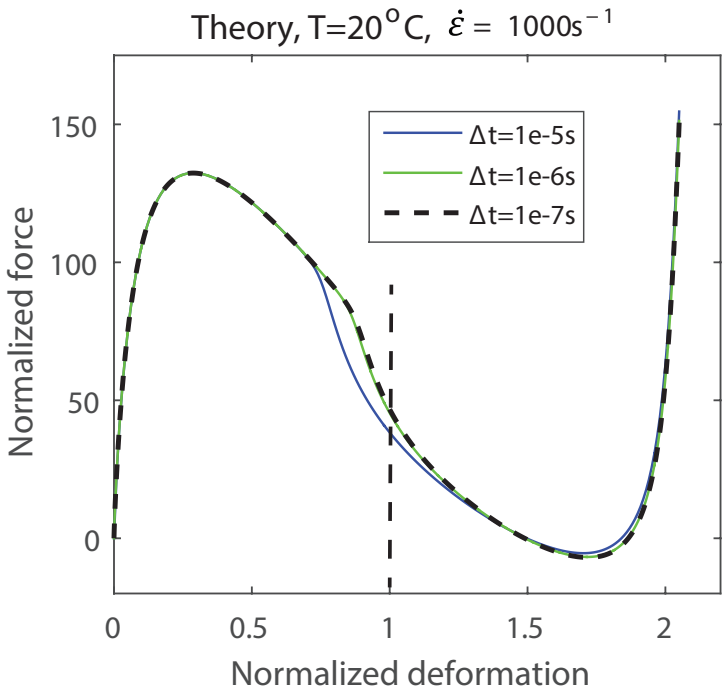

FIG. 2.11. Convergence study for single beam model with viscoelastic material (the imperfection size $a_3 = 0$, $\dot{\epsilon}$ is the loading strain rate). The geometrical parameters have the following values: $l/h = 50$, $h/t = 10$.

The curves of normalized force vs. normalized deformation for a single unit cell with viscoelastic constitutive model are shown in Fig. 2.13 at constant temperature for different strain rates. Note that there is excellent agreement between results of theoretical model and FEA simulations with different strain rates at the reference temperature ($T_M = -3^oC$). For results at room temperature ($T = 20^oC$), slight differences are observed between results of theoretical model and FEA simulations. As shown in the following figure (Fig. 2.16), this discrepancy is not due to an inaccuracy of the theoretical model; slight mode imperfections are introduced in FEA models due to the presence of discrete elements. These discrete elements cause the FEA model not to be perfectly accurate at high temperature. This is validated from the results in Fig. 2.12. When the number of elements in the FEA model increases, the result from FEA tends to get closer to the result from theoretical model. A rigorous convergence study would be needed to determine whether the FEA model converge to the theoretical model.

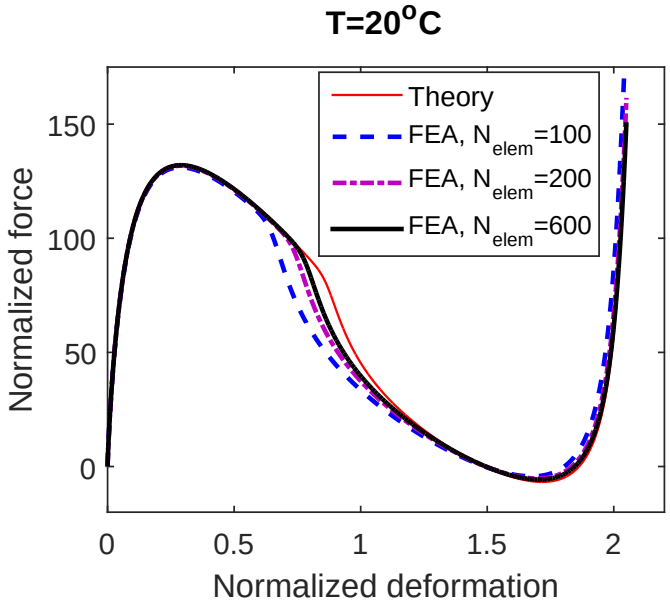

FIG. 2.12. Influence of the number of elements in FEA model of a unit cell with viscoelastic constitutive model at room temperature ($T = 20^oC$). The geometrical parameters have the following values: $l/h = 50$, $h/t = 10$.

Fig. 2.13 demonstrates that the stiffness of unit cell with viscoelastic material decreases when the loading strain rate decreases; moreover, the critical force also decreases for smaller strain rate. With higher strain rate (for example, $\dot{\epsilon} = 1000s^{-1}$), the mechanical response of this unit cell with viscoelastic material at reference temperature is similar to the force vs displacement curve of unit cell with elastic material, which corresponds to the theory that the polymer behaves almost elastically at high strain rate.

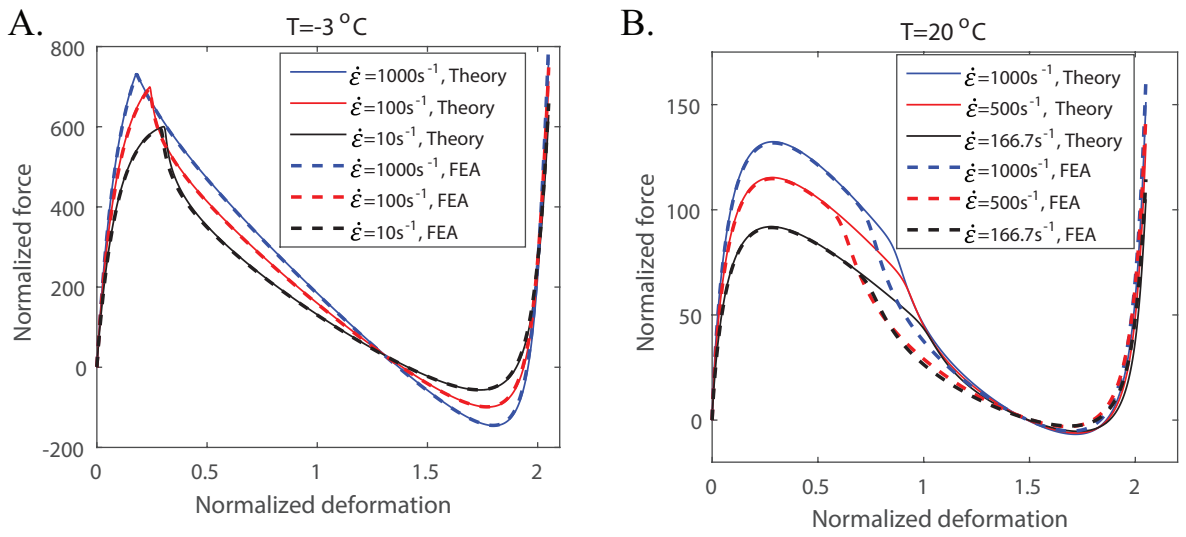

FIG. 2.13. Comparison of normalized force vs. normalized deformation curves between theory and finite element model for single unit cell with viscoelastic constitutive model using different loading strain rates (the imperfection size $a_3 = 0$). A. The temperature is reference temperature $T = -3^oC$. B. The temperature is room temperature $T = 20^oC$. Solid lines are results from theoretical models, dashed lines are results from FEA simulations. The geometrical parameters have the following values: $l/h = 50$, $h/t = 10$.

The normalized force vs. normalized deformation for a single unit cell with viscoelastic constitutive model are shown in Fig. 2.14 at different temperatures for a constant strain rate. The results demonstrate that the stiffness of unit cell with viscoelastic material decreases when the temperature increases; moreover, the critical force also decreases for higher temperatures.

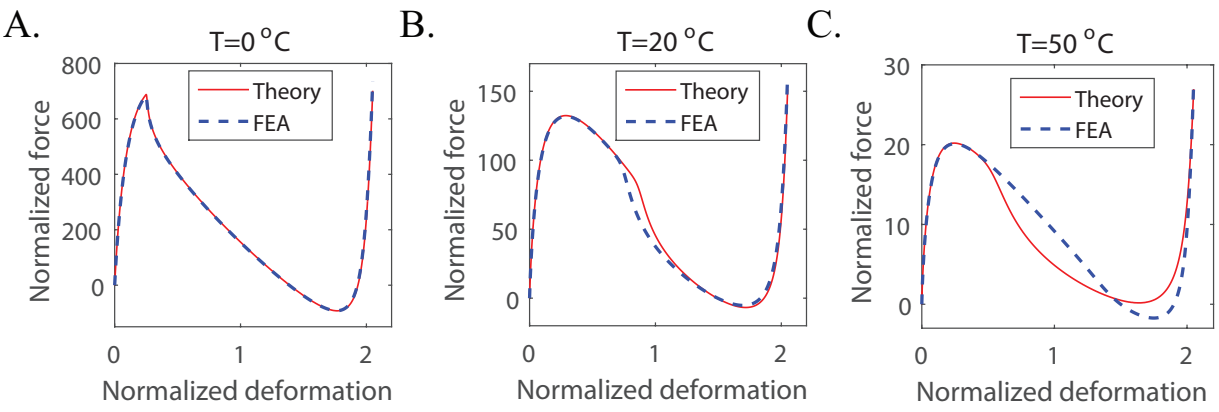

FIG. 2.14. Comparison of normalized force vs. normalized deformation curves between theory and finite element model for single unit cell with viscoelastic constitutive model at different temperatures (the imperfection size $a_3 = 0$). A. $T = 0^oC$. B. $T = 30^oC$. C. $T = 50^oC$. The loading strain rate is constant ($\dot{\epsilon} = 1000s^{-1}$). Solid lines are results from theoretical models, dashed lines are results from FEA simulations. The geometrical parameters have the following values: $l/h = 50$, $h/t = 10$.

Again, note that there is excellent agreement between theoretical model and FEA simulations at lower temperatures (for example, $T = 0^oC$). Some differences are observed between results obtained from theoretical model and FEA simulations at higher temperatures (for example, $T = 50^oC$). These differences are related to the differences in the mode shapes between theoretical model and FEA models. The mode amplitudes for FEA simulations are obtained using Eq. 6.4 of Appendix B.

When the beam model is discretized into beam elements in FEA model, it is very likely some higher mode imperfections would be introduced; however, there are no mode imperfections in the theoretical model for perfect beam model. This difference rendered the variation between the mode amplitudes obtained from theoretical model and FEA simulations (shown in Fig. 2.15A). For the first three symmetric modes, the results show that the differences of the mode amplitudes become larger at the middle regime of the simulation time. However, if a slight mode imperfection is introduced for both theoretical model and FEA model, the mode amplitudes match almost exactly between theory and FEA (Fig. 2.15B).

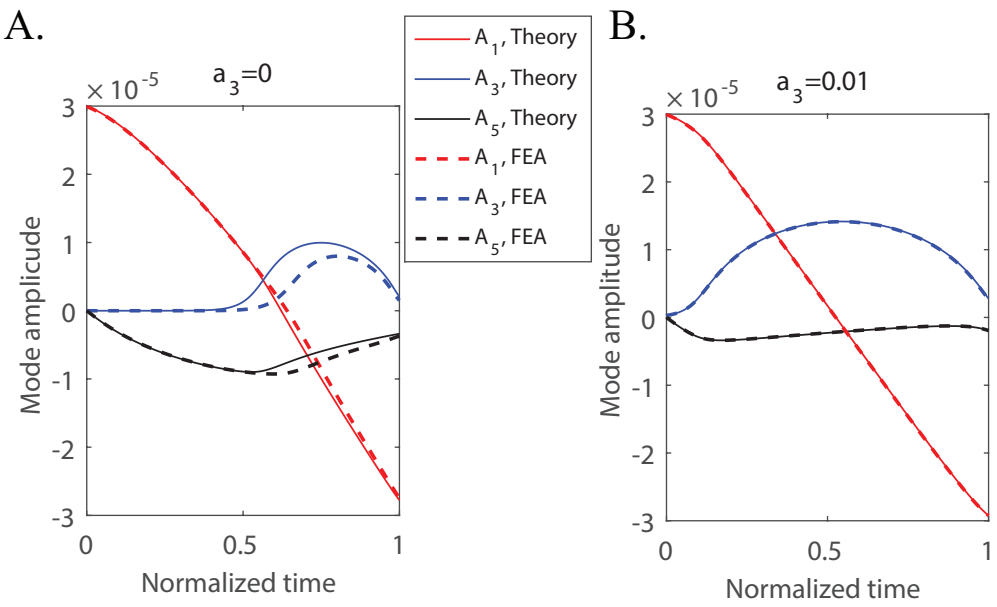

FIG. 2.15. Comparison of mode amplitudes (the first three symmetric modes) obtained from theory and finite element model for a unit cell with viscoelastic constitutive model at $T = 50^oC$. A. No mode imperfection. B. The imperfection size $a_3 = 0.01$. The loading strain rate is constant ($\dot{\epsilon} = 1000s^{-1}$), solid lines are results from theoretical models, dashed lines are results from FEA simulations. The geometrical parameters have the following values: $l/h = 50$, $h/t = 10$.

The above explanation was validated by results from models with higher mode imperfections. Fig. 2.16 demonstrates that when the introduced imperfection becomes bigger, the difference between the results from the theoretical model and FEA simulation gets smaller and smaller. When the mode imperfection size $a_3 \geq 0.001$, the normalized force vs normalized deformation curves match almost exactly.

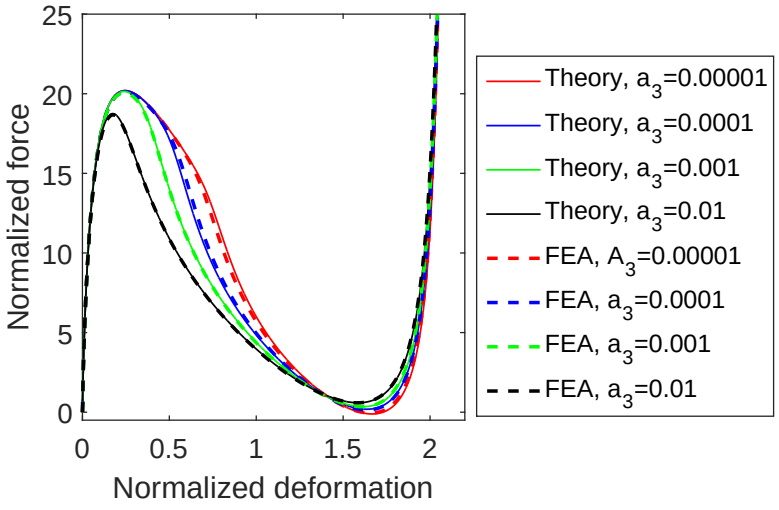

FIG. 2.16. Comparison of normalized force vs. normalized deformation curves between theory and finite element model for single unit cell with viscoelastic constitutive model with different imperfection sizes. The loading strain rate is constant ($\dot{\epsilon} = 1000s^{-1}$), the temperature is $T = 50^oC$. Solid lines are results from theoretical model, dashed lines are results from FEA simulations. The geometrical parameters have the following values: $l/h = 50$, $h/t = 10$.

When higher mode imperfections are introduced, Fig. 2.17 gives the normalized force vs. normalized deformation curves with constant strain rate at different temperatures. Compared with the results of perfect unit cells, there is excellent agreement for unit cells with higher mode imperfections between results of theoretical model and FEA simulations, even at higher temperatures (50^oC). Moreover, with higher mode imperfections, the FEA simulations are found to converge much faster. For example, previous for perfect model with $T = 20^oC$, the time step Δt should be as small as $1e-8$s; however, with 1% higher mode imperfection, the time step Δt of converged results can be as large as $1e-6$s.

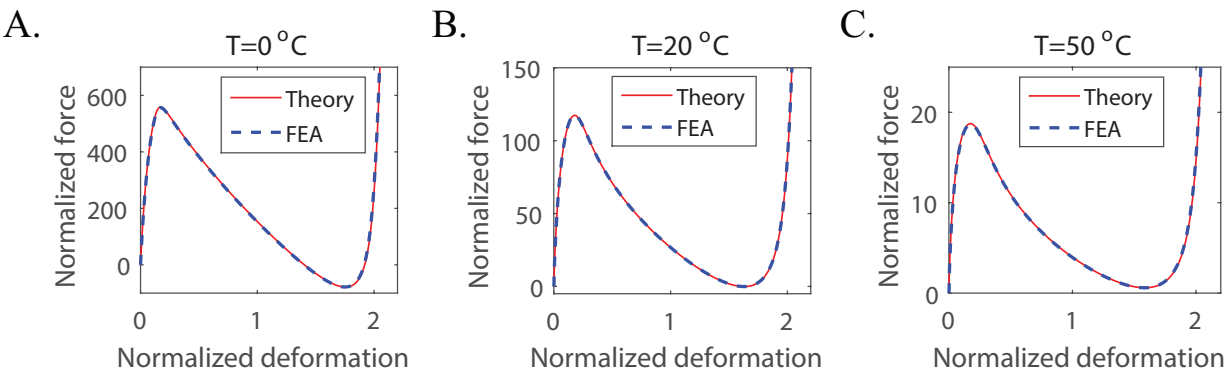

FIG. 2.17. Comparison of normalized force vs. normalized deformation curves between theory and finite element model for single unit cell with viscoelastic constitutive model at different temperature (the imperfection size $a_3 = 0.01$). A. $T = 20^oC$. B. $T = 50^oC$. The loading strain rate is constant ($\dot{\epsilon} = 1000s^{-1}$). Solid lines are results from theoretical model, dashed lines are results from FEA simulation. The geometrical parameters have the following values: $l/h = 50$, $h/t = 10$.

2.3.3 Analysis of the mechanics of viscoelastic unit cell

After being validated by FEA simulations, the theoretical model can be employed to study the mechanics of the single unit cell with viscoelastic material. Unlike the case of the elastic model, the critical force f_{cr} of single unit cell is not only related to geometric design, but also related to temperature and loading strain rate.

2.3.3.1 Unit cells without mode shape imperfection

For perfect unit cells without mode shape imperfection, utilizing the theoretical model, the critical force vs. temperature with different loading strain rates was plotted in Fig. 2.18. From the results, it demonstrates that the critical force becomes smaller with higher temperature or lower loading strain rate. Besides of geometric design parameters, temperature and loading strain rate can also be utilized to tune the critical force of unit cells.

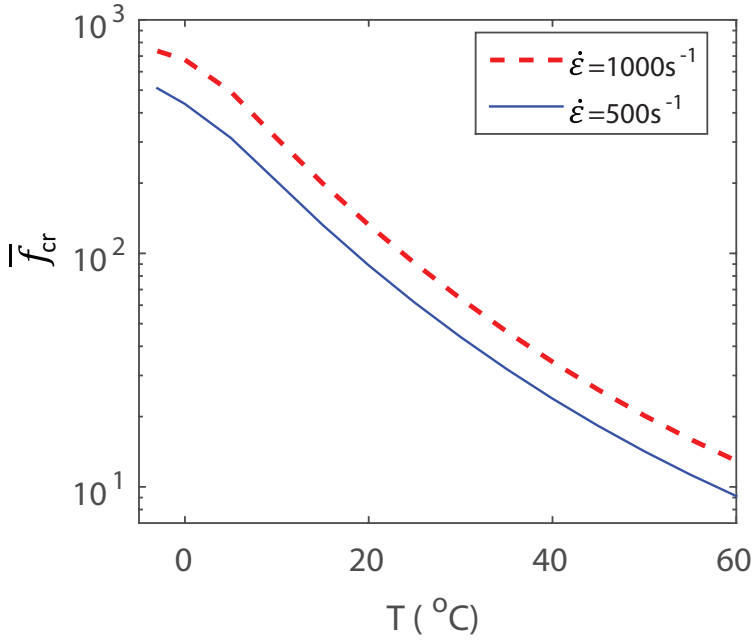

FIG. 2.18. Normalized critical force vs. temperature curves for single unit cell with viscoelastic constitutive model for different strain rates (the imperfection size $a_3 = 0$). The geometrical parameters have the following values: $l/h = 50$, $h/t = 10$.

2.3.3.2 Unit cells with mode shape imperfection

With higher mode imperfection, the critical force vs. temperature was plotted in Fig. 2.19. As observed in the case of the elastic model, the critical force decreases as mode imperfection size increases for constant strain rate and temperature.

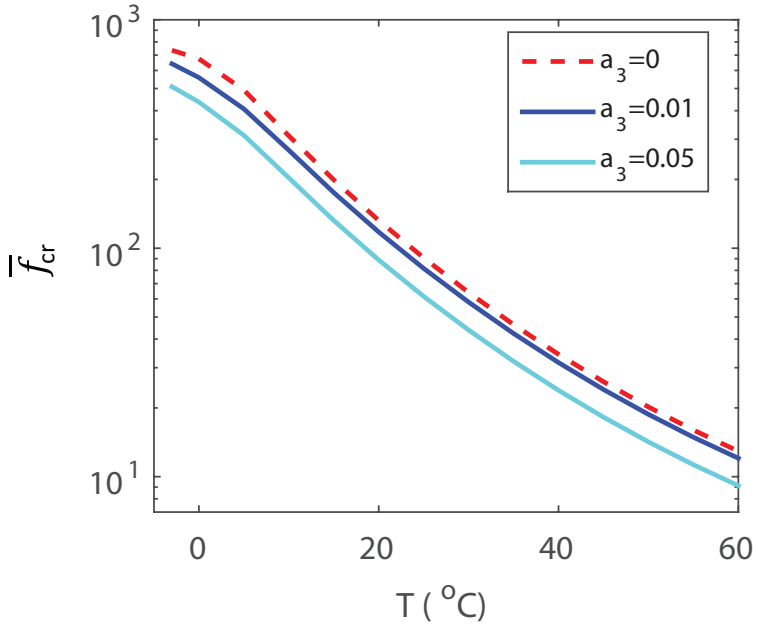

FIG. 2.19. Normalized critical force vs. temperature curves for single unit cell with viscoelastic constitutive model with different imperfection sizes. The loading strain rate is constant ($\dot{\epsilon} = 1000s^{-1}$), the geometrical parameters have the following values: $l/h = 50$, $h/t = 10$.

2.4 Summary

In this chapter, theoretical models of a unit cell with snap-through instabilities were developed for both the cases of an elastic constitutive model and thermoviscoelastic constitutive model. These theoretical models were validated using FEA simulations. Excellent agreement was observed between results of theoretical models and FEA simulations (mode imperfections need to be introduced for the viscoelastic case). Compared with the theoretical model with thermoviscoelastic constitutive model, the theoretical model with elastic constitutive model is simpler. Despite its relative simplicity, it is useful to analyze the nonlinear mechanics of single unit cell with snap-through instabilities. For example, this model is useful to understand the influence of geometric parameters on the mechanics of the unit cell. The results showed that two important geometric non-dimensional parameters (P and Q) determine the stiffness and bistability of the unit cell. By modifying the geometric parameters

and mode imperfection size, the critical force of the unit cell can be tuned. For the specific type of unit cell studied in this thesis, a theoretical model with thermovisoelastic constitutive model was developed for the first time. The theoretical model made it possible to study the effects of strain rate and temperature on the mechanical response of single unit cell with snap-through instabilities. The theoretical model with thermoviscoelastic constitutive model developed in this chapter is much more computationally efficient than FEA simulations to obtain converged results. For unit cells with thermoviscoelastic material, the results show that the critical force for single unit cell with same geometric design decreases at higher temperature or lower strain rate due to the material's viscoelasticity effect. Thus, temperature, strain rate, and geometric design parameters (like thickness, imperfection size, etc) are control parameters than can be utilized to tailor the critical force for single unit cells with thermoviscoelastic material. The theoretical models of single unit cells with snap-through instabilities developed in this chapter are useful tools for the design and analysis of architected materials comprised of this type of unit cells.

Chapter 3

Elastic architected materials with a deterministic snapping sequence

3.1 Introduction

When a multi-layer architected material with snap-through instabilities is loaded, each layer snaps sequentially. The sequence in which each layer snaps (*i.e.*, which layer snaps 1^{st}, 2^{nd}, ...) can be defined as the snapping sequence. Although previous papers give important insight into the design and mechanics of these architected materials with snap-through instabilities, these previous works have not investigated strategies that would make it possible to tune their snapping sequence. The snapping sequence of architected materials with snap-through instabilities is unpredictable if, as in most previous works, the architecture consists of identical unit cells[4,1]. Imperfections in the geometry, material properties[102,103,104] or in the boundary conditions determine the deformation sequence in this case. This is validated by the experiments as shown in Fig. 3.1. These two samples with identical unit cells were fabricated using the same nominal design parameter values; however, they have opposite snapping sequences when they are compressed at a constant velocity: for sample #1, the top layer snaps first, then the bottom layer snaps; while the snapping sequence is from

bottom to top for sample #2.

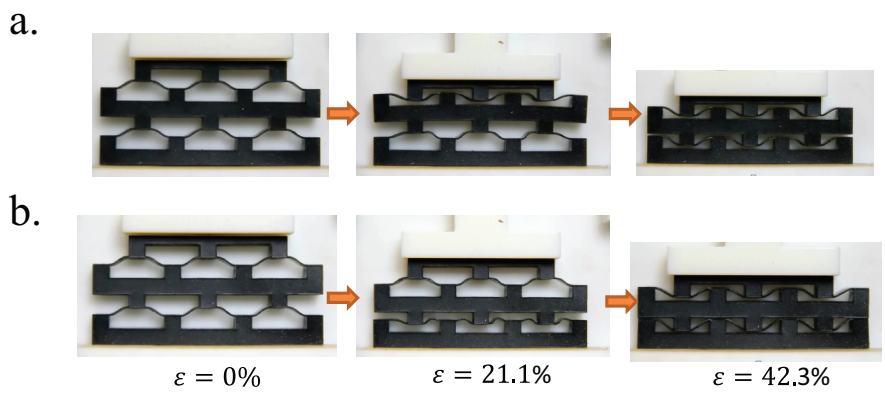

FIG. 3.1. Snapshots of compression experiments on two fabricated samples with identical unit cells. a. Sample #1 snapped from top to bottom. b. Sample #2 snapped from bottom to top. (ϵ is the effective strain of the samples at different time step, which is defined by the ratio of the samples' displacement and the overall height.)

Motivated by this, this chapter studied how to tune the snapping sequence of architected materials with snap-through instability in a controllable manner[105]. In this chapter, the snapping sequence of these architected materials were investigated using theoretical models, finite element simulations and experiments. Strategies that make it possible to tune the snapping sequence are established and analyzed.

3.2 Theoretical model for multilayer architected materials with snap-through instabilities

A theoretical model for a multilayer architected material that is comprised of a series of bistable unit cells was developed by extending the theoretical model described in Chapter 2.2 for a single unit cell. Consider the architected material with n unit cells in series shown in Fig. 3.2a and the corresponding schematics shown in Fig. 3.2b. In the theoretical model, the beams are connected by a rigid link. The bottom beam (beam 1) has clamped-clamped boundary conditions; the left and right ends of the other beams (beams $2, 3, \ldots, n$) are only allowed vertical (y-direction) displacement. The thicknesses of the curved part of each unit

cell are t_i. For all unit cells, the initial height of the curved parts is h. The displacements of the midpoint of the curved part of unit cell i is u_i (see Fig. 3.2b); the deformations of the unit cells can be expressed as,

$$\begin{aligned} d_1 &= u_1 \\ d_i &= u_i - u_{i-1}, \quad \text{for } i = 2, \ldots, n \end{aligned} \tag{3.1}$$

and the total deformation is,

$$d_{tot} = \sum_{i=1}^{n} d_i \tag{3.2}$$

The total deformation, d_{tot}, the total strain energy, U_{tot}, and the loading force, f, are normalized with respect to the parameters of unit cell 1, *i.e.*, the following definitions are used for the normalized force, $\overline{f}$, the normalized deformation, $\overline{d}_{tot}$ and the normalized strain energy, $\overline{U}_{tot}$:

$$\overline{f} = \frac{l^3}{EI_1 h} f, \ \overline{d}_{tot} = \frac{d_{tot}}{h}, \ \overline{U}_{tot} = \frac{l^3}{EI_1 h^2} U_{tot} \tag{3.3}$$

where I_1 is the area moment of inertia of beam 1. When each of the unit cells is isolated, a subscript i refers to the properties of the ith unit cell. For single unit cells, the applied force f_i, the deformation, d_i and the strain energy, U_i, are normalized with respect to the properties of unit cell 1:

$$\overline{f_i} = \frac{l^3}{EI_1 h} f_i, \ \overline{d}_i = \frac{d_i}{h}, \ \overline{U}_i = \frac{l^3}{EI_1 h^2} U_i \tag{3.4}$$

where $\overline{f}_i$, $\overline{d}_i$ and $\overline{U}_i$ are the normalized force, deformation and strain energy for unit cell i, respectively.

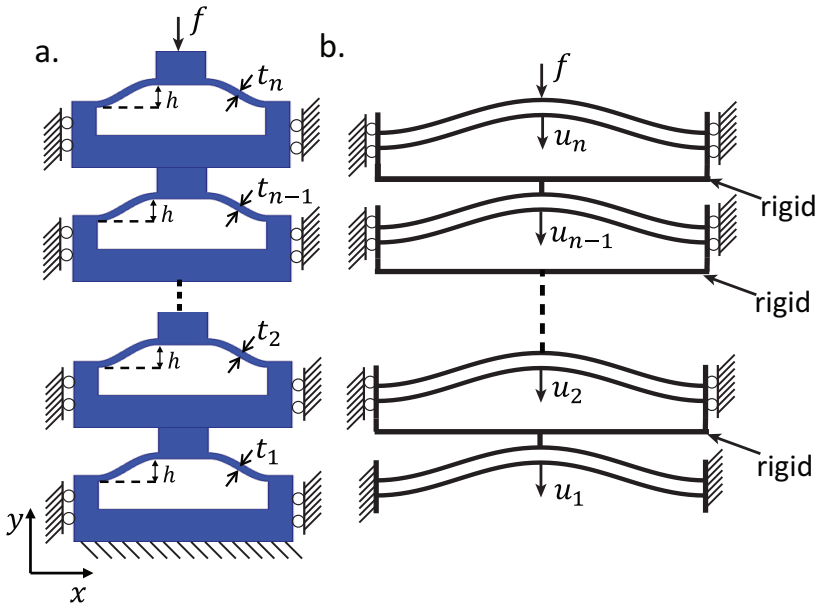

FIG. 3.2. a. Multiple unit cells in series. b. Schematics of the theoretical model with multiple unit cells in series.

The normalized deformations of each unit cell can be expressed as a vector $(\overline{d}_1, \overline{d}_2, \ldots, \overline{d}_n)$. In order to determine the values of the components in this vector when the total normalized deformation $\overline{d}_{tot}$ is increased, an algorithm similar to the algorithm proposed by Oh and Kota[106] and Overvelde *et al.*[107] for multistable mechanisms can be used. This algorithm requires calculating the total normalized strain energy of the system, $\overline{U}_{tot}(\overline{d}_1, \overline{d}_2, \ldots, \overline{d}_n)$, which can be computed by,

$$\overline{U}_{tot}(\overline{d}_1, \overline{d}_2, \ldots, \overline{d}_n) = \sum_{i=1}^{n} \overline{U}_i(\overline{d}_i) \tag{3.5}$$

where $\overline{d}_n = \overline{d}_{tot} - \sum_{i=1}^{n-1} \overline{d}_i$. The normalized strain energy for each unit cell $\overline{U}_i$ is determined using the theoretical model of section 2.2.1. In this algorithm, the loading from $\overline{d}_{tot} = 0$ to $\overline{d}_{tot,max}$ is discretized into small steps of amplitude $\delta\overline{d}$. Assuming that at step k of this algorithm, the values of $(\overline{d}_1, \overline{d}_2, \ldots, \overline{d}_n)$ are $(\overline{d}_1^k, \overline{d}_2^k, \ldots, \overline{d}_n^k)$; at step $k+1$, the values are found

by solving the following optimization problem,

$$\begin{aligned} &\min \overline{U}_{tot}(\overline{d}_1, \overline{d}_2, \ldots, \overline{d}_n) \\ &\text{with respect to } (\overline{d}_1, \overline{d}_2, \ldots, \overline{d}_{n-1}) \\ &\text{subject to } \overline{d}_n = \overline{d}_{tot} - \sum_{i=1}^{n-1} \overline{d}_i \end{aligned} \tag{3.6}$$

This optimization problem is solved using a local optimization algorithm (the interior-point algorithm using the *fmincon* function in MATLAB). Using a local minimization algorithm is critical; during loading the architected material does not switch to a state that corresponds to the global minimum but remains in the neighborhood of the current configuration.

Once the values of $\overline{d}_i$ are obtained at all steps for the loading (or unloading), the values of $\overline{d}_i$ can be plotted as a function of $\overline{d}_{tot}$ to analyze the sequence of deformed configurations the architected material goes through when the loading parameter is increased. In the case of a architected material with 2 unit cells in series, the curve of $\overline{d}_1$ as a function of $\overline{d}_{tot}$ completely characterizes how the material deforms during loading. This curve will be called the deformation path of the architected material.

Besides using the above method to determine the snapping sequence of multilayer architected materials with snap-through instabilities, we can also utilize the critical force contour plot of single unit cells (shown in Fig. 2.5D) to qualitatively figure out the snapping sequence for a multilayer architected materials with different geometric designs. Because the critical force corresponds to the start of the negative stiffness region, the unit cell with the smallest critical force value would snap earlier than unit cells with larger critical force. Based on this assumption, the snapping sequence can be determined by finding the order of critical forces of the unit cells in different layers. For example, if the critical forces of unit cells in layers i, j, k have the following relationship, $f_{cr,i} < f_{cr,j} < f_{cr,k}$, then layer i snaps first, then layer j snaps, and finally layer k snaps.

3.3 Experimental methods and finite element model

The theoretical model was validated using experiments and finite element simulations. The fabrication of samples, mechanical testing methods, and the finite element models are described in this section.

3.3.1 Experimental methods

Samples were fabricated using a multimaterial 3D printer (Objet Connex 260, Stratasys, Edina, MN, USA, shown in Fig. 3.3, located in the Laboratory for Mechanics of Soft Active Materials and 3D printing at Georgia Tech). The printing material is DM9895, which is a digital material derived by mixing two base materials. One of the two base materials is TangoblackPlus, which is a rubbery material at room temperature; the other one is Verowhite, which is a rigid plastic at room temperature. The in-plane dimensions of the printed samples are about 10cm $\times$ 10cm; the out-of-plane thickness is 1cm.

FIG. 3.3. 3D printer used to print samples (Objet Connex 260)

In order to determine the deformation sequences of printed samples, compression tests were conducted on a universal Material Testing System (MTS, Model Insight 10, Eden Prairie, MN, USA) in a displacement control manner with a 10kN load cell. The samples were compressed (at room temperature) using a customized compression fixture at a testing velocity of 10mm/min until all unit cells collapse. A digital camera was used to record the whole testing process.

3.3.2 Finite element model

The corresponding finite element model with elastic constitutive model was built using the "Static/General" nonlinear procedure in Abaqus/Standard. The FEA model is built with 4-node bilinear quadrilateral plane-stress element with reduced integration (CPS4R in Abaqus) and an elastic, isotropic constitutive model. The boundary conditions are shown in Fig. 3.2, *i.e.*, the bottom edge of unit cell 1 is fixed, the left and right sides of these unit cells have a fixed x-direction displacement, and the top edge of unit cell n also has a fixed x-direction displacement. The model was simulated using displacement control, such that the vertical (y) displacement on the top edge of the model is prescribed. The deformation path and the force vs. deformation curves predicted by a static nonlinear FEA simulation with displacement control are used to validate the theoretical model. Moreover, considering the viscoelasticity of the printed samples, FEA models with a viscoelastic constitutive model were also built for comparisons with the experiments. The response to stimulation of the architected materials at a constant strain rate was simulated using nonlinear quasi-static FEA simulations (VISCO procedure in ABAQUS) with displacement control.

3.4 Results and discussion

3.4.1 Analysis of the strain energy landscape for architected materials with identical unit cells

Based on the theoretical model described in Section 3.2, the total strain energy contours of a architected material with two identical unit cells in series can be obtained as a function of $\bar{d}_{tot}$ and $\overline{d}_1$, as shown in Fig. 3.4. The strain energy contours show that there are four local minima, A, B, C, and D (that correspond to stable equilibria) and one local maximum of the total strain energy (that corresponds to an unstable equilibrium). The presence of multiple minima indicates the multistability of this architected material. The global minimum A is the initial undeformed configuration. The local minima B and C correspond to cases when only unit cell 2 has collapsed and only unit cell 1 has collapsed, respectively. The local minimum D is when both unit cell 1 and unit cell 2 have collapsed. Because the two unit cells are identical , the local minima B and C have the same strain energy value, which means the deformation path (the curve $\overline{d}_1(\overline{d}_{tot})$) during loading can follow the sequence A-B-D or A-C-D. In an experiment, the presence of imperfections, for example caused by the manufacturing process or in the experimental setup (for instance in the application of the boundary conditions), would determine which of the deformation paths is preferred (as observed in Fig. 3.1).

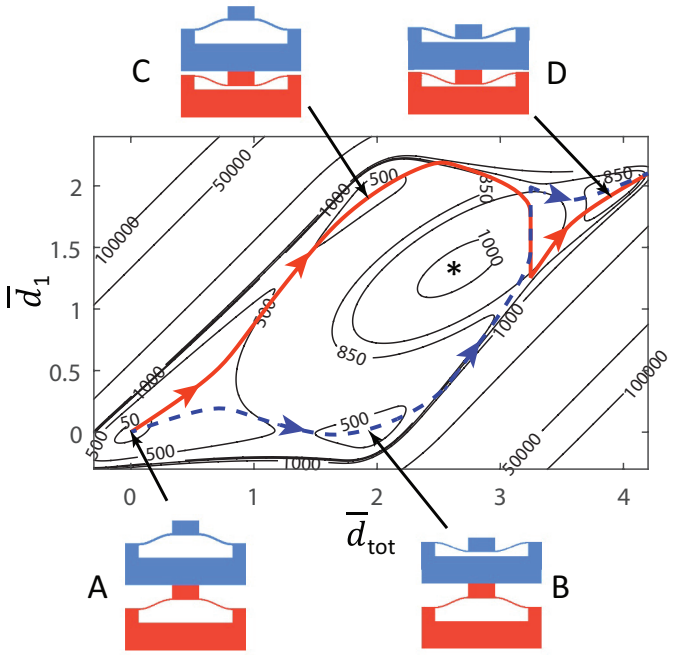

FIG. 3.4. Contour plot of normalized total strain energy for two identical unit cells in series as a function of the normalized deformations $\overline{d}_{tot}$ and $\overline{d}_1$ ($*$ denotes the local maximum), the numerical values on the contour lines correspond to the values of the normalized strain energy $\overline{U}_{tot}$. The red solid line corresponds to one of the possible deformation paths during loading, the blue dashed line corresponds to the other possible path.

3.4.2 Varying the thickness to obtain a deterministic snapping sequence

If geometric variations are applied to the unit cells of the above bilayer architected materials, four unique local minima with different strain energy values can be obtained. Before analyzing the bilayer architected materials, the nonlinear mechanics of single unit cells with different thickness in curved parts were analyzed using the theoretical model described in Section 2.2 of Chapter 2. The relationship between the thickness of the curved parts in unit cell 1 and unit cell 2 is $t_2 = 1.5t_1$. The results for single unit cells shown in Fig. 3.5 demonstrate that the critical force of unit cell 2, $f_{cr,2}$, is higher than the critical force of unit cell 1, $f_{cr,1}$, which means unit cell 2 requires a larger loading force to collapse. Moreover, the strain energy of unit cell 2 is also greater than that of unit cell 1.

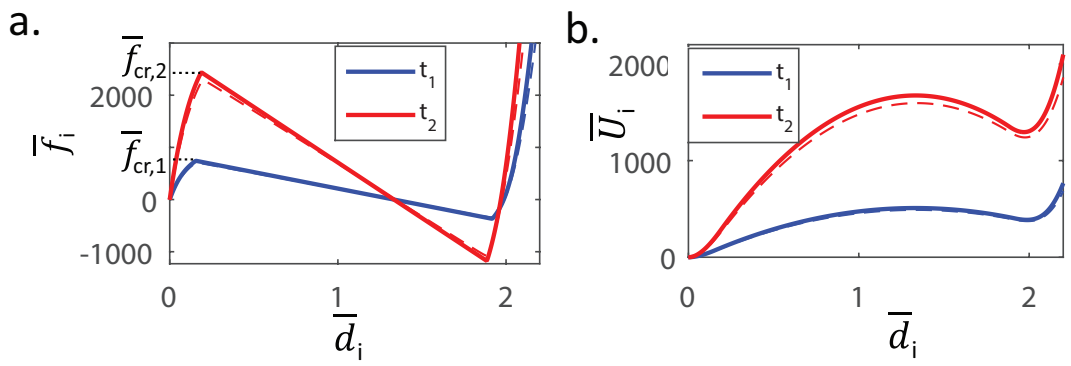

FIG. 3.5. Results for single unit cell with different thickness. a. Normalized force vs. deformation curves for single unit cells of different thicknesses. b. Normalized strain energy vs. deformation curves for single unit cells of different thicknesses. In a and b, solid lines correspond to the theoretical model and dashed lines to FEA simulations.

Results of single unit cells, the theoretical model described in Section 3.2 can be employed to analyze a two-layer architected material with the above two unit cells combined in series. The theoretical results for the total strain energy contour, deformation path and normalized force vs. deformation curves can be determined as the red lines in Fig. 3.6a, 3.6b, and 3.6c, respectively. As shown in the contour plot of the total strain energy for this architected material (Fig. 3.6a), the four local minima of the strain energy are different, such that a unique deformation path is obtained. In order to validate the theoretical results, the simulation results for the corresponding FEA model are given in Fig. 3.6b-3.6c, as the blue dashed lines. Note the excellent agreement for the deformation path between the theoretical model and the FEA simulation (Fig. 3.6b). Both the theoretical model and the FEA simulation show that the deformation sequence is A-C-D for loading and D-B-A for unloading. This also agrees with the critical force relationship of this two unit cells $f_{cr,1} < f_{cr,2}$, *i.e.*, bottom unit cell snaps first, then the top unit cell snaps. As shown in Fig. 3.6a and 3.6b, when the normalized total deformation $\bar{d}_{tot}$ is about 3.4, there will be one snap-back of unit cell 1 (i.e., the value of d_1 drops instantaneously) during loading when unit cell 2 snaps through. In the normalized force vs normalized deformation curve shown in Fig. 3.6c, the first peak has a smaller amplitude than the second peak due to the lower stiffness of unit cell 1; futhermore, the force goes below the horizontal axis (which means a

tensile force is observed) twice during loading.

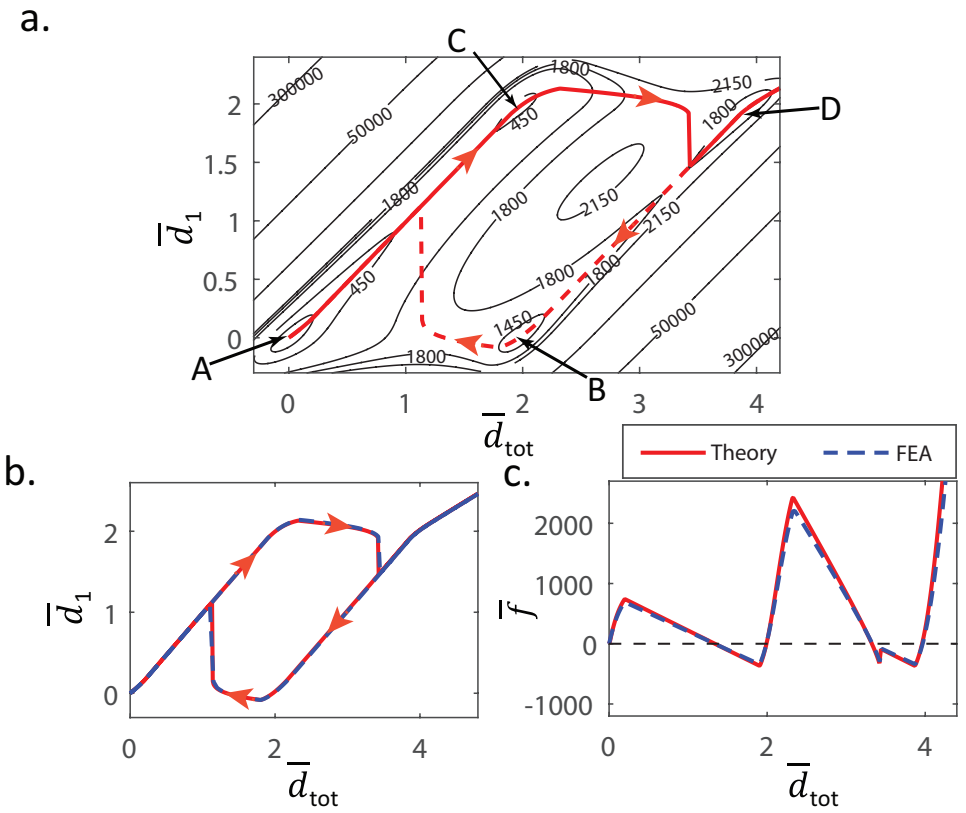

FIG. 3.6. Theoretical analysis of the effect of varying the thickness from row to row on the deformation path. a. Contours of the total strain energy of a architected material with two unit cells with different thicknesses. The deformation path obtained using the theoretical model is shown for loading (solid red line) and unloading (dashed red line). b. Comparison between the deformation paths of the architected material obtained using the theoretical model and FEA simulations. c. Normalized force vs. normalized total deformation (for loading only).

3.4.3 Using mode shape imperfection to obtain a deterministic snapping sequence

Besides the method of varying the thickness, the snapping sequence can also be tuned by varying the mode shape imperfection size a_3 (where the imperfection in the initial shape of the beam, $\delta W(x)$, is given by Eq. 2.6). Consider the architected material with two unit cells in series, where unit cell 2 is perfect ($a_{3,2} = 0$) and unit cell 1 has a 10% third mode imperfection ($a_{3,1} = 0.1$) as shown in Fig. 3.7a. The nonlinear mechanics of single unit cells

with mode shape imperfection size a_3 were analyzed using theoretical model described in Section 2.2 of Chapter 2. The results are shown in Fig. 3.7b-c. The results of both the theoretical model and FEA simulations show that the critical loading force and the strain energy of a single unit cell decrease when the model has a 3^{rd} mode imperfection.

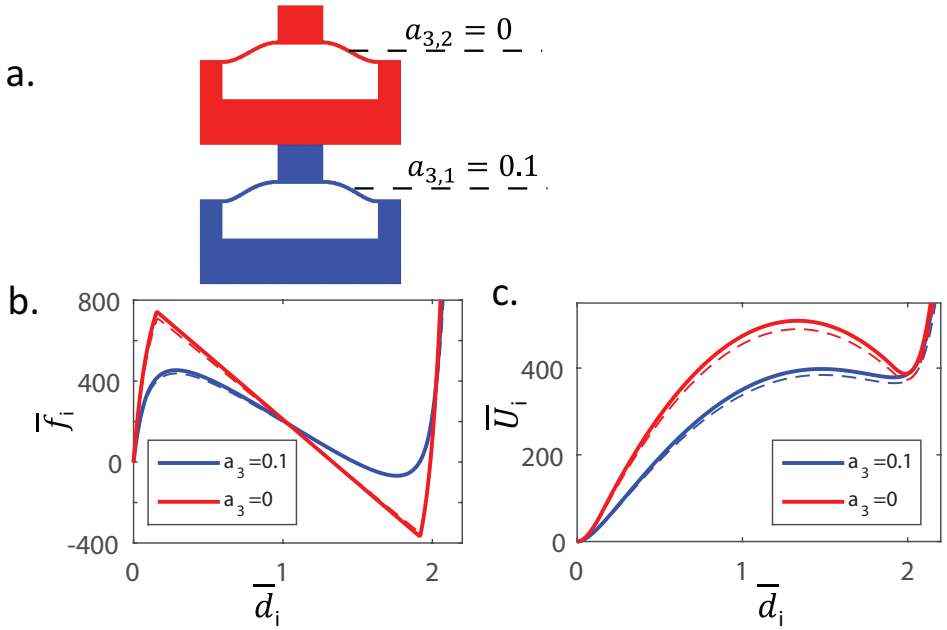

FIG. 3.7. Influence of mode shape imperfection on the mechanics of single unit cell. a. Architected material with two unit cells in series: unit cell 2 has no mode shape imperfection ($a_{3,2} = 0$), unit cell 1 has a 3^{rd} mode shape imperfection ($a_{3,1} = 0.1$). b. and c. Comparison curves of normalized force vs. deformation and normalized strain energy vs. deformation for single unit cell 2 with $a_3 = 0$ and unit cell 1 with $a_3 = 0.1$ (solid lines are theoretical results, dashed lines are results from FEA).

With the results of single unit cells, the theoretical model described in Section 3.2 can be employed to analyze the architected material shown in Fig. 3.7a. In contrast to the case of identical unit cells, the local minima of the strain energy are different, which makes the deformation path unique (Fig. 3.8a). The deformation sequence is A-C-D for loading, and D-B-A for unloading. As in the case of the architected material with two cells that have different thicknesses, there will be one snap-back of the unit cell 1 during the initial snap-through of unit cell 2 (Fig. 3.8a), when the normalized total deformation $\bar{d}_{tot}$ is about 3.3. As observed in Fig. 3.8c, the first peak in the normalized force vs normalized deformation

curve has a smaller amplitude due to the smaller critical force in unit cell 1 (Fig. 3.8c); furthermore, a tensile force is observed twice during the loading. However, in contrast to the case of the thickness variation, the first peak has a smoother shape than the second peak because adding an imperfection significantly affects the shape of the normalized deflection vs normalized deformation curve for a single unit cell (see Fig. 3.7b).

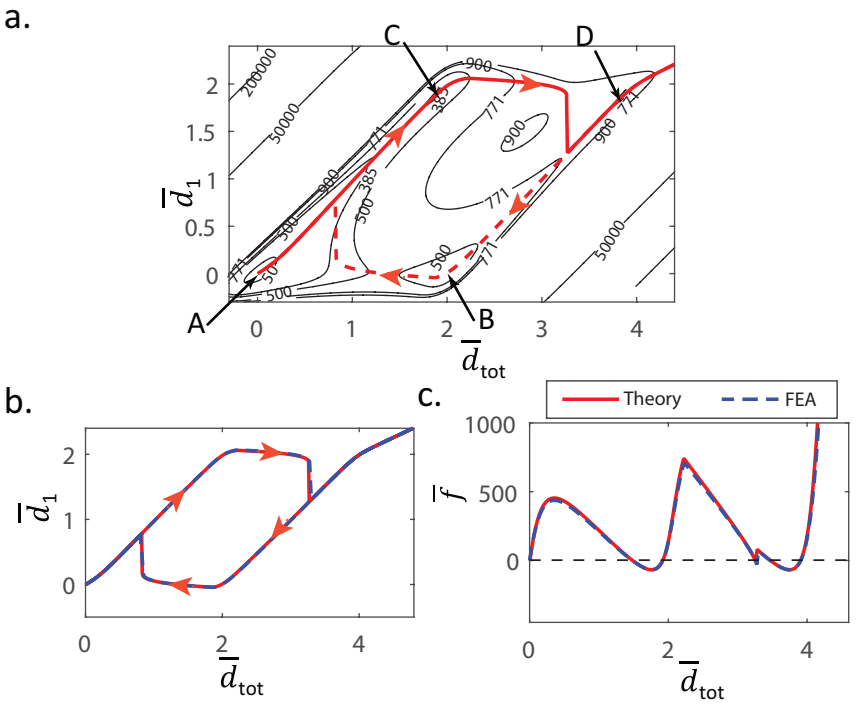

FIG. 3.8. Theoretical analysis of the effect of mode shape imperfection on the deformation path. a. Contour plot of total strain energy for the architeced material with two unit cells (shown in Fig. 3.7a). The deformation path obtained using the theoretical model is shown for loading (solid red line) and unloading (dashed red line). b. Comparison between the deformation paths of the architected material (shown in a) obtained using the theoretical model and FEA simulations. c. Normalized force vs. normalized total deformation (for loading only).

3.4.4 Experimental validation

3.4.4.1 Qualitative validation: snapping sequence

Several multilayer architectures were fabricated using a 3D printing technique. These samples were tested using a customized compression fixture to experimentally validate that the

methods of thickness variation and mode shape imperfection can be used to tune the deformation sequence.

One of the printed samples is the multistable architected material shown in Fig. 3.9a (architected material A), which consists of 5 rows, each with 5 unit cells (in the rest of this thesis, we will call a architected material with N rows, each with M unit cells as an $N \times M$ architected material). For this 5×5 multilayer architected material, the thickness is constant within each row, while the thickness varies from row to row ($t_1 < t_5 < t_2 < t_3 < t_4$, where the unit cells are ordered from bottom to top). From the critical force contour plot shown in Fig. 3.9b, we can determin the relationship of the critical forces of different layers, $f_{cr,1} < f_{cr,5} < f_{cr,2} < f_{cr,3} < f_{cr,4}$. Then the snapping sequence should be, row 1 collapses first, then row 5, row 2, row 3, and row 4. This result is validated by experiments and FEA simulations. Fig. 3.9c-d shows snapshots of the response of the multilayer architecture at different effective strains ϵ for both experiment and finite element simulation. These snapshots demonstrate that the deformation sequence matches what is expected from the previous analysis (*i.e.*, row 1 collapses first, then row 5, row 2, row 3, and row 4).

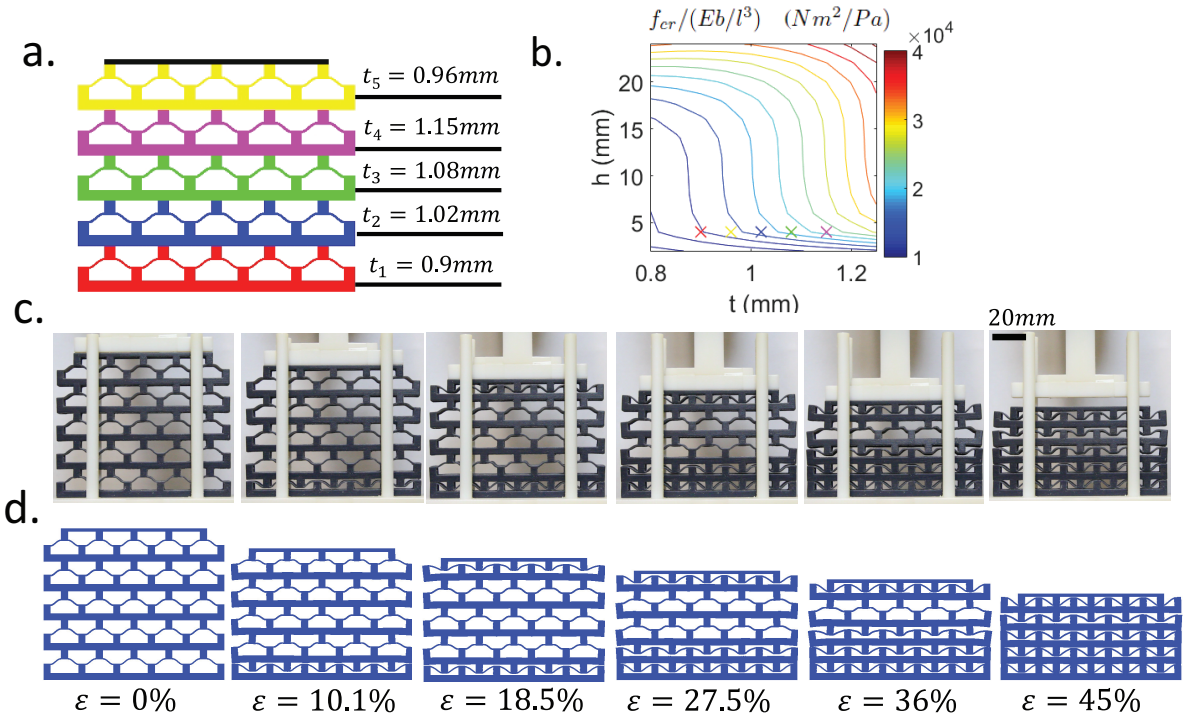

FIG. 3.9. Experimental validation of the method of thickness variation to obtain a deterministic deformation sequence (architected material A). a. 5×5 multilayer architected material with unit cells of thickness t varies from row to row. b. The critical force contour for single unit cells (the cross points represents the unit cells from architected material A with corresponding colors). c. and d. Snapshots of the multilayer architecture at different values of the effective strain ϵ (c. Experiment, d. FEA).

Another printed sample is the 5×5 multilayer architected material shown in Fig. 3.10a (architected material B). The unit cells of this 5×5 architected material have a uniform mode imperfection size within each row, but the imperfection size varies from row to row. The thickness of each unit cell's curved part is 1mm. Snapshots of the response at different strains ϵ for both experiment and finite element simulation (Fig. 3.10b-c) demonstrate that the deformation sequence matches the expected sequence (*i.e.*, row 1 collapses first, then row 5, row 2, row 3, and row 4).

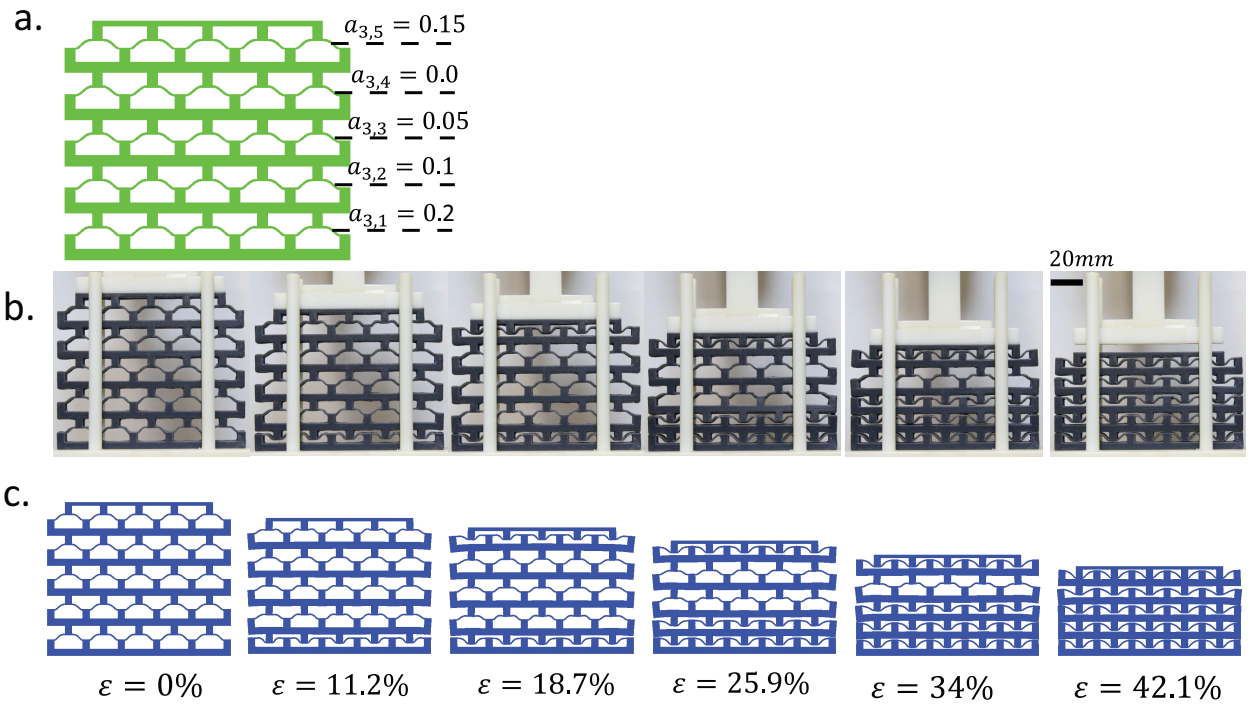

FIG. 3.10. Experimental validation of the method of mode shape imperfection to obtain a deterministic snapping sequence (architected material B). a. 5×5 multilayer architected material with unit cells of mode imperfection size a_3 varies from row to row. b. and c. Snapshots of the multilayer architecture at different values of the effective strain ϵ (b. Experiment, c. FEA).

3.4.4.2 Quantitative comparisons

The experiments were also analyzed more quantitatively by plotting the value of the normalized deformation of each unit cell, $\bar{d}_i$, as a function of the total deformation, $\bar{d}$, in Fig. 3.11a and b. The normalized deformation was computing using frames of the movies recorded using the digital camera during the compression test. For the experiments, FEA simulations and theoretical model, the same clear deformation sequence can be seen by inspecting the results (*i.e.*, row 1 collapses first, then row 5, row 2, row 3, and row 4 in both Fig. 3.11a and b). While both the FEA simulations and the theoretical model are able to qualitatively capture the deformation sequence, only the FEA simulations are able to quantitatively match the experiments. In particular, the unit cells in the theoretical model deform earlier than in the FEA models and experiments. Moreover, there is an instantaneous snap-back in theoretical

model; however, a more gradual and limited snap-back is observed in the FEA model and in experiments (for example see $\epsilon = 18\%$ for $\overline{d}_1$ in Fig. 3.11a and $\epsilon = 15\%$ for $\overline{d}_1$ in Fig. 3.11b). The inaccuracies of the theoretical model are due to two sources: (1) the viscoelasticity of the printed materials and (2) the assumption regarding the kinematics in the theoretical model (a small rotation assumption is used and parts of the unit cell are assumed to be rigid). The smoothing of the curves seen the experiments and FEA simulations (with a viscoelastic model) are primarily due to the viscoelasticity of the printed samples. Simulations with finite element with an elastic constitutive model (not shown) do show a discontinuous instability jump that is similar to what is seen in the theoretical model. In spite of the quantitative differences between theory and experiments, the theoretical model does capture the important characteristics of the deformation paths of this multistable architected material and can be used to inform the design of architected materials with a deterministic deformation sequence.

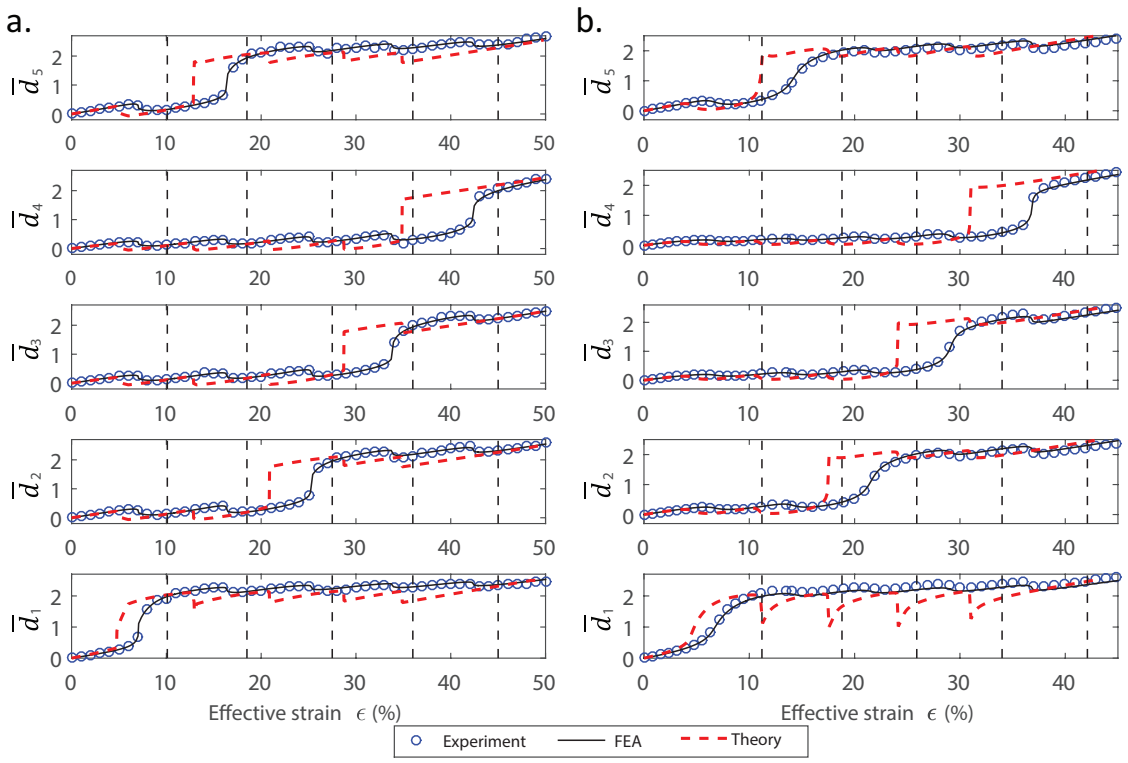

FIG. 3.11. Quantitative analysis of the deformation sequence. a. Architected material A (see Fig. 3.9a). b. Architected material B (see Fig. 3.10a). $\overline{d}_i$ is the normalized deformation of row i defined as Eq. 3.4. The dashed black vertical lines are corresponding to the effective strains of the snapshots in Fig. 3.9 and Fig. 3.10.

The effective stress vs. strain curve was also obtained during the compression test and compared with the FEA model with viscoelastic material as shown in Fig. 3.12a and c. The effective stress is calculated from the compression force divided by the bottom area of the model, and the effective strain is calculated from the total deformation divided by the initial height of the model. For both architected materials, there is good quantitative agreement between experiments and FEA simulation results. This excellent quantitative agreement is interesting because of the difference in the boundary conditions applied in the FEA and in the experiments: the top edge of the sample was prescribed to move at a constant velocity in the FEA simulations; in the experiments, the top edge of the compression fixture was prescribed to move at a constant velocity and the top edge of the sample was not attached to the compression fixture. In the case of an elastic sample, a separation of the top edge

of the sample from the compression fixture would have been expected when one the row of the samples snap-through. However, the presence of viscoelasticity significantly affects the kinetics of the snap-through process, such that the sample remains in contact with the compression fixture. The experiments and FEA simulations with a viscoelastic constitutive model do not show that the force crosses the horizontal axis, which could be wrongly interpreted as the absence of multistability. However, the multistability was experimentally verified by letting the architected material relax to any of the expected stable configurations. Furthermore, the first peak has a higher amplitude than the second peak, in contrast to what has been observed in Figs. 3.6 and 3.8.

Because of the viscoelasticity of the 3D printed sample, the theoretical model cannot be directly compared to the experiments or the FEA simulations with a viscoelastic material; hence, the theoretical model was compared to FEA simulations with an elastic constitutive model (Fig. 3.12b and d). For both architected materials, the theoretical result has excellent agreement with the FEA with elastic constitutive model and captures the major characteristics of this architected material, showing its multistability (*i.e.*, crossings of the horizontal axis) and growing stress peaks. This implies that the absence of a tensile force and the fact that the second stress peak has a lower amplitude than the first peak are due to the viscoelasticity of the 3D printed samples (note, however, that obtaining a tensile force would also require to use an adhesive between the compression fixture and the sample, as done for example in[4]). Because of the assumption of small rotation, some parts being rigid in the theoretical model, the values of the strain corresponding to maxima and minima are somewhat shifted in the theoretical model compared to FEA with an elastic constitutive model.

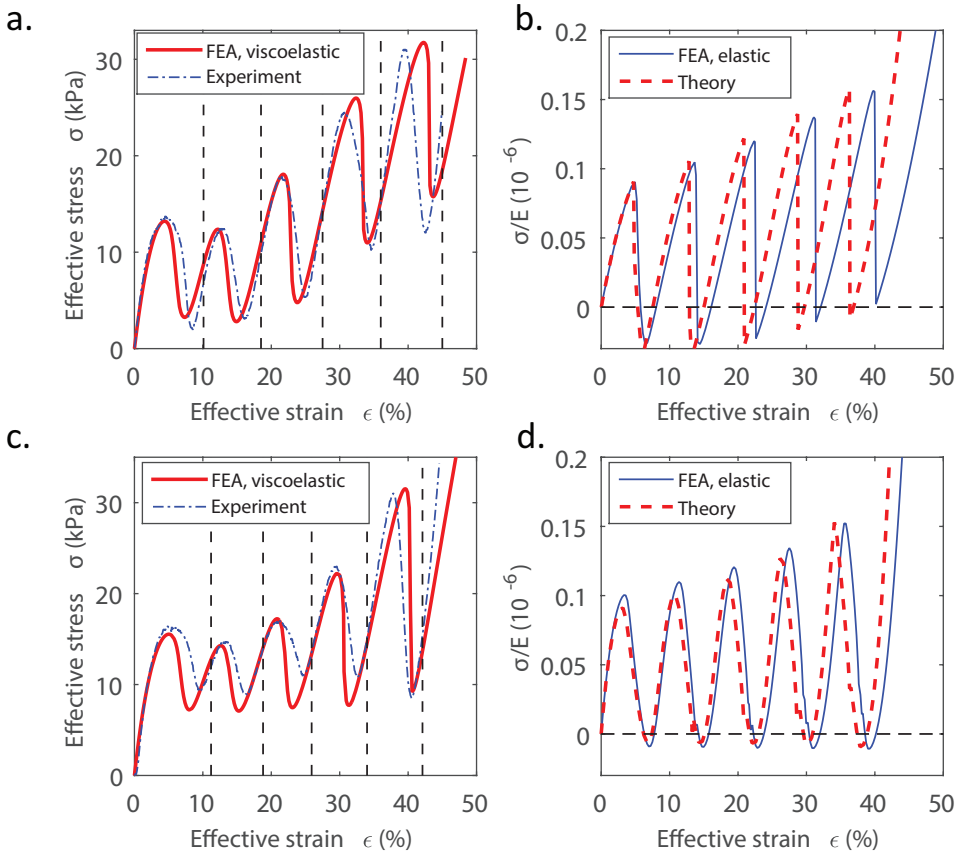

FIG. 3.12. Stress vs. strain curves for architected material A (a and b) and for architected material B (c and d). In a and c, experimental data is compared to FEA with a viscoelastic constitutive model. In b and d, the theoretical model is compared to FEA simulations using an elastic constitutive model.

3.5 Summary

In this chapter, small geometric variations were utilized to tune the deformation sequence of one kind of architected material with snap-through instabilities that consists of a quasi-periodic microarchitecture. This work overcomes the limit shown in previous studies that when the unit cells used in a multistable architected material are identical, the stable configuration that the architected material switches to is unpredictable due to the effects of imperfections in the manufacturing process and in the boundary conditions. Two different methods were analyzed and used to obtain a deterministic snapping sequence: (1) the thickness t of each layer was varied; (2) higher mode shape imperfections were introduced

into the initial shape of the curved part of the unit cells. In order to obtain a deterministic snapping sequence, a rigorous theoretical model was developed to analyze the mechanics of multistable architected materail and help to design this architected material. The novel theoretical model was validated by comparison to finite element simulations of a model that consists of multiple bistable unit cells in series. Both the loading and unloading response of the theoretical model are in excellent agreement with finite element simulations.

The results of finite element simulations and experiments on 3D printed samples confirm that the snapping sequence of multiple unit cells can be tuned either by varying the thickness or by introducing higher mode shape imperfections to the unit cell curved parts. Despite viscoelasticity, which is not taken into account in the theoretical model, the theory does predict the experimentally observed snapping sequence. Excellent quantitative match between experiments and FEA simulations is observed when viscoelasticity is taken into account. Despite the presence of manufacturing imperfections, a deterministic deformation sequence is obtained for thickness variations or mode shape imperfections of moderate sizes. The validity of the proposed model was demonstrated for systems with a small number of unit cells and with simple variations in the model parameters. However, the proposed model is general and could be applied to more complex architected materials with a large number of unit cells with spatial variations in multiple geometrical and material parameters and might be particularly useful for the analysis of multistable materials of larger sizes, which could be useful for the design multifunctional architected materials with programmable and switchable properties.

Chapter 4

Viscoelastic multistable architected materials with temperature-dependent snapping sequence

4.1 Introduction

Chapter 3 demonstrated that a deterministic snapping sequences for architected materials with snap-through instabilities can be obtained by employing geometric variations in the unit cells. However, the snapping sequence is predefined and cannot change after the fabrication of the architected materials. In order to overcome this limitation and to improve the architected material's tunability, multimaterial viscoelastic architected materials were developed; these architected materials have a snapping sequence that can be reversibly tuned using temperature as a control parameter.

The novel idea of this chapter is based on the fact that different polymers have different time dependent and temperature dependent responses. Thus it is possible that one polymer is stiffer at low temperature (or high strain rate) but becomes softer than the other polymer when the temperature decreases (or strain rate decreases). By properly integrating these

polymers into a periodic structure, the crossover of the relative stiffness could give dramatic different responses of architected materials to compressive loading at different temperature or different strain rate, which also makes it possible to obtain reconfigurable arhitected materials with controllable snapping sequences[108].

In this chapter, the design and fabrication of multimaterial architected materials are first presented. Then how temperature utilized to obtain controllable snapping sequence is investigated and discussed using FEA simulation and experiments. Moreover, one potential application of these architected materials as soft reconfigurable architected materials with tunable stiffness is demonstrated.

4.2 Design and fabrication of multimaterial architected materials with snap-through instabilities

In this chapter, the studied architected materials also consist of N layers (in series) of unit cells with snap-through instabilities. In contrast to the architected materials in Chapter 3 made up of only one material, the different layers of the architected material are made of different materials. For example, for the architected materials shown in Figs. 4.1A, the top layer(s) is (are) made of PEGDA while the other layer(s) is (are) made of a 3D printed polymer, DM8995 (a digital material made of the mixture of two base materials; we will refer to DM8995 as DM hereafter).

A.

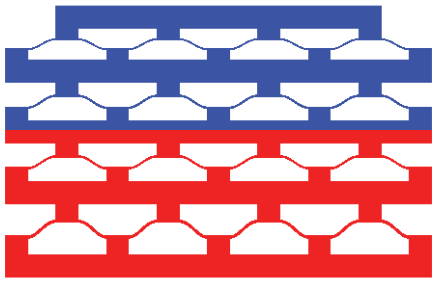

B.

Geometrical parameter	Value
t	t_0~$2t_0$
h	Qt
L	Pt
T	$11.6t_0$
H	$6t_0$
w	$5.8t_0$

FIG. 4.1. Bi-material architected materials with snap-through instabilities. A. Example of 4-layer architected material ($N = 4$). B.Values of unit cell's geometric parameters. Fabricated samples use $t_0 = 0.25$mm and an out-of-plane thickness of 6mm.

3D printing is commonly utilized to create structures with complicated geometries. However, a very limited number of materials can be 3D printed, which limits the applications of 3D printing to multimaterial reconfigurable architected materials. While the polyjet based method allows three or more materials to be printed simultaneously, the number of available materials in the polyjet based method is extremely limited (for example less than 10 polymers for the newest 3D printer models of the Stratasys Objet Connex series polyjet 3D printers).

To have more freedom in the material choice, a facile 3D printing inverse molding process (Fig. 4.2A) was implemented. A periodic structure was first printed by the same 3D printer used in Chapter 3. The material used is the same 3D printed material (DM) as in Chapter 3. The printed periodic structure was used as a positive mold to make a PDMS mold (end of Step 1). The PDMS mold was then used to replicate the periodic structure, but with different materials. In the example shown in Fig. 4.2, half of the mold was first filled with a 3D printed half structure made of DM; the rest of the space was then filled by a photocurable Poly(ethylene glycol) diacrylate (PEGDA) resin. After curing, a bi-material architected material (Fig. 4.2B) was obtained. The advantage of this approach is that it removes the material choice constraints imposed by 3D printing. For example, one is able to select PEGDA, whose dependence of storage modulus on the temperature crosses that of 3D

printed materials (see Fig. 4.3A); such a crossover renders very exciting behaviors, which could not be achieved if one solely relies on the 3D printed materials.

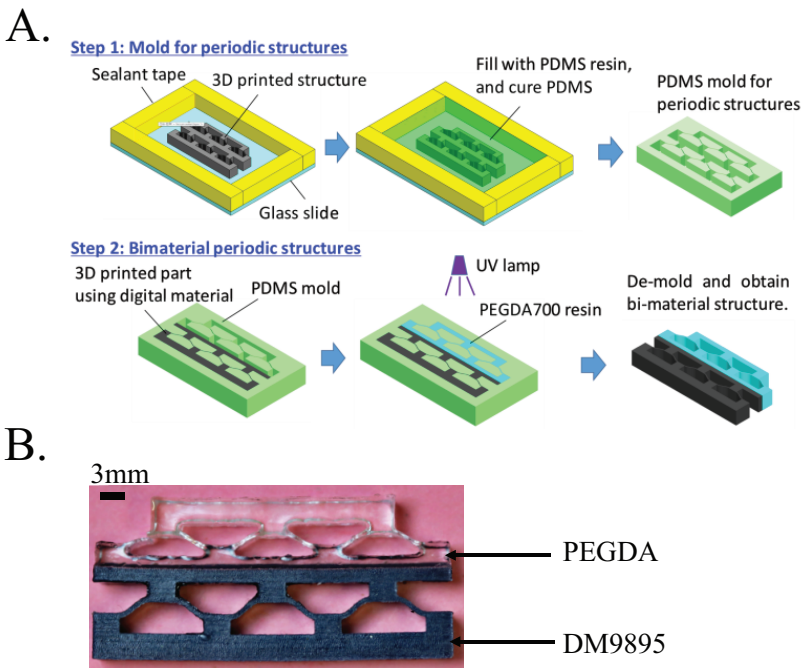

FIG. 4.2. A. Fabrication process for multimaterial architected materials. B. Example of bi-material fabricated sample.

4.3 Mechanical testing and finite element models

The sample were compressed at a constant velocity $v = 10\text{mm/min}$ using the same universal Material Testing System as used in Chapter 3. The experiments were conducted in a temperature controlled box. For experiments that were conducted at temperature above room temperature, the temperature was first increased, then held for 10 min (such that the temperature of the sample reaches its steady-state value) before doing the compression test.

Besides compression experiments, the mechanics of these multistable architected materials were analyzed using two-dimensional finite element models. 4-node bilinear quadrilateral plane-stress elements with reduced integration (CPS4R in Abaqus) were used. Self-contact normal interactions were defined for the whole model. Because the modulus of PEDGA is almost temperature-independent in the temperature range that was considered (see Fig.

4.3A), PEDGA was modeled as an isotropic, elastic constitutive material. An isotropic, thermo-viscoelastic constitutive model was used for DM since its modulus is temperature-dependent (see Fig. 4.3A). For this thermo-viscoelastic model, the temperature-dependent relaxation modulus, $E(t,T)$, is expressed as a Prony series of the form:

$$E(t,T) = E_{eq}(T) + \sum_{i=1}^{n} E_i \exp\Big[-\frac{t}{\tau_i(T)}\Big] \tag{4.1}$$

4.4 Results and discussion

4.4.1 The snapping sequence can be tuned using temperature

Bilayer samples (Fig. 4.3B) made of PEDGA and DM were fabricated using the inverse molding process described in Section 4.2. The two materials, PEDGA and DM, were chosen because their storage moduli cross over at a temperature near room temperature, at about 32^oC (Fig. 4.3A). This cross-over in the stiffness of the two layers is the physical basis for the temperature-dependent switch in the snapping sequence. The critical force of the DM layer decreases as the temperature T is increased according to the theoretical results of Chapter 2. The bilayer samples were compressed by moving a loading cell at a constant velocity. When a bilayer sample is compressed, the layer with the lower stiffness snaps before the other layer snaps. Hence, due to the temperature-dependent modulus of DM, the snapping sequence (which layer snaps first and second) can be tuned by temperature: at room temperature (T=20^oC), DM is much stiffer than PEDGA (Fig. 4.3A), therefore, the top layer (L2) snaps first (as seen in Fig. 4.3c); however, the snapping sequence changes when the compression test is conducted at 50^oC, where DM is softer than PEGDA (Fig. 4.3A) and the bottom layer (L1) snaps first (as seen in Fig. 4.3E). To more quantitatively evaluate the snapping

sequence, the deformation of bottom layer, $d_1(\varepsilon)$, and top layer, $d_2(\varepsilon)$, were calculated using:

$$\begin{aligned} d_1(\varepsilon) &= u_1(\varepsilon) \\ d_2(\epsilon) &= u_2(\varepsilon) - u_1(\varepsilon) \end{aligned} \tag{4.2}$$

where $u_1(\varepsilon)$ and $u_2(\varepsilon)$ are the displacements of bottom layer and top layer, respectively (shown in Fig. 4.3B) and ε is the effective strain (computed using $\varepsilon = u_2/h_{tot}$ where h_{tot} is the total height of the sample). At low temperature, it is observed that the value of d_2 rises before the value of d_1, while the opposite trend is observed at high temperature. While the snapping of each layer would be instantaneous if elastic materials would be used, the snapping of each layer is more gradual here due to the presence of viscoelasticity. Comparison of the experimental results to finite element simulations demonstrates that finite element simulations agree very well with the experiments both at the low (Fig. 4.3D) and high (Fig. 4.3F) temperatures.

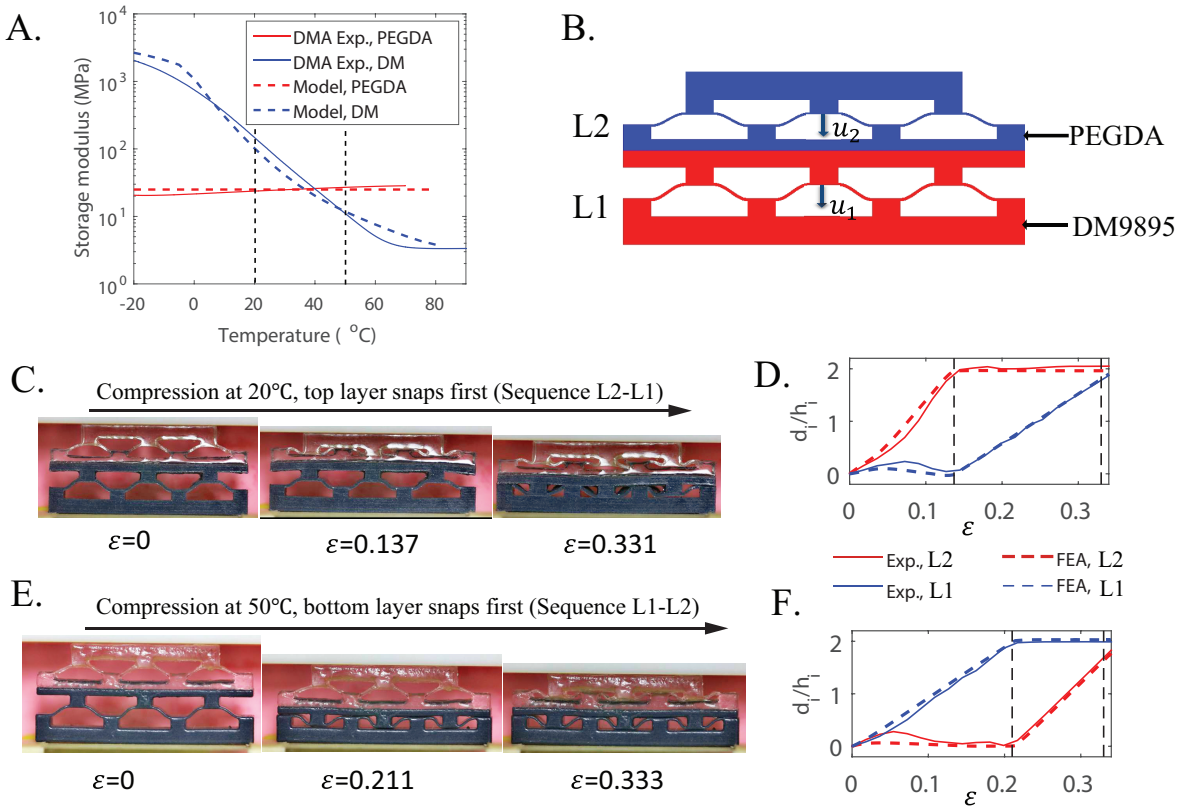

FIG. 4.3. Tuning the snapping sequence using temperature. A. Storage modulus vs temperature for PEDGA and DM at 1Hz. B. Schematics of bilayer sample. u_1 and u_2 are the displacements of the bottom and top layers, respectively. C. and E. Snapshots of the compression tests at 20^{o}C and 50^{o}C. D. and F. Comparison of the normalized deformation for the bottom layer, d_1/h_1, and top layer, d_2/h_2, at 20^{o}C and 50^{o}C. The vertical dashed lines corresponds to the effective strain value in the snapshots of panels C and E.

4.4.2 Influence of the geometrical parameters on the critical temperature

Because of the high fidelity of the finite element simulations, the influence of the geometrical parameters on the snapping sequence was systematically studied using finite element simulations. The temperature at which the snapping sequence switches from the sequence observed at room temperature (*i.e.*, the PEDGA layer snaps first) to the sequence observed at high temperature (*i.e.*, the DM layer snaps first) was defined to be the critical temperature, T_{cr}. The value of the curved part of the unit cell, t (see Fig. 4.1b), significantly influences the

stiffness of the unit cell. Hence, we analyzed the influence on T_{cr} of the ratio of the t value for the DM layer, t_1, to the t value for the PEDGA layer, t_2. For these simulations, t_2 was kept constant while t_1 was varied between t_2 and 1.65 $\times t_2$.

The numerical results shown in Fig. 4.4 demonstrate that the critical temperature increases when t_1/t_2 increases. This is due to the increase in the stiffness of the DM layer relative to the stiffness of the PEDGA layer. When the thickness ratio is high enough ($t_1/t_2 \geq 1.65$), no switching of the snapping sequence is observed: at all temperatures, the top layer (PEDGA) snaps first. This can explained by the fact that the modulus of DM saturates to a constant value at high temperature (Fig. 4.3A). For validation of these numerical results, the transition temperature was also determined experimentally for 22 different samples fabricated using the inverse mold fabrication method. For each sample, tests were repeated at multiple temperatures in order to determine with a 1 degree accuracy the value of the critical temperature. The critical temperature obtained experimentally follow closely the trend observed in the finite element simulations; furthermore, as in the simulations, no switch was observed when $t_1/t_2 \geq 1.65$.

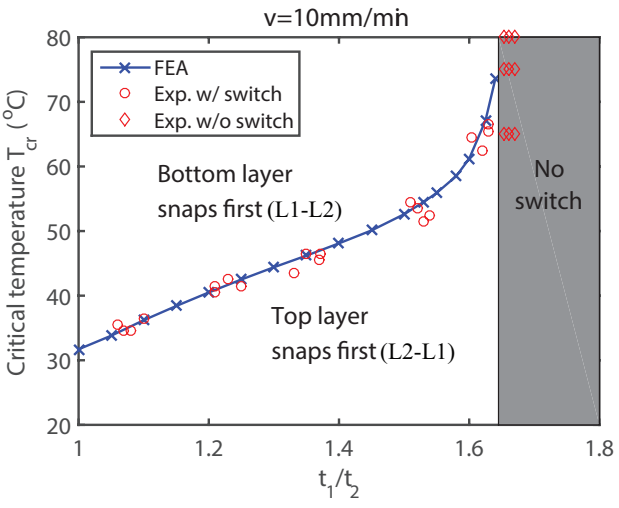

FIG. 4.4. Critical temperature vs thickness ratio: the area above the blue curve means the bottom layer snaps first (snapping sequence is L1 snaps first, then L2 snaps), the area below the blue curve means the top layer snaps first (snapping sequence is L2 snaps first, then L1 snaps), the gray-shaded area means there is no snapping sequence switching snapping sequence is always L2 snaps first, then L1 snaps.

4.4.3 Multiple snapping sequence switchings in N-layer architected materials

The dependence of T_{cr} on the geometrical parameters can be exploited to considerably expand the number of stable configurations that can be obtained in response to a compressive deformation. A multistable architected material with N layers of bistable unit cells in series has a total of $N_{tot} = 2^N$ stable configurations. These stable configurations can be identified by a combination of binary numbers $i_1, ..., i_N$, where i_j (j=1,...,N) corresponds to the stable configuration of layer j (where $i_j = 0$ and $i_j = 1$ correspond to the undeformed and stable configurations, respectively). However, only a small portion of these stable configurations can be obtained by applying a compressive deformation if thermoviscoelastic effects are not exploited: the number of stable configurations obtained at a single temperature using a compressive deformation is only $N_{single} = N + 1$. For example consider the 4-layer sample shown in Fig. 4.5A that consists of two DM layers (layers 1 and 2) and two PEGDA layers (layers 3 and 4). The two DM layers have different t values ($t_1 > t_2$) and the two PEDGA layers have different t values ($t_3 > t_4$). At room temperature, only configurations 0000, 0001, 0111, 0111 and 1111 can be obtained in response to a compressive deformation (Fig. 4.5B). However, because of variations in the t values, four different critical temperatures can be identified: between layers 1 and 3, between layers 1 and 4, between layers 2 and 3 and between layers 2 and 4. Hence, this makes it possible to obtain $N_{seq} = 5$ different snapping sequences, depending on the temperature (Fig. 4.5B), which results in a total of nine different configurations (shown in the last column of Fig. 4.5B) that can be obtained in response to a compressive deformation.

While a higher number of stable configurations could be obtained by applying a more complicated loading history (that includes tensile loads) or by deforming individual layers by stimulating them directly, only configurations that are obtained in response to a compressive load are considered here. More generally, let N_{DM} and N_{PEGDA} be the number of DM layers and PEDGA layers, respectively. Consider one of the DM layers. As the temperature is

increased, this DM layer will exhibit a snapping sequence switch with each of the PEDGA layers, which results in N_{PEGDA} different critical temperatures for this DM layer. Thus, the total number of critical temperature is:

$$N_{cr} = N_{PEGDA} \times N_{DM} \tag{4.3}$$

such that the number of sequences is:

$$N_{seq} = N_{cr} + 1 = N_{PEGDA} \times N_{DM} + 1 \tag{4.4}$$

Since $N = N_{PEGDA} + N_{DM}$, the maximum number of snapping sequences that can be obtained with bi-material architected materials with N layers is:

$$N_{seq,max}(N) = \max_{2 \leq N_{DM} \leq N-1} \{(N - N_{DM})N_{DM} + 1\} = \lfloor \frac{N}{2} \rfloor \lfloor \frac{N+1}{2} \rfloor + 1 \tag{4.5}$$

where $\lfloor . \rfloor$ denotes the floor function. For the snapping sequence obtained at room temperature, $N+1$ different configurations are obtained; furthermore, for each of the $N_{seq} - 1$ other snapping sequences, an additional stable configuration is obtained (see Fig. 5B). Hence, the maximum number of stable configurations that can be obtained by loading a bimaterial architected material at different temperatures is:

$$N_{bimat}(N) = (N+1) + (N_{seq,max}(N) - 1) = \lfloor \frac{N}{2} \rfloor \lfloor \frac{N+1}{2} \rfloor + N + 1 \tag{4.6}$$

As shown in Fig. 4.5C, N_{bimat} is significantly larger than N_{single} for large N values. Exploiting thermoviscoelastic effects make it possible to considerably expand the number of stable configurations that can be obtained in response to compressive loads.

A.

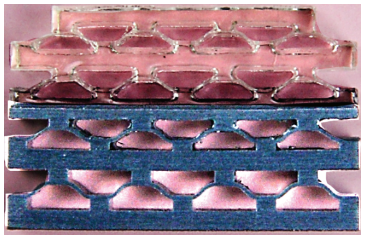

B.

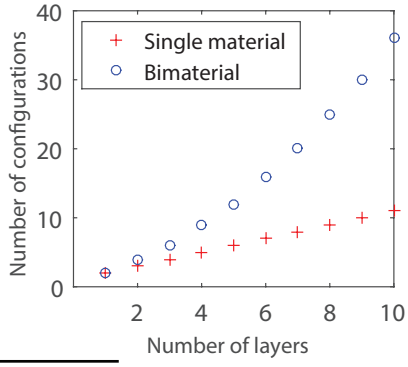

C.

Temperature (°C)	Snapping sequence	Configurations
$T < 31$	L4-L3-L2-L1	0000, 0001, 0011, 0111, 1111
$31 < T < 41$	L4-L2-L3-L1	0000, 0001, 0101, 0111, 1111
$41 < T < 46$	L2-L4-L3-L1	0000, 0100, 0101, 0111, 1111
$46 < T < 62$	L2-L4-L1-L3	0000, 0100, 0101, 1101, 1111
$T > 62$	L2-L1-L4-L3	0000, 0100, 1100, 1101, 1111

FIG. 4.5. A. Example of fabricated sample with 4 layers where $t_2 = t_3 = 1.2t_4$ and $t_1 = 1.6t_4$. B. Snapping sequences and configurations at different temperatures. C. Number of stable configurations obtained in response to compressive deformation as function of the number of layers.

4.4.4 Exploiting temperature-dependent snapping sequences to obtain materials with tunable stiffness

The ability of these architected materials to have multiple stable configurations can be exploited to obtain reconfigurable materials with tunable stiffness. Because these architected materials consist of N layers in series, they can be modeled as 1D chains of nonlinear springs. The effective dynamic stiffness of the architected material in configuration $i_1, ..., i_N$ can be estimated using the equation:

$$k^*_{eff,i_1,...,i_N}(\omega, T) = \Big[\sum_{j=1}^{N} \frac{1}{E^*_j(\omega, T) k_{j,i_j}}\Big]^{-1} \tag{4.7}$$

where k_{j,i_j} is the normalized stiffness of layer j in configuration i_j and E^*_j is the dynamic Young's modulus of the material used for layer j; and * denotes a complex number. k_{j,i_j} was

computed using the analysis of a single elastic layer using the following definition:

$$k_{j,i_j} = \frac{1}{E}\frac{dF}{du}(u_{i_j}) \tag{4.8}$$

where E is the Young's modulus, F is the applied force, u is the deflection of the layer and u_{i_j} is the deflection of the layer in configuration i_j.

The stiffnesses of all the stable configurations that can be obtained by exploiting thermoviscoelasticity in bimaterial architected materials made of 4 layers were analyzed. For the design previously shown in Fig. 4.5A, the stiffness of these nine stable configurations do not vary much (Fig. 4.10C): for example, the difference between the stiffnesses in Configurations 0111 and 1111 is only 2% of the stiffness in Configuration 0000. To obtain a design with highly tunable stiffness values, a wide range of values for the non-dimensional parameters $Q_j = h_j/t_j$ and $P_j = L_j/t_j$ of each layer was considered, as shown in the Fig. 4.6: $2.8 \leq Q_j \leq 5$ and $0.03663 \leq 1/P_j \leq 0.1172$, where each parameter is allowed to take 12 different value. The stiffness values of each individual layer was first calculated using FEA simulations with a Static, Linear perturbation in ABAQUS. As shown in Fig. 4.7, the boundary conditions for the bottom edge of the model are the following: for the top 3 layers, the bottom edge has a fixed vertical displacement and the bottom middle node is fixed in both directions; for the bottom layer, the bottom edge is fixed (since the bottom edge of the 4-layer model is also fixed). For all simulations, a uniformed vertical displacement was applied to the top edge of the model.

The value of the stiffness of individual layers was normalized by $E \times b$ (where E is the Young's modulus and b is the out-of-plane thickness) and plotted as function of P and Q in Fig. 4.8. Using a total of $2 \times 12 \times 12 = 288$ simulations of a single layer of unit cells, the use of Eq. 4.7 made it possible to evaluate the effective stiffness of 4-layer architected material at room temperature of a total of $12^8 = 4.3 \times 10^8$ designs.

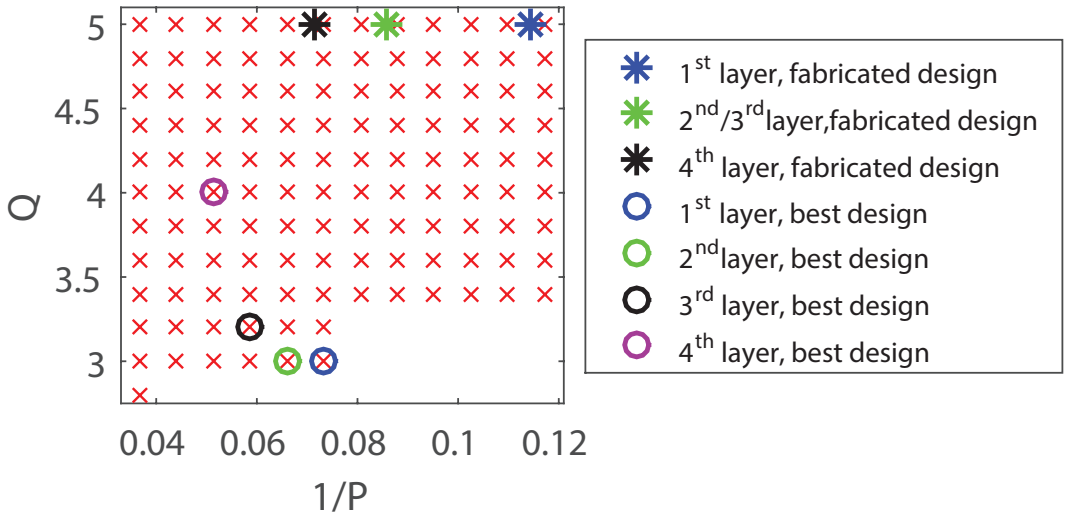

FIG. 4.6. Design space. Each red cross correspond to a value of P_j and Q_j that was considered for each layer. The parameters of the fabricated design (Fig. 5A) and of the best design are shown with stars and circles, respectively. The squares represents parameter combinations that correspond to a monostable design.

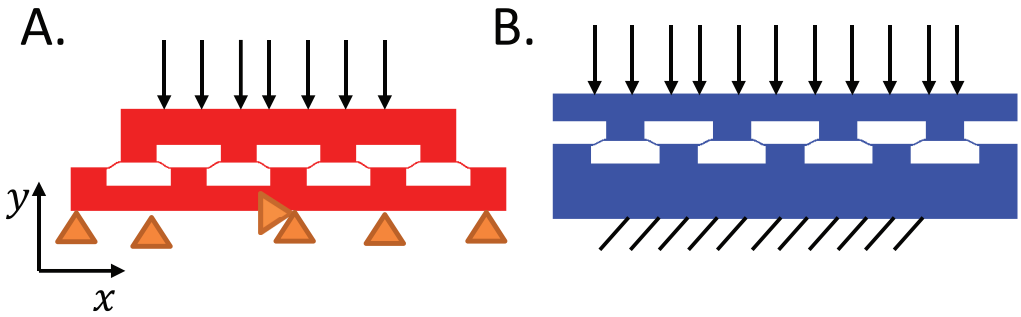

FIG. 4.7. FEA model of single layer. A. Boundary conditions for the top 3 layers. B. Boundary condition for the bottom layer.

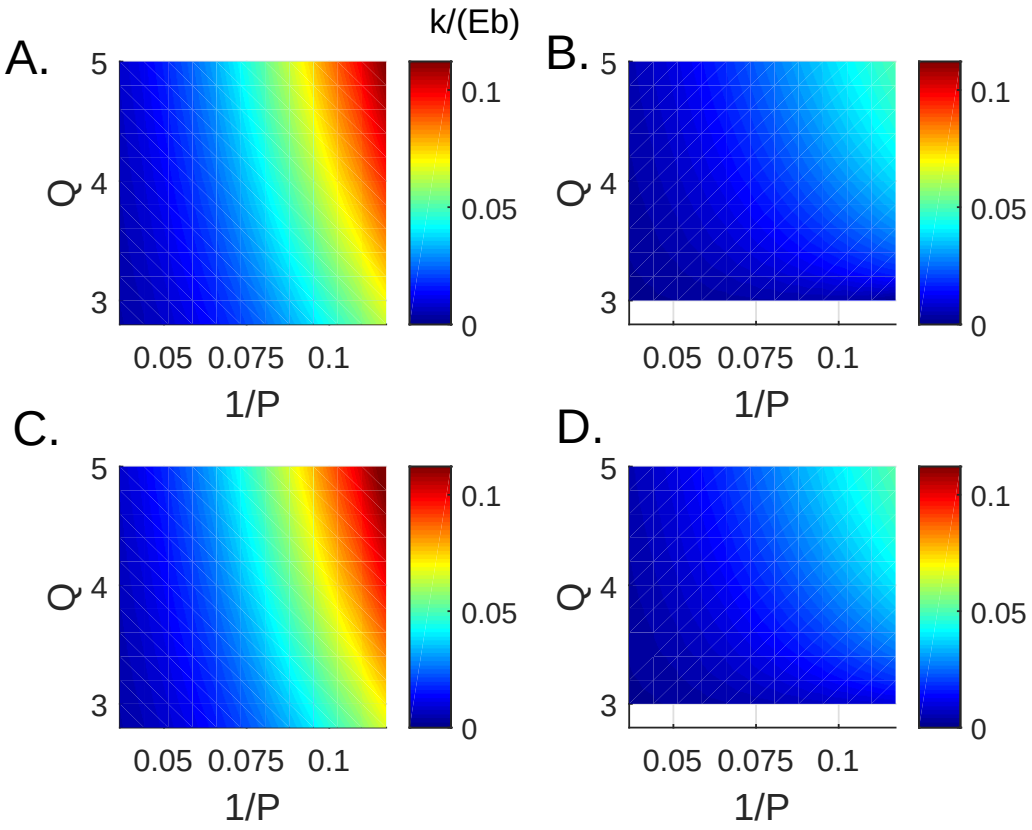

FIG. 4.8. Value of the normalized stiffness ($k/(Eb)$) in the undeformed configuration (k_0 in A and C) and deformed configurations (k_1 in B and D) for a single layer as function of P and Q. The normalized stiffness is defined in Eq. 4.8.

To find a set of parameters such that the stiffnesses of each of the stable configurations are significantly different, we chose the design that maximizes the following objective function:

$$f(Q_1, Q_2, Q_3, Q_4, P_1, P_2, P_3, P_4) = \min_{i_1 i_2 i_3 i_4 \neq j_1 j_2 j_3 j_4} \frac{|k_{eff,i_1 i_2 i_3 i_4} - k_{eff,j_1 j_2 j_3 j_4}|}{k_{eff,0000}} \tag{4.9}$$

where $i_1 i_2 i_3 i_4$ and $j_1 j_2 j_3 j_4$ corresponds to different stable configurations; k_{eff}, is the real part of the dynamic stiffness computed using Eq. 4.7. As seen in Fig. 4.10B, the effective stiffness of the nine stable configurations for the best design obtained at room temperature using Eq. 4.7 vary more significantly than for the initial design. To confirm that this architected material exhibits significant deformation-induced tunability of its stiffness, the stiffness was directly calculated using finite element simulations of the 4-layer architected

material. For these simulations, the material was loaded at room temperature in the cases of Configurations 0001, 0011, 0111 and 1111. In order to compute the effective stiffness in other configurations, the architected material was first loaded at a higher temperature until the corresponding layers snap, before changing the temperature to room temperature. For all nine configurations, the effective dynamic stiffness was computed by applying a harmonic velocity of small amplitude at room temperature.

To illustrate the simulation process, the following discussion takes a bi-layer model as an example. For a bi-layer bimaterial architected material, there are 4 different stable configurations (00, 01, 10 and 11). Three steps are used in the simulations: compression loading, relaxation, and periodic loading. In the compression loading step, the loading cell is initially utilized to compress the structure with a loading velocity of 10mm/min; the loading cell is then held for 1000 seconds, before unloading the loading cell. The deformed structure is allowed to relax freely in the relaxation step for 6000 seconds. In the last periodic loading step, a harmonic velocity of frequency 1Hz is directly applied at the top edge of the model for 5 cycles. The effective stiffness is computed using the last cycle of the simulation.

For the undeformed stable configuration (Configuration 00), only the periodic loading step is needed. All these three steps are necessary for other three stable configurations. Since the PEGDA layer snaps before the DM layer at room temperature, all three steps are at room temperature to obtain the stiffness values for deformed configurations 01 and 11. However, in order to derive the stiffness in the last stable configuration (Configuration 10), the compression loading step has to be applied at a temperature, $T_{loading}$, above the critical temperature, T_{cr}, as shown in Fig. 4.9B. Once the material has snapped to configuration 10, the temperature is decreased to room temperature before the relaxation step, such that the effective stiffness is always calculated at room temperature. The loading temperature that were used for the nine stable configurations of the 4-layer architected material are shown in Fig. 4.9C.

A.

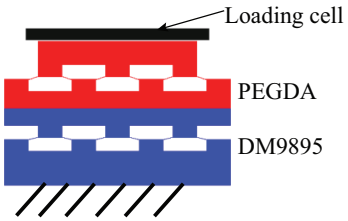

B.

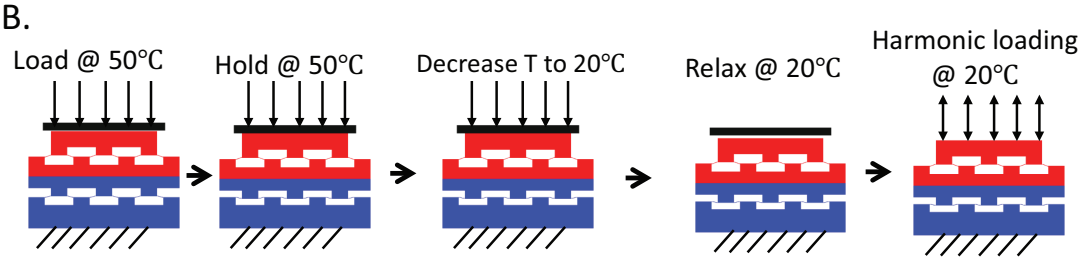

C.

Configuration	$T_{loading}$(°C)	$T_{harmonic}$(°C)
0000	–	20
0001	20	20
0011	20	20
0111	20	20
1111	20	20
0100	50	20
1100	50	20
1101	50	20
0101	26	20

FIG. 4.9. A. FEA model of one bi-layer bimaterial architected material. B. Stiffness calculation process for configuration 01 of a bi-layer bimaterial architected material. C. Loading temperature for 4-layer architected material (Fig. 4.10D).

While small quantitative differences with the spring model are observed, the stiffness obtained with these direct FEA simulations also show that the nine stable configurations have significantly different effective stiffnesses (Fig. 4.5B); for example, Configuration 1111 is 66% softer than Configuration 0000. The two configurations that have the most similar stiffness are Configurations 0111 and Configuration 1111; the difference in their stiffness values is 4% of the stiffness in Configuration 0000.

Examination of the parameters for the best design ($Q_1 = 3$, $Q_2 = 3$, $Q_3 = 3.2$, $Q_4 = 4$, $P_1 = 13.7$, $P_2 = 15.2$, $P_3 = 17.1$, and $P_4 = 19.5$) makes it possible to get some insight

about what is required to obtain highly tunable stiffness. When the geometrical parameters of a single layer of unit cells are such that the unit cells are close to the limit between monostable and bistable behaviors ($Q_{cr} \approx 3$), the stiffness in the undeformed configuration is much higher than the stiffness in the deformed configuration, as shown in the recent work of Meaud and Che[54]. Because of the significant difference between the stiffness in the undeformed and deformed configurations of each unit cell, snapping from one configuration to another configuration cause a significant change in the effective stiffness of the architected material.

Other researchers have used temperature-induced effects to develop programmable materials with tunable stiffness. For example, Restrepo *et al.*[109,110] recently proposed periodic cellular solids with tunable stiffness by introducing controlled morphological imperfections into the unit cells and exploiting the shape memory effect. Haghanah *et al.*[?] introduced programmable architected materials that can tuned via using actuation of embedded electromagnetic locks. In contrast to our work, these materials are truly two-dimensional materials while our architected material have only tunable properties in the vertical (Y direction). Compared to this previous work, the use of multistable architected materials makes it possible to use a simple model based on a 1D chain of elastic springs that predicts with great accuracy the stiffness of an architected materials with N layers. This spring model makes it easier to design materials with desired tunable stiffness properties.

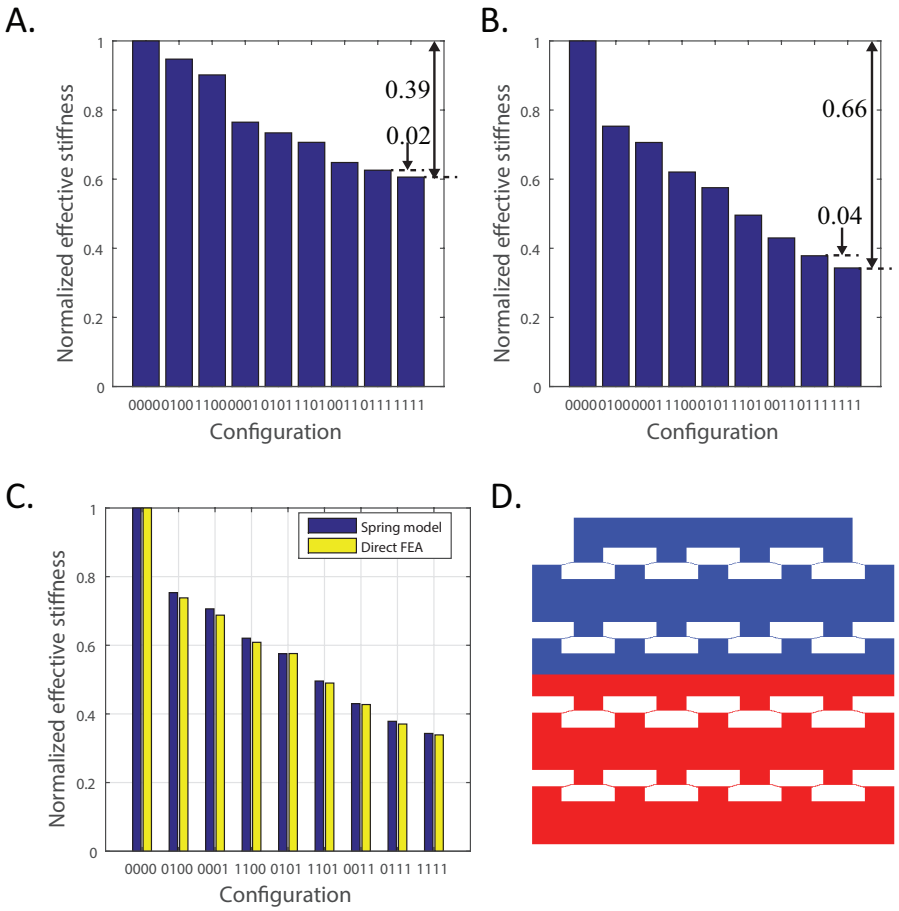

FIG. 4.10. Normalized effective stiffness of the stable configurations for 4-layer architected materials. A. and B. Stiffness values obtained with the spring model for the design of Fig. 4.5 (A) and the best design (B). C. Comparison of the stiffness values obtained with the spring model and the direct finite element simulations for the best design. D. Best design.

4.5 Summary

These numerical and experimental results demonstrate that the snapping sequence of multi-material thermoviscoelastic architected materials can be tuned by varying temperature. In contrast to architected materials that consist of a single material discussed in Chapter 3, temperature can be used as a control parameter to tune the behavior of these smart materials after fabrication. This novel physical behavior is made possible by the use of thermoviscoelastic materials whose moduli cross-over close to room temperature. The temperature-dependent switching of the snapping sequence of bilayer bimaterial architected material was

systematically investigated using finite element simulations and experiments with samples fabricated using an inverse molding process. The influence of the geometrical parameters on the critical temperature at which the snapping sequence switches from one sequence to another sequence was analyzed. These reversible configurational changes in these architected materials can be exploited to develop materials that are reconfigurable based on the desired functionality. Exploiting the temperature-dependent snapping sequence in bimaterial architected materials that consist of a large number of unit cells makes it possible to obtain a large number of distinct stable configurations only by applying a compressive load at different temperatures. With a proper choice of design parameters, each of these distinct stable configurations can have a unique value in its effective properties; the result demonstrated that these materials can be utilized for example as programmable soft material with tunable stiffness.

Chapter 5

Time-dependent snapping of thermoviscoelastic architected materials with snap-through instabilities

5.1 Introduction

Temperature was utilized in Chapter 4 to tune the snapping response of thermoviscoelastic architected materials with snap-through instabilities because of the temperature-dependent property of polymers. Besides having temperature-dependent properties, the polymers also have time-dependent mechanical properties, as described in Chapter 1 Section 1.2.3.

In this chapter, the time-dependent snapping response of single layer architected materials with thermoviscoelastic material was studied. For unit cells that can snap back from a deformed configuration to the undeformed configuration, the snap-back is instantaneous if the system is elastic, which means the system is monostable; however, for unit cells with viscoelastic material, due to the relaxation of viscoelastic materials, the snap-back is not instantaneous and can be delayed by a duration that depends on the geometrical parameters of the system and on temperature. This time and temperature dependent mechanics could

find interesting applications in the fields of shape morphing, energy absorption and actuators with self-recovery capabilities. The conditions for observing time-dependent snapping within a single layer was investigated in this chapter. Moreover, the effects of temperature and geometric design parameters on the time it takes for the system to snap back was also studied using finite element simulations. This time-depend snapping was further extended to a bimaterial bilayer architected materials.

5.2 Influence of viscoelasticity on the bistability of architected materials

5.2.1 FEA model

A FEA model was built to analyze the nonlinear mechanics of single layer architected materials with snap-through instabilities. As shown in Fig. 5.1A, there are three parts in the FEA model, *i.e.*, the top loading cell, a single layer architected material, and the bottom fixture. 4-node bilinear quadrilateral plane-stress elements with reduced integration (CPS4R in Abaqus) were used. Self-contact normal interactions were defined for the whole model. The boundary conditions for the FEA models are as follows: the node at the middle of the bottom edge of the architected material model is fixed in the x direction, the bottom fixture is fixed, and the x direction displacement of the loading cell is constrained. In order to study the influence of viscoelasticity on the bistability of architected material with snap-through instabilities, the architected material models were built with both elastic and viscoelastic constitutive models. The material parameters for DM are the same as in Chapter 4.

In the FEA simulations, there are three steps for the loading cell (shown in Fig. 5.1B): (1) the loading step (the loading cell moves in -y direction with constant velocity to cause the architected material model to collapse), (2) the relaxation step (the loading cell is held at a constant displacement), and (3) the unloading step (the loading cell moves in $+y$ direction

with constant velocity).

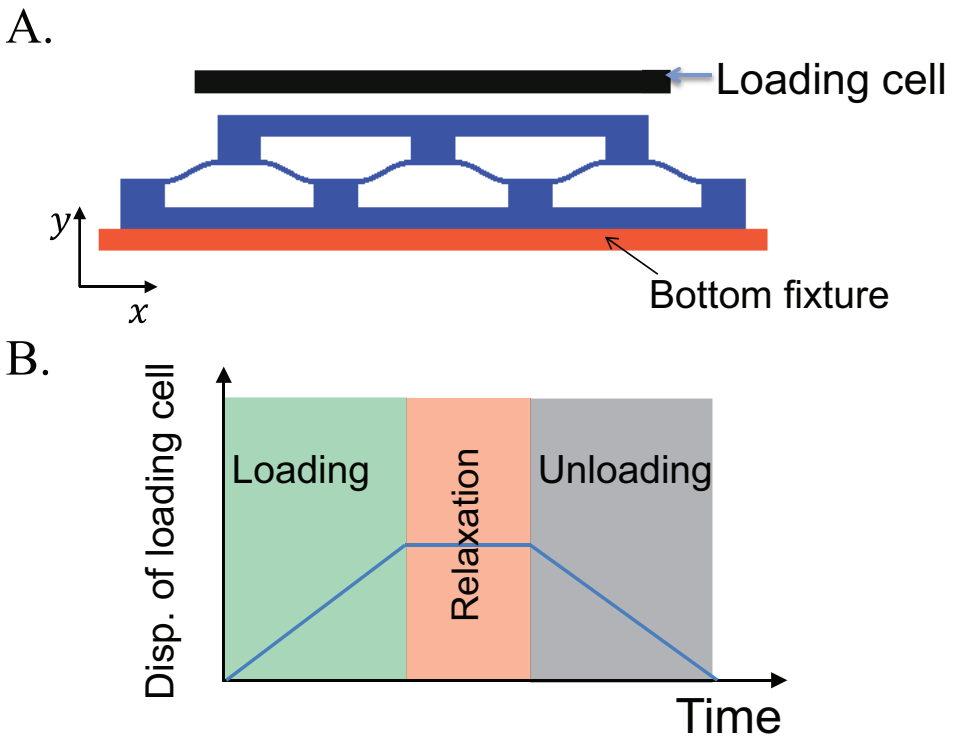

FIG. 5.1. FEA model of single layer architected material. A. Schematics of the FEA model comprised of three parts: loading cell, architected material model, bottom fixture. B. Loading history for the loading cell.

5.2.2 Bistability of architected material made of an elastic material

As described in Chapter 2 Section 2.2, the bistability of a single layer architected material with elastic constituent only depends on the geometric design parameters. For single layer architected materials made up of unit cells without mode shape imperfections, the bistability is only related to the geometric constant Q. Fig. 5.2A and Fig. 5.2B give the normalized displacement vs time curves for single layer architected materials comprised of unit cells with different Q when the architected material is loaded by a loading cell with a displacement history shown in Fig. 5.1B. With $Q = 2.7$, the single layer model snaps back to its undeformed configuration after the removal of the loading cell, which means it is monostable; while for the case with $Q = 3.0$, the single layer model remains in a deformed configuration after

the removal of the loading cell, which means it is bistable. The limit between monostable and bistable behaviors for these single layer architected materials with elastic material is $Q_{cr} \approx 2.95$, as shown in Fig. 5.2c.

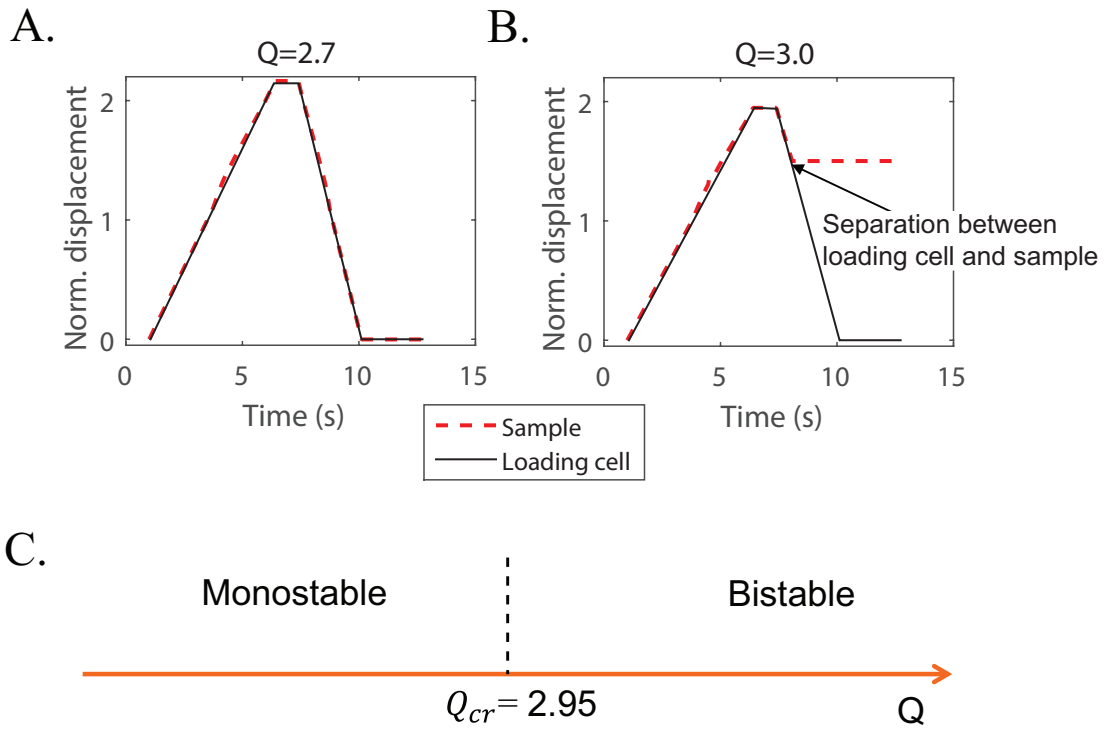

FIG. 5.2. Influence of the non-dimensional parameter $Q = h/t$ on the bistability of a single layer elastic architected material. A. Normalized displacement vs time curve for single layer architected material comprised of unit cells with $Q = 2.7$. B. Normalized displacement vs time curve for single layer architected material comprised of unit cells with $Q = 3.0$. C. Bistability limit for single layer architected material with elastic material. (The normalized displacement is defined to be the ratio of the displacement of the node on the top edge of the sample u_{top} to the initial height of curved part of the unit cell h.) The geometrical parameters of the unit cell in the architected material model have the following values: $L/h = 4.91$, $T/h = 6.16$, $H/h = 1.55$, $w/h = 1.97$, $h/t = Q$.

5.2.3 Bistability of architected material made of an viscoelastic material

Although there is a distinct bistability limit for single layer architected materials with elastic material, that distinction becomes more blurry in the case of a viscoelastic system. As a single layer architected material with elastic constituent, a single layer architected material with

viscoelastic material is monostable (the single layer sample snaps almost instantaneously) when the geometric constant Q is small, for example the model with $Q = 2.7$ shown in Fig. 5.3A. For larger geometric constant Q, for example the model with $Q = 2.95$ shown in Fig. 5.3C, the single layer sample is considered to be bistable: it remains in a deformed configuration for the duration of the simulations (5 hours). However, when the geometric constant Q has an intermediate value, for example the model with $Q = 2.83$ shown in Fig. 5.3B, the bistability of a single layer architected material with viscoelastic material falls into a third regime, that has been termed "temporary bistability' by Santer[7] or 'pseudo-bistability" by Brinkmeyer *et al.*[91]. Initially the single layer sample appears to be locked in an unstable equilibrium; however, after a long duration (about 33.7 minutes), it jumps to the stable undeformed configuration.

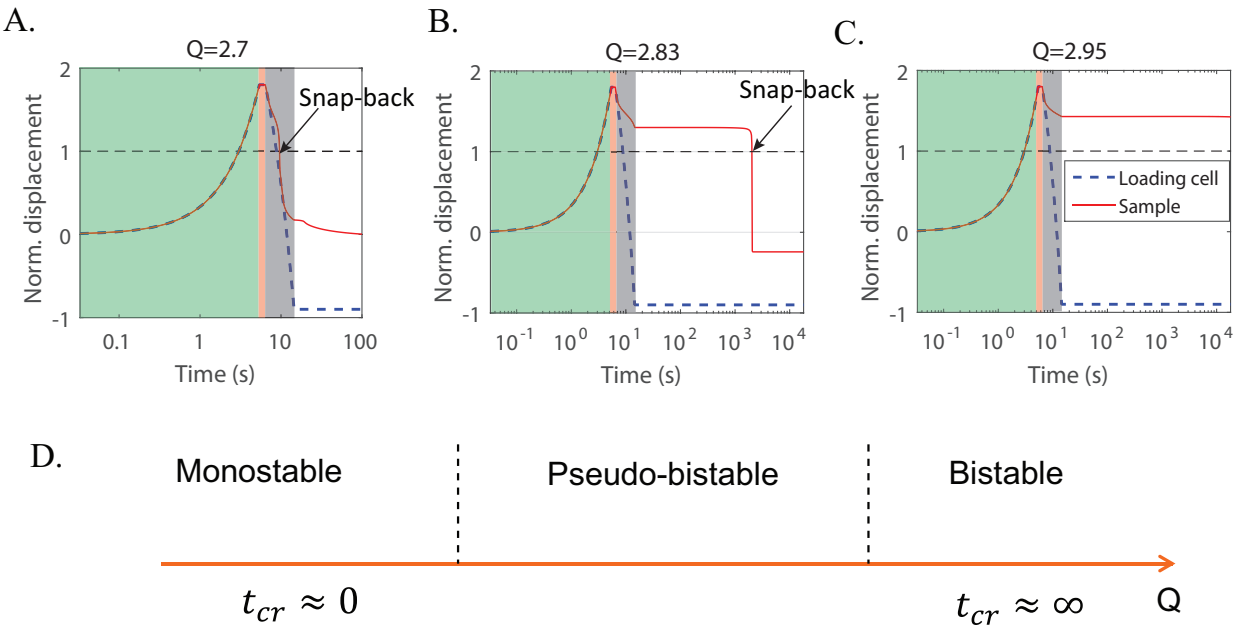

FIG. 5.3. Results of FEA simulations for single layer architected materials with viscoelastic material. A-C. Normalized displacement vs time curves for single layer architected materials comprised of unit cells with $Q = 2.7$ (A), $Q = 2.83$ (B) and $Q = 2.95$ (C). All simulations are at room temperature ($T = 20^oC$).

5.3 Critical time for architected materials with viscoelastic material

5.3.1 Definition of critical time

An objective and quantitative value, the critical time, was introduced to study the influence of geometric parameters and temperature on the time-dependent snapping. As shown in Fig. 5.4, the critical time, t_{cr}, was defined to be:

$$t_{cr} = t_2 - t_1 \tag{5.1}$$

where t_1 is the time when the normalized displacement of the loading cell equals 1 during the unloading step, and t_2 is the time when the normalized displacement of the architected material equals 1 during the recovery step.

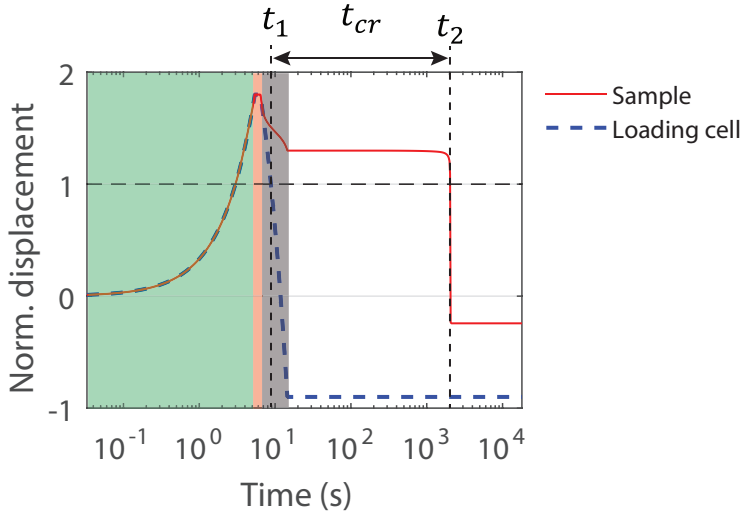

FIG. 5.4. Definition of t_{cr} for time dependent snapping of single layer architected material with viscoelastic material.)

The three bistability regimes discussed in Section 5.2.3 (shown in Fig. 5.3) can be categorized by the relative values of t_{cr},

- the single layer sample is monostable, if t_{cr} is very small (the sample was considered

to be monostable if $t_{cr} < 3$ seconds);

- the single layer sample is bistable, if $t_{cr} = \infty$ (because the simulations need to be completed within a finite duration, the criterion $t_{cr} > 5$ hours was chosen to determine whether a sample is bistable);

- the single layer sample is pseudo-bistable, if $0 < t_{cr} < \infty$ (the sample was considered to be pseudo-bistable if 3 seconds $< t_{cr} < 5$ hours).

5.3.2 Influence of geometric design and temperature

After defining the critical time t_{cr}, the influence of geometric design and temperature was studied using FEA simulations. The results shown in Fig. 5.5A demonstrates that the critical time t_{cr} is nearly temperature-independent for low Q values (for example $Q = 2.75$), which corresponds to a monostable behavior; however, for high Q values (for example $Q = 2.95$), the critical time t_{cr} varies from 5 hours to less than 10 seconds as temperature increases from 20^oC to 60^oC, which corresponds to a pseudo-bistable behavior. For even larger Q (for example $Q = 2.95$, not shown in the figure), the sample did not snap back even after 5 hours, such that it was considered to be bistable.

Fig. 5.5B shows that the critical time t_{cr} increases as the geometric constant Q increases from a timescale of a few seconds to multiple hours. For example, when $Q < 2.8$, the critical time t_{cr} remains less than 3 seconds. The single layer samples with $Q < 2.8$ can be categorized as monostable architected materials. For single layer samples with $Q > 2.95$, the critical time t_{cr} is larger than 5 hours; these single layer samples are categorized as bistable architected materials. In the third regime, where $2.8 < Q < 2.95$, the critical time Q varies dramatically from seconds to hours. These single layer samples are referred to be pseudo-bistable.

While the works of Santer[7] and Brinkmeyer *et al.*[91] demonstrate that pseudo-bistability depends on the geometric parameters of a system with snap-through instability, the influence

of temperature is analyzed for the first time here. For a given sample, varying temperature makes it possible to tune the critical time after fabrication, from a time scale of a few hours to a few seconds.

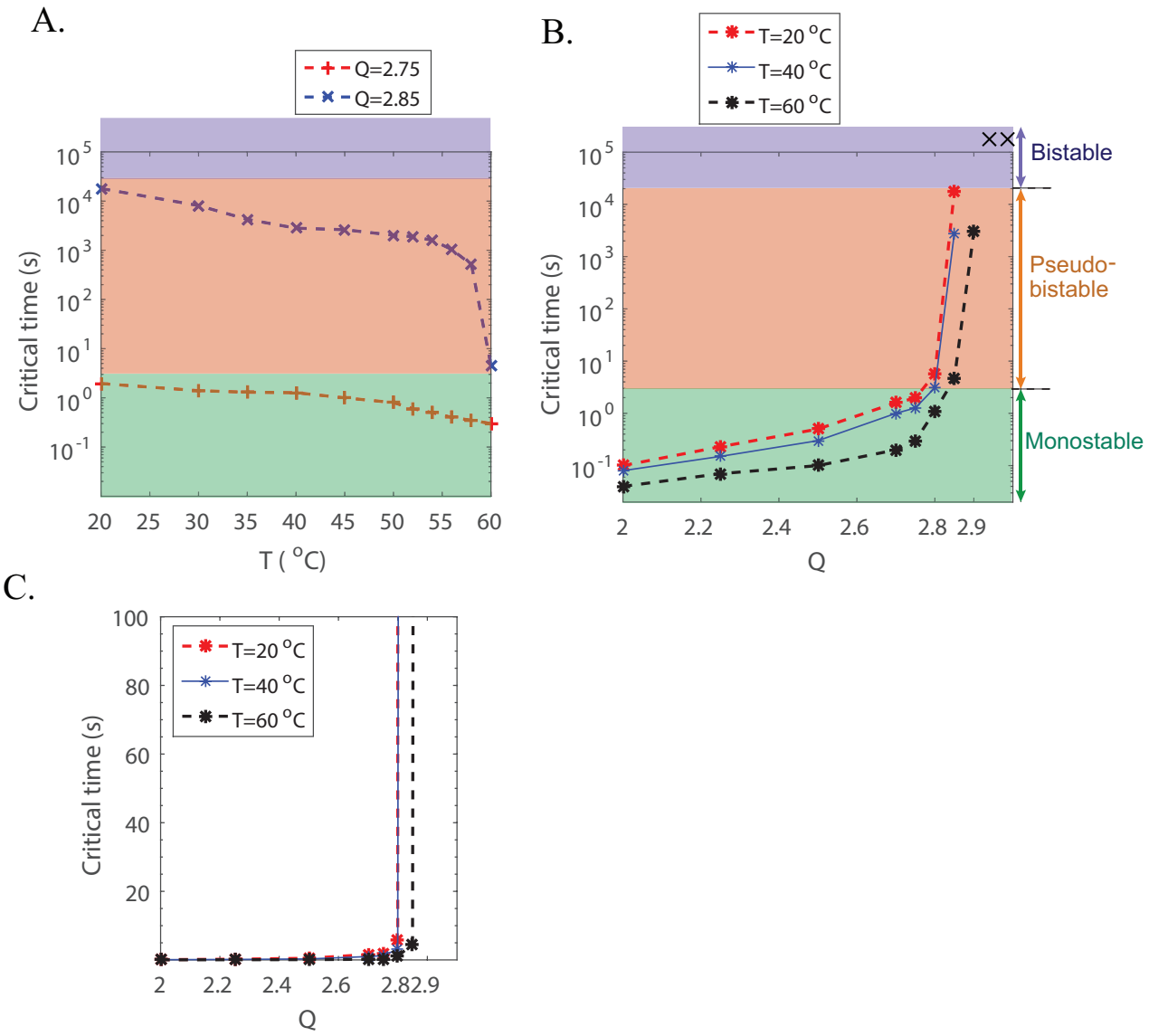

FIG. 5.5. Influence of geometric design and temperature on the critical time t_{cr} for time dependent snapping of single layer architected material with viscoelastic material (the maximum normalized displacement $\bar{d} = 1.8$), C is just the same figure as B with linear y scale. x represents the the data points that have critical time $t_{cr} > 5$ hours.

5.3.3 Experimental validation

Experiments were conducted to validate the FEA results for the time-dependent snapping of a single layer architected material . The samples were printed using the same 3D printer (Objet Connex 260) described in Chapter 3. The printing material used here was also DM9895. The experiments were conducted at different temperature and the loading velocity was 14.25 mm/min. The displacement history of the sample was extracted from the recorded video of the experiment. The maximum experiment time is 10 minutes. Several snapshots from one experiment of sample with $Q = 3.0$ at room temperature were shown in Fig. 5.6. Four points (1, 2, 3, 4) represent the sample top left, middle, right and the loading cell, respectively. The snapshots demonstrate that there is a time-dependent snapping for this sample: it took about 5 minutes for this sample to snap back to its initial configuration after removing the loading cell.

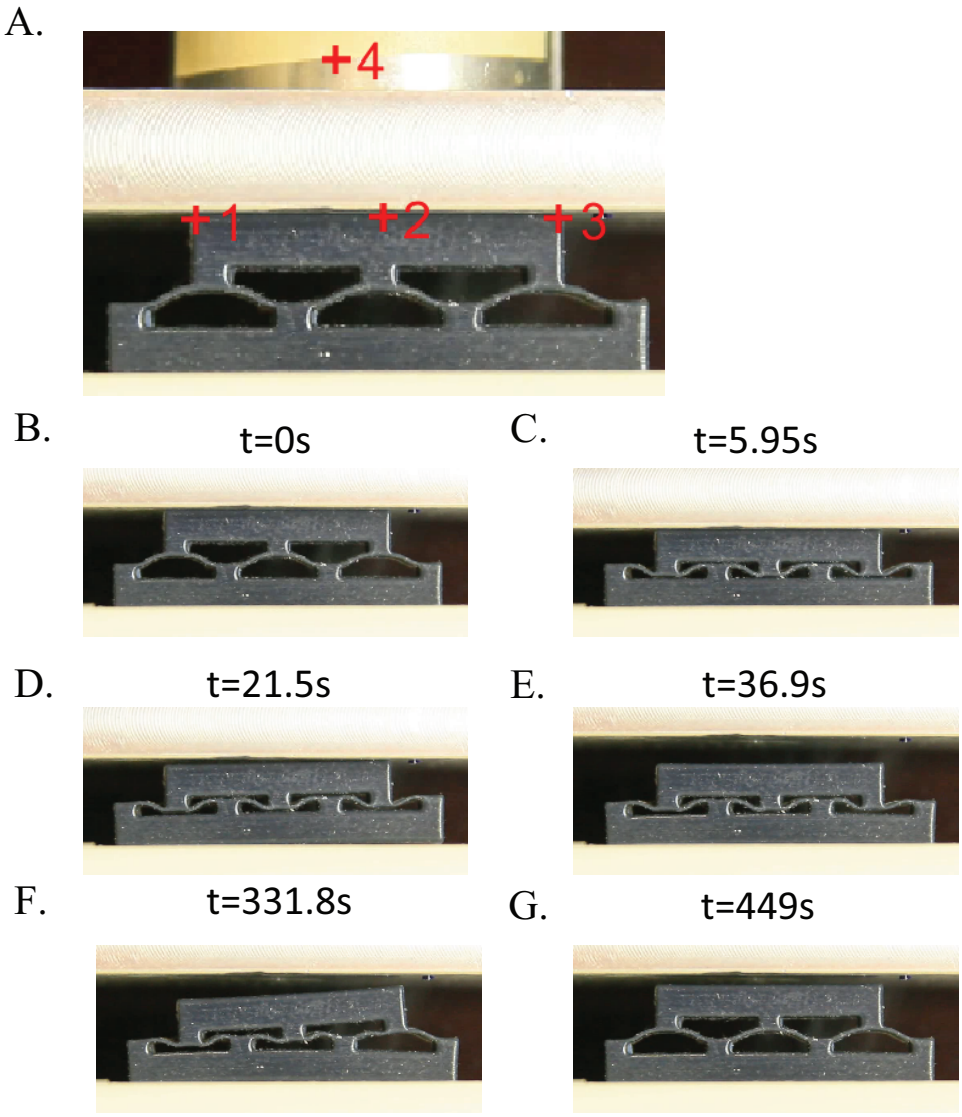

FIG. 5.6. Snapshot from the recorded experiment video of sample with $Q = 3.0$. A. Labeled points 1, 2, 3, 4 for post-processing of the video to obtain the deformation history. 1, 2, 3, 4 corresponds to the sample top left, middle, right and the loading cell. B, C, D, E, F and G are snapshots that correspond to the onset of contact between the loading cell and sample, the end of the loading step, the loading cell and sample began to separate from each other, the end of unloading, right unit cell fully snapped back and the end of the experiment, respectively.

The displacement history of different samples with different Q values was plotted in Fig. 5.7. This figure shows that, during the unloading step, the displacement of the sample initially follows that of the loading cell , then the sample loses contact with the loading cell. Note that there are discontinuities in the displacement curves of the samples for both Fig.

5.7A and B. These discontinuities are due to the fact that the loading cell and the sample tend to stick to each other at $t = 18.8$ seconds under $T = 20^oC$ such that the sample was lifted by the loading cell before suddenly dropping down.

At room temperature (20^oC), the sample with $Q = 2.7$ returns quickly to its undeformed configuration; however, the sample with $Q = 3.0$ appears to remain in the vicinity of a second equilibrium for a long duration (about 5 minutes), before snapping back. This indicates pseudo-bistable behavior. Increasing temperature T causes the sample to snap back earlier for both samples with $Q = 2.7$ and $Q = 3.0$.

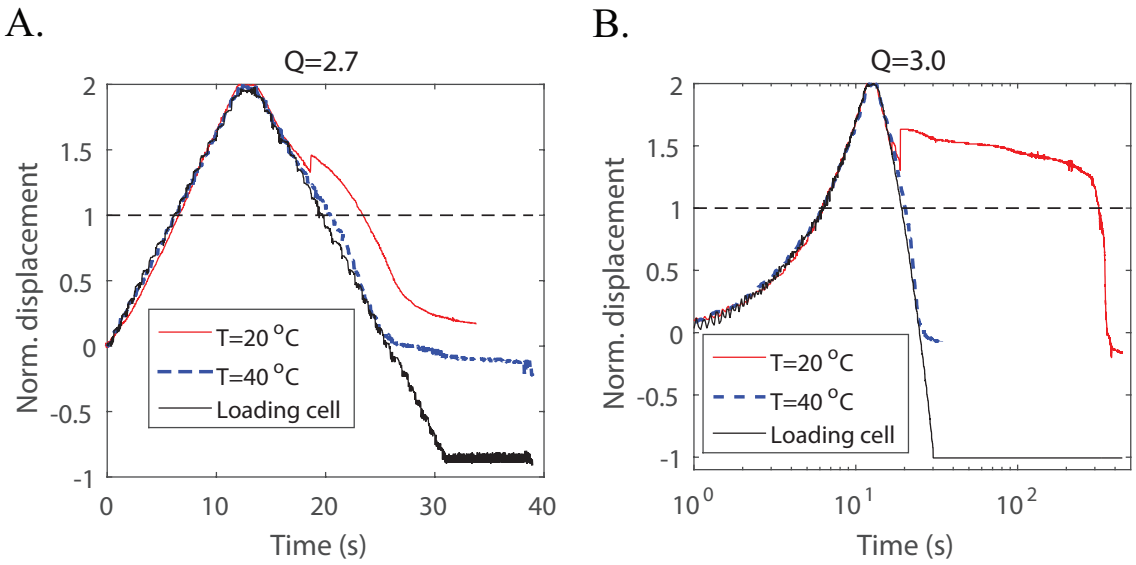

FIG. 5.7. Normalized displacement vs time from experiment for the single layer samples with different Q and temperature (only showing the data for the top middle of the samples). A. $Q = 2.7$. B. $Q = 3.0$. The maximum normalized displacement is 2.0.

Once the displacement history curves were obtained, the critical time for each sample at different temperature was calculated using Eq. 5.1. Fig. 5.8 validated previous results from FEA simulations: the critical time t_{cr} increases when the geometric parameter Q increases and decreases from minutes to seconds when the temperature increases from 20^oC to 40^oC. The results demonstrates that, for a given sample, varying temperature makes it possible to tune the critical time after fabrication.

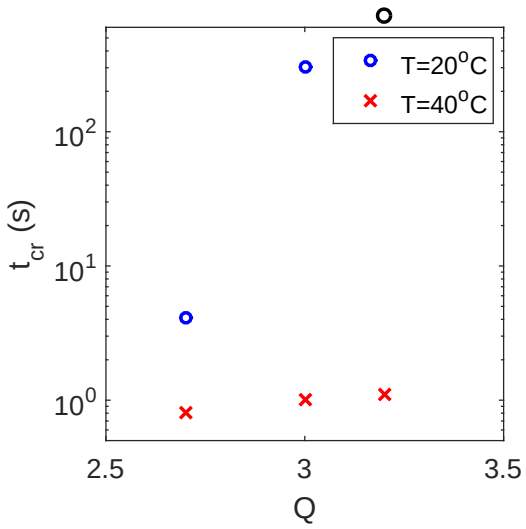

FIG. 5.8. Effects of temperature and geometric design on critical time of single layer viscoelastic architected materials. Black circle symbol indicates that the sample with $Q = 3.2$ did not snap back within 10 minutes at 20^oC.

5.3.4 Influence of imperfections on the critical time

Some additional samples were also fabricated. These samples had different set of model parameters, in particular the parameter t was considerably smaller. Because of the small dimension, the lack of accuracy of 3D printing cause the presence of shape imperfections in the samples. The geometrical parameters for these two sets of printed samples are given in Table. 5.1.

TABLE 5.1. Geometrical parameters for printed samples

Parameter	Samples in Section 5.3.3 (mm)	Samples and FEA models in Section 5.3.4 (mm)
h	0.712	1.425
t	h/Q	h/Q
l	7	7

In experiments, these imperfections are inevitable and cannot be ignored. Chapter 2 discussed that higher mode imperfections could affect the bistability of a unit cell. FEA simulations show that higher mode imperfections dramatically decrease the critical time

t_{cr} of single layer architected materials with viscoelastic materials. For example, Fig. 5.9 demonstrates that the critical time for a single layer architected material with $Q = 2.85$ decreases to less than 1 second when a 10% second mode imperfection is introduced.

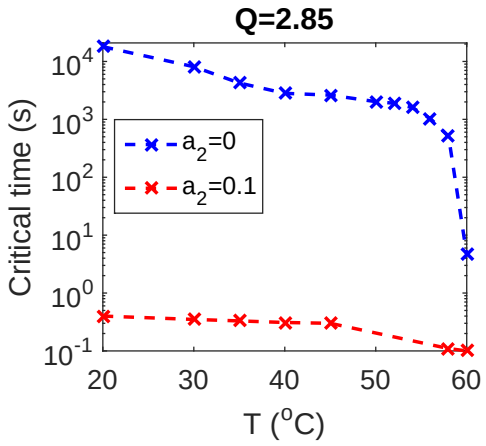

FIG. 5.9. Influence of higher mode imperfection on the critical time t_{cr} for time dependent snapping of single layer architected material with viscoelastic material (the maximum normalized displacement $\bar{d} = 1.8$, $Q = 2.85$).

Fig. 5.10 shows that the top left (Point 1), top middle (point 2) and top right (point 3) of the samples (see Fig. 5.7) do have the same displacement, which implies that there is some rotation of part of the sample (see Fig. 5.6F). This indicates that the printed sample has a non-symmetric mode (2^{nd} mode) shape imperfection. The value for the critical time, evaluated using the displacement of point 2 at the middle of the sample (see Fig. 5.6A) is $t_{cr} = 1.3$ seconds.

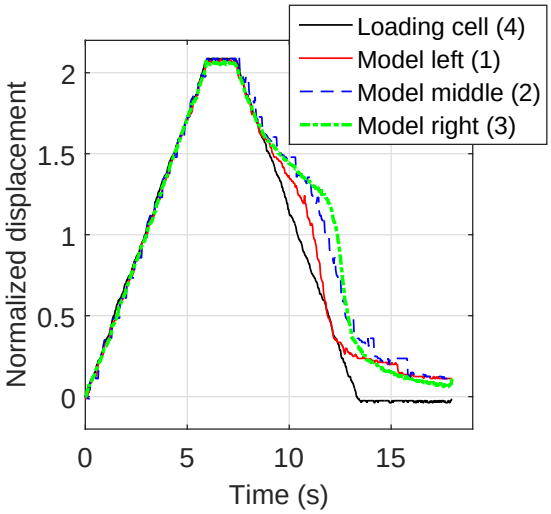

FIG. 5.10. Normalized displacement vs time from experiment for the single layer sample with $Q = 2.7$. The maximum normalized displacement is 2.1.

The corresponding FEA model was built with perfect unit cells and unit cells with higher mode imperfections (defined as Eq. 2.29). The results of normalized displacement vs. time curves from FEA simulations are shown in Fig. 5.11. The critical time for this single layer sample without imperfections is $t_{cr} = 56$ seconds, which is much larger than the experimental data. Due to a non-symmetric imperfection observed in the experiments, a 2^{nd} mode imperfection was added for the FEA model with imperfections. After adding higher mode imperfections, the critical time from FEA simulation is $t_{cr} = 1.21$ seconds. The comparison of normalized displacement vs time between FEA simulation with higher mode imperfections and experiment are shown in Fig. 5.12, which gives good agreement between FEA simulation and experiment. The results of Fig. 5.9 demonstrate that choosing parameter values such that good control of the geometry is achievable is critical in order to observe pseudo-bistable behavior with a high critical time value.

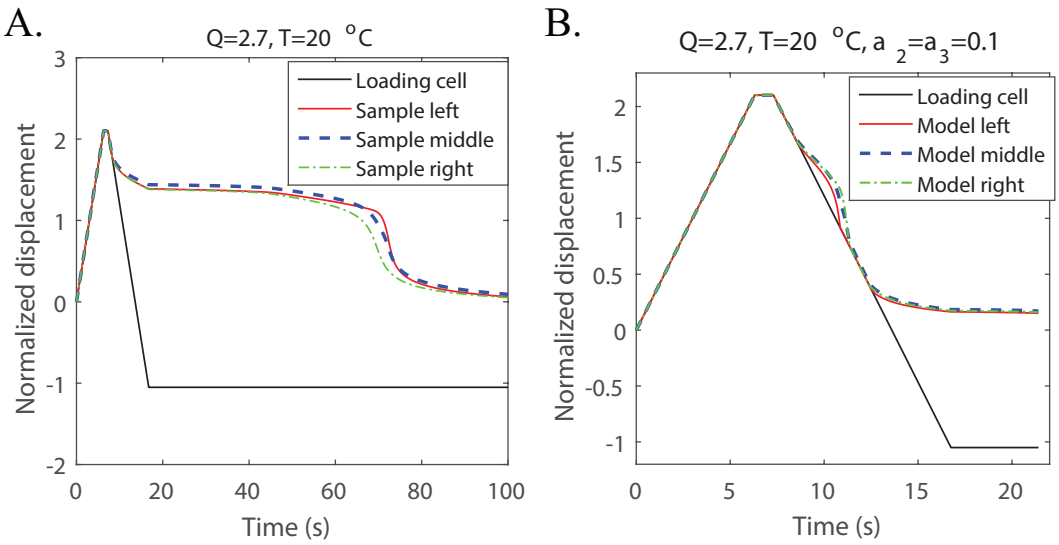

FIG. 5.11. Normalized displacement vs time from FEA simulations for the single layer sample with $Q = 2.7$. A. No imperfection included in the curved shape of the unit cells. B. Higher mode imperfections introduced ($a_2 = a_3 = 0.1$).

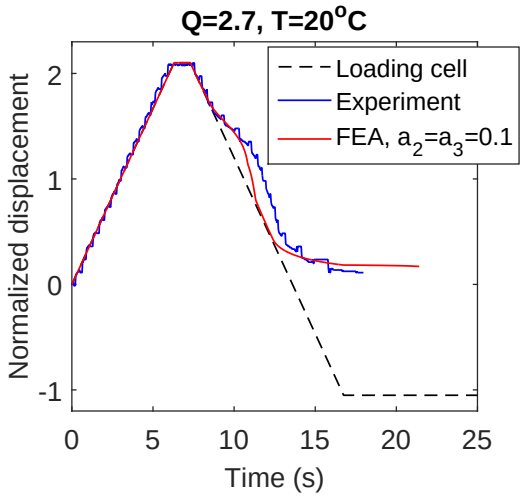

FIG. 5.12. Comparison of normalized displacement vs time between FEA simulations with mode imperfection ($a_2 = a_3 = 0.1$) and experiment for the single layer sample with $Q = 2.7$. The displacement of point 2 (see Fig. 5.6A) was used.

5.4 Extension to multimaterial multi-layer architected materials

The time-dependent snapping observed in these single layer architected materials with viscoelastic material gives the insight to look at more complex architected material, like the bimaterial system described in Chapter 4. The local stiffness of a layer made of a viscoelastic material decreases over time when the structure is held at constant strain. This makes it possible to observe interesting time-dependent snapping of a bimaterial bi-layer architected material. When it is first loaded, only one of the two layers is in a deformed configuration. Consider the experiment shown in Fig. 5.13. In this experiment, the bimaterial bilayer sample (top layer with PEGDA, bottom layer with DM) was first compressed at constant velocity at 35^oC until the top layer collapsed. Then the loading cell was held such that the total strain of this sample was constant. Interestingly, it was observed that a configurational change occurred, *i.e.*, the deformed top layer snapped back to the undeformed configuration, while the undeformed bottom layer snapped into a deformed configuration.

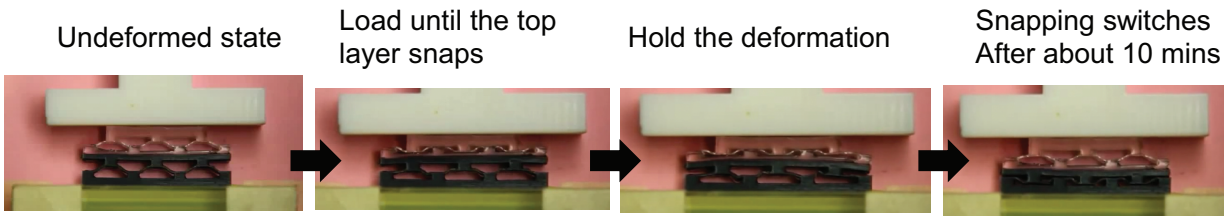

FIG. 5.13. Experiment result of time dependent switching for a bilayer bimaterial architected material with $30mm/min$ loading velocity at 35^oC

5.5 Summary

In this chapter, the time-dependent snapping of single layer architected materials with a viscoelastic constitutive model was studied. Unlike single layer architected materials with elastic material whose bistability only depends on geometric parameters, temperature also influences the bistability of single layer architected materials with viscoelastic material. Due

to viscoelasticity effects, there is no distinct limit between bistable and monostable behaviors. A third regime, called pseudo-bistable behavior, was observed for single layer architected materials with viscoelastic material. Depending on the critical time, these three regimes (monostable, bistable, and pseudo-bistable) were analyzed. The influence of geometric design and temperature on the critical time was investigated using FEA simulations. The results demonstrated that for a single layer model with pseudo-bistability, the critical time varied from seconds to hours as temperature is increased. This time-dependent snapping behavior was also observed in experiments with 3D printed samples.

Moreover, multilayer architected materials with pseudo-bistability can demonstrate interesting snapping response. For example, after being deformed, a multilayer architected material could recover layer by layer if the layers are designed to have different critical time values. The capacity to tune the time dependent snapping could be utilized to develop novel reconfigurable materials with programmable properties, and could find interesting applications for shape morphing or energy absorption with self-recovery capabilities.

Chapter 6

Conclusion

6.1 Summary of the completed research

This thesis studied one kind of architected materials comprised of unit cells with snap-through instabilities. In order to study and analyze the nonlinear mechanics of this type of architected materials, theoretical models for a single unit cell with both elastic and viscoelastic constitutive models were developed and validated using FEA simulations.The developed theoretical models are much more computationally efficient than FEA models to study the nonlinear mechanics of a single unit cell with both an elastic and viscoelastic material. For a single unit cell with elastic material, the force vs deformation curves and bistability were analyzed. The results showed that it is possible to tune the critical force of a single unit cell by varying the geometric design parameters and introducing mode imperfections. For single unit cells with visceolastic material, besides the choice of geometric design and mode imperfections, one can also utilize temperature and strain rate to tailor the mechanical response due to the viscoelasticity effects. The advantage is that these control parameters can be implemented after the fabrication of the samples.

Based on the theoretical model of a single unit cell with elastic material, a theoretical model of multi-layer architected material with elastic material was developed and validated

using FEA simulations. The deformation sequence for multi-layer architected materials was analyzed using the theoretical model, FEA simulations and experiments with 3D printed samples. The results demonstrated that one can obtain a deterministic deformation sequence for a multistable architected materials with sanp-through instabilities by introducing some geometric variations to the unit cells. This overcomes the limitations that the snapping sequence is undetermined if the unit cells are identical.

Although the snapping sequences can be determined by varying the geometric design parameters of the unit cells, the sanpping sequence of architected material with a single material is fixed and cannot be changed after being fabricated. In order to have tunable snapping sequence and enhanced reconfigurability, this study continued to develop bimaterial architected materials with snap-through instabilities by a facile 3D printing inverse molding process. Due to the effects of viscoelasticity, the snapping sequence of these bimaterial architected materials was controllable by using different temperatures. Because the snapping sequence is tunable, this kind of architected materials could have much more stable configurations. This thesis demonstrated one potential application of reconfigurable architected material with tunable mechanical stiffnesses.

In addition to having temperature-dependent properties, viscoelastic architected materials with snap-through instabilities also have a time-dependent response. The time dependent snapping of these materials was analyzed, primarily using finite element simulations. Unlike single layer architected materials with elastic material, there were three regimes for single layer architected materials with viscoelastic material: monostable, bistable and pseudo-bistable categorized by the relative critical time t_{cr}. The effects of temperature and geometric design on the critical time were analyzed. The results demonstrated that the critical time varied from seconds to hours for architected materials with pseudo-bistability. The pseudo-bistable behavior was validated experimentally.

Analyzing the fundamental mechanics of architected materials with snap-through instabilities in this thesis gave a better understanding of how geometric design parameters and

temperature could be utilized to design and obtain reconfigurable architected materials with switchable snapping sequences. The work of this study can give other researchers some insights to develop and study similar architected materials with snap-through instabilities.

6.2 Opportunities for future work

The theoretical model of a unit cell with viscoelastic material could be extended to a multilayer model as was done in Chapter 3 for the elastic case. This theoretical model would be useful to analyze the mechanical response of multilayer viscoelastic architected materials with snap-through instabilities. Moreover, the theoretical model of a viscoelastic unit cell could also be extended to study the time-dependent snapping of a pseudo-bistable unit cell.

The time-dependent snapping of architected materials with a viscoelastic material can be explored to study what type of complicated time-dependent snapping response could be obtained by assembling multiple layers made of different materials. Multilayer viscoelastic architected materials makes it possible to exhibit interesting snap-back behavior layer by layer with a tunable critical time. These architected materials could have potential applications of actuators with self-recovery capabilities.

Furthermore, some limitations of this work are that it focuses on the 1D architected materials with snap-through instabilities. 2D and 3D designs of architected materials with snap-through instabilities have been recently proposed[6]. Extension of the analysis of viscoelastic effects for these designs could expand the range of applications for the concepts that were investigated in this thesis.

Appendix

Appendix A: Material model parameters

Two materials used in this dissertation are PEGDA and DM9895. PEGDA is modeled as an elastic material with a constant Young's modulus of 25MPa. DM9895 is modeled as a thermoviscoelastic material, with a 27 term Prony series. The material parameters for DM9895 are the values of E_0, E_i, τ_i^0, C_1, C_2 and T_M (see Eqs. 2.22-2.24). These parameters were found in a previous paper by fitting the model to DMA measurements[83]. For completeness, the parameters are listed in the Tables 1 and 2:

TABLE 1. Other parameters in the viscoelastic model

Parameter	Value
T_g	38 (^{o}C)
T_M	-3 (^{o}C)
C_1	17.44
C_2	42.1
E_0	3.3 MPa

TABLE 2. Parameters for the viscoelastic branches in the viscoelastic model

Branch i	E_i (Pa)	τ_i^0 (s)
1	3E+08	0.0001
2	2.75E+08	0.000657
3	2.96E+08	0.003872
4	3.05E+08	0.02
5	3.5E+08	0.1
6	3.78E+08	0.576863
7	2.92E+08	3.401616
8	2.15E+08	20
9	1.47E+08	96.82391
10	2.15E+08	362.9461
11	63127650	1000
12	62092100	2671.527
13	52099306	7912.87
14	42374719	23498.79
15	35205449	71461.38
16	27897552	228551.6
17	20760769	726401
18	15532429	2277776
19	11281878	7091525
20	8305791	21997171
21	5959708	68236585
22	4351312	2.08E+08
23	3329757	6.41E+08
24	2644468	2.07E+09
25	2196711	7.07E+09
26	1578065	2.4E+10
27	107012.2	1E+11

Appendix B: Modal amplitude calculation from FEA

Using integration by part, the integration of the product of one mode shape and of the 2^{nd} derivative of another mode shape yields the following value,

$$\begin{aligned}\int_0^l W_i(x)W_j^{(\prime\prime)}(x)dx &= -\int_0^l W_i^{\prime}W_j^{\prime}dx \\ &= 0 \quad \text{if } i \neq j \\ &= -\frac{N_i^2}{2l} \quad \text{if } i = j\end{aligned} \tag{6.1}$$

Let the beam shape from FEA simulation as $w(x,t)$,

$$w(x,t) = \sum_{i=0}^{N_m} A_i(t)W_i(x) \tag{6.2}$$

Thus,

$$\begin{aligned}&\int_0^l w(x,t)W_j^{\prime\prime}dx \\ &= \sum_{i=0}^{N_m} A_i(t)\int_0^l W_i(x)W_j^{\prime\prime}(x)dx \\ &= -\frac{N_i^2}{2l}A_i(t) \quad \text{if } i = j\end{aligned} \tag{6.3}$$

such that the mode amplitudes for FEA simulations are obtained using Eq. 6.4.

$$A_n(t) = -\frac{2l}{N_n^2}\int_0^l w(x,t)W_n^{\prime\prime}dx \quad \text{for } n = 1,3,\ldots,N_m \tag{6.4}$$

References

[1] David Restrepo, Nilesh D Mankame, and Pablo D Zavattieri. Phase transforming cellular materials. *Extreme Mechanics Letters*, 4:52–60, 2015.

[2] Babak Haghpanah, Ladan Salari-Sharif, Peyman Pourrajab, Jonathan Hopkins, and Lorenzo Valdevit. Multistable shape-reconfigurable architected materials. *Advanced Materials*, 28(36):7915–7920, 2016.

[3] Dixon M Correa, Carolyn C Seepersad, and Michael R Haberman. Mechanical design of negative stiffness honeycomb materials. *Integrating Materials and Manufacturing Innovation*, 4(1):8, 2015.

[4] Sicong Shan, Sung H Kang, Jordan R Raney, Pai Wang, Lichen Fang, Francisco Candido, Jennifer A Lewis, and Katia Bertoldi. Multistable architected materials for trapping elastic strain energy. *Advanced Materials*, 27(29):4296–4301, 2015.

[5] Tobias Frenzel, Claudio Findeisen, Muamer Kadic, Peter Gumbsch, and Martin Wegener. Tailored buckling microlattices as reusable light-weight shock absorbers. *Advanced Materials*, 28(28):5865–5870, 2016.

[6] Chenhui Ren, Deqing Yang, and Haoxing Qin. Mechanical performance of multidirectional buckling-based negative stiffness metamaterials: An analytical and numerical study, 2018.

[7] M. Santer. Self-actuated snap back of viscoelastic pulsing structures. *International Journal of Solids and Structures*, 47(24):3263 – 3271, 2010.

[8] A. Brinkmeyer, A. Pirrera, M. Santer, and P.M. Weaver. Pseudo-bistable pre-stressed morphing composite panels. *International Journal of Solids and Structures*, 50(7):1033 – 1043, 2013.

[9] Tobias A Schaedler and William B Carter. Architected cellular materials. *Annual Review of Materials Research*, 46:187–210, 2016.

[10] Jae-Hwang Lee, Jonathan P Singer, and Edwin L Thomas. Micro-/nanostructured mechanical metamaterials. *Advanced materials*, 24(36):4782–4810, 2012.

[11] N. A. Fleck, V. S. Deshpande, and M. F. Ashby. Micro-architectured materials: past, present and future. *Proceedings of the Royal Society of London A: Mathematical, Physical and Engineering Sciences*, 466(2121):2495–2516, 2010.

[12] CM Spadaccini. Mechanical metamaterials: Design, fabrication, and performance. *Winter*, 45(4):28–36, 2015.

[13] Hao Peng and P Frank Pai. Acoustic metamaterial plates for elastic wave absorption and structural vibration suppression. *International Journal of Mechanical Sciences*, 89:350–361, 2014.

[14] HH Huang and CT Sun. Wave attenuation mechanism in an acoustic metamaterial with negative effective mass density. *New Journal of Physics*, 11(1):013003, 2009.

[15] P Frank Pai. Metamaterial-based broadband elastic wave absorber. *Journal of Intelligent Material Systems and Structures*, 2010.

[16] Christopher Sugino, Stephen Leadenham, Massimo Ruzzene, and Alper Erturk. On the mechanism of bandgap formation in locally resonant finite elastic metamaterials. *Journal of Applied Physics*, 120(13):134501, 2016.

[17] XN Liu, GK Hu, GL Huang, and CT Sun. An elastic metamaterial with simultaneously negative mass density and bulk modulus. *Applied physics letters*, 98(25):251907, 2011.

[18] Timothy Klatt and Michael R Haberman. A nonlinear negative stiffness metamaterial unit cell and small-on-large multiscale material model. *Journal of Applied Physics*, 114(3):033503, 2013.

[19] Nicholas Fang, Dongjuan Xi, Jianyi Xu, Muralidhar Ambati, Werayut Srituravanich, Cheng Sun, and Xiang Zhang. Ultrasonic metamaterials with negative modulus. *Nature materials*, 5(6):452–456, 2006.

[20] Yiqun Ding, Zhengyou Liu, Chunyin Qiu, and Jing Shi. Metamaterial with simultaneously negative bulk modulus and mass density. *Physical review letters*, 99(9):093904, 2007.

[21] Roderic Lakes. Foam structures with a negative poisson's ratio. *Science*, 235(4792):1038–1040, 1987.

[22] Sahab Babaee, Jongmin Shim, James C Weaver, Elizabeth R Chen, Nikita Patel, and Katia Bertoldi. 3d soft metamaterials with negative poisson's ratio. *Advanced Materials*, 25(36):5044–5049, 2013.

[23] Chuanwei Huang and Lang Chen. Negative poisson's ratio in modern functional materials. *Advanced Materials*, 28(37):8079–8096, 2016.

[24] L Ai and X-L Gao. Metamaterials with negative poissonŠs ratio and non-positive thermal expansion. *Composite Structures*, 162:70–84, 2017.

[25] L Ai and X-L Gao. Three-dimensional metamaterials with a negative poisson's ratio and a non-positive coefficient of thermal expansion. *International Journal of Mechanical Sciences*, 135:101–113, 2018.

[26] Jae-Hwang Lee, Lifeng Wang, Steven Kooi, Mary C Boyce, and Edwin L Thomas. Enhanced energy dissipation in periodic epoxy nanoframes. *Nano letters*, 10(7):2592–2597, 2010.

[27] Lucas R Meza, Satyajit Das, and Julia R Greer. Strong, lightweight, and recoverable three-dimensional ceramic nanolattices. *Science*, 345(6202):1322–1326, 2014.

[28] Bastiaan Florijn, Corentin Coulais, and Martin van Hecke. Programmable mechanical metamaterials. *Physical review letters*, 113(17):175503, 2014.

[29] Ladan Salari-Sharif, Tobias A Schaedler, and Lorenzo Valdevit. Energy dissipation mechanisms in hollow metallic microlattices. *Journal of Materials Research*, 29(16):1755–1770, 2014.

[30] Dixon M Correa, Timothy Klatt, Sergio Cortes, Michael Haberman, Desiderio Kovar, and Carolyn Seepersad. Negative stiffness honeycombs for recoverable shock isolation. *Rapid Prototyping Journal*, 21(2):193–200, 2015.

[31] Mehrdad Mohsenizadeh, Federico Gasbarri, Michael Munther, Ali Beheshti, and Keivan Davami. Additively-manufactured lightweight metamaterials for energy absorption. *Materials & Design*, 139:521–530, 2018.

[32] Z Yang, Jun Mei, Min Yang, NH Chan, and Ping Sheng. Membrane-type acoustic metamaterial with negative dynamic mass. *Physical review letters*, 101(20):204301, 2008.

[33] HH Huang, CT Sun, and GL Huang. On the negative effective mass density in acoustic metamaterials. *International Journal of Engineering Science*, 47(4):610–617, 2009.

[34] Nan Hu and Rigoberto Burgueño. Buckling-induced smart applications: recent advances and trends. *Smart Materials and Structures*, 24(6):063001, 2015.

[35] Lorna J. Gibson and Michael F. Ashby. *Cellular Solids: Structure and Properties*. Cambridge Solid State Science Series. Cambridge University Press, 2 edition, 1997.

[36] Stephen P Timoshenko and James M Gere. *Theory of elastic stability*. Courier Corporation, 2009.

[37] T. Mullin, S. Deschanel, K. Bertoldi, and M. C. Boyce. Pattern transformation triggered by deformation. *Physical Review Letters*, 99:084301, 2007.

[38] K. Bertoldi, M.C. Boyce, S. Deschanel, S.M. Prange, and T. Mullin. Mechanics of deformation-triggered pattern transformations and superelastic behavior in periodic elastomeric structures. *Journal of the Mechanics and Physics of Solids*, 56(8):2642 – 2668, 2008.

[39] Babak Haghpanah, Jim Papadopoulos, Davood Mousanezhad, Hamid Nayeb-Hashemi, and Ashkan Vaziri. Buckling of regular, chiral and hierarchical honeycombs under a general macroscopic stress state. In *Proc. R. Soc. A*, volume 470, page 20130856. The Royal Society, 2014.

[40] Sung Hoon Kang, Sicong Shan, Andrej Košmrlj, Wim L Noorduin, Samuel Shian, James C Weaver, David R Clarke, and Katia Bertoldi. Complex ordered patterns in mechanical instability induced geometrically frustrated triangular cellular structures. *Physical review letters*, 112(9):098701, 2014.

[41] Raj Kumar Pal, Massimo Ruzzene, and Julian J Rimoli. A continuum model for nonlinear lattices under large deformations. *International Journal of Solids and Structures*, 96:300–319, 2016.

[42] Julian J Rimoli and Raj Kumar Pal. Mechanical response of 3-dimensional tensegrity lattices. *Composites Part B: Engineering*, 115:30–42, 2017.

[43] Nicholas Karnessis and Gaetano Burriesci. Uniaxial and buckling mechanical response of auxetic cellular tubes. *Smart Materials and Structures*, 22(8):084008, 2013.

[44] K Bertoldi and MC Boyce. Mechanically triggered transformations of phononic band gaps in periodic elastomeric structures. *Physical Review B*, 77(5):052105, 2008.

[45] K. Bertoldi and M. C. Boyce. Wave propagation and instabilities in monolithic and periodically structured elastomeric materials undergoing large deformations. *Phys. Rev. B*, 78:184107, Nov 2008.

[46] Bertoldi Katia, Reis Pedro M., Willshaw Stephen, and Mullin Tom. Negative poisson's ratio behavior induced by an elastic instability. *Advanced Materials*, 22(3):361–366, 2010.

[47] Liu Jia, Gu Tianyu, Shan Sicong, Kang Sung H., Weaver James C., and Bertoldi Katia. Harnessing buckling to design architected materials that exhibit effective negative swelling. *Advanced Materials*, 28(31):6619–6624, 2016.

[48] Raj Kumar Pal, Massimo Ruzzene, and Julian J. Rimoli. Tunable wave propagation by varying prestrain in tensegrity-based periodic media. *Extreme Mechanics Letters*, 22:149 – 156, 2018.

[49] Hossein Salahshoor, Raj Kumar Pal, and Julian J. Rimoli. Material symmetry phase transitions in three-dimensional tensegrity metamaterials. *Journal of the Mechanics and Physics of Solids*, 119:382 – 399, 2018.

[50] Pai Wang, Filippo Casadei, Sicong Shan, James C Weaver, and Katia Bertoldi. Harnessing buckling to design tunable locally resonant acoustic metamaterials. *Physical review letters*, 113(1):014301, 2014.

[51] Pai Wang, Jongmin Shim, and Katia Bertoldi. Effects of geometric and material nonlinearities on tunable band gaps and low-frequency directionality of phononic crystals. *Physical Review B*, 88(1):014304, 2013.

[52] Jongmin Shim, Pai Wang, and Katia Bertoldi. Harnessing instability-induced pattern

transformation to design tunable phononic crystals. *International Journal of Solids and Structures*, 58:52–61, 2015.

[53] Stephan Rudykh and Mary C Boyce. Transforming wave propagation in layered media via instability-induced interfacial wrinkling. *Physical review letters*, 112(3):034301, 2014.

[54] Julien Meaud and Kaikai Che. Tuning elastic wave propagation in multistable architected materials. *International Journal of Solids and Structures*, 2017.

[55] D Krishnan and HT Johnson. Optical properties of two-dimensional polymer photonic crystals after deformation-induced pattern transformations. *Journal of the Mechanics and Physics of Solids*, 57(9):1500–1513, 2009.

[56] Jie Li, Jongmin Shim, Justin Deng, Johannes TB Overvelde, Xuelian Zhu, Katia Bertoldi, and Shu Yang. Switching periodic membranes via pattern transformation and shape memory effect. *Soft Matter*, 8(40):10322–10328, 2012.

[57] Ji-Hyun Jang, Cheong Yang Koh, Katia Bertoldi, Mary C. Boyce, and Edwin L. Thomas. Combining pattern instability and shape-memory hysteresis for phononic switching. *Nano Lett.*, 9(5):2113–2119, May 2009.

[58] Julien Meaud. Multistable two-dimensional spring-mass lattices with tunable band gaps and wave directionality. *Journal of Sound and Vibration*, 434:44–62, 2018.

[59] Jun-Yu Ou, Eric Plum, Liudi Jiang, and Nikolay I Zheludev. Reconfigurable photonic metamaterials. *Nano letters*, 11(5):2142–2144, 2011.

[60] CR Tipton, E Han, and T Mullin. Magneto-elastic buckling of a soft cellular solid. *Soft Matter*, 8:2880, 2012.

[61] Marshall Schaeffer and Massimo Ruzzene. Dynamic reconfiguration of magneto-elastic lattices. *Comptes Rendus Mécanique*, 343(12):670–679, 2015.

[62] Dian Yang, Lihua Jin, Ramses V. Martinez, Katia Bertoldi, George M. Whitesides, and Zhigang Suo. Phase-transforming and switchable metamaterials. 2015.

[63] Yiqi Mao, Kai Yu, Michael S. Isakov, Jiangtao Wu, Martin L. Dunn, and H. Jerry Qi. Sequential self-folding structures by 3d printed digital shape memory polymers. *Scientific Reports*, 5:13616, September 2015.

[64] Dan Raviv, Wei Zhao, Carrie McKnelly, Athina Papadopoulou, Achuta Kadambi, Boxin Shi, Shai Hirsch, Daniel Dikovsky, Michael Zyracki, Carlos Olguin, et al. Active printed materials for complex self-evolving deformations. *Scientific reports*, 4:7422, 2014.

[65] George J Simitses and Dewey H Hodges. *Fundamentals of structural stability*. Butterworth-Heinemann, 2006.

[66] Lia Kashdan, Carolyn Conner Seepersad, Michael Haberman, and Preston S. Wilson. Design, fabrication, and evaluation of negative stiffness elements using sls. *Rapid Prototyping Journal*, 18(3):194–200, 2012.

[67] David L. Platus. Negative-stiffness-mechanism vibration isolation systems, 1999.

[68] J. Prasad and A. R. Diaz. Synthesis of bistable periodic structures using topology optimization and a genetic algorithm. *Journal of Mechanical Design*, 128(6):1298–1306, December 2005.

[69] Jin Qiu, Jeffrey H Lang, and Alexander H Slocum. A curved-beam bistable mechanism. *Journal of Microelectromechanical Systems*, 13(2):137–146, 2004.

[70] Y. C. Wang and R. S. Lakes. Extreme stiffness systems due to negative stiffness elements. *American Journal of Physics*, 72(1):40–50, 2004.

[71] Ahmad Rafsanjani, Abdolhamid Akbarzadeh, and Damiano Pasini. Snapping mechanical metamaterials under tension. *Advanced Materials*, 2015.

[72] Z Wu, RL Harne, and KW Wang. Exploring a modular adaptive metastructure concept inspired by muscleŠs cross-bridge. *Journal of Intelligent Material Systems and Structures*, 27(9):1189–1202, 2016.

[73] Mahmoud I Hussein, Michael J Leamy, and Massimo Ruzzene. Dynamics of phononic materials and structures: Historical origins, recent progress, and future outlook. *Applied Mechanics Reviews*, 66(4):040802, 2014.

[74] Filippo Casadei, Tommaso Delpero, Andrea Bergamini, Paolo Ermanni, and Massimo Ruzzene. Piezoelectric resonator arrays for tunable acoustic waveguides and metamaterials. *Journal of Applied Physics*, 112(6):064902, 2012.

[75] Raj Kumar Pal, Julian Rimoli, and Massimo Ruzzene. Effect of large deformation preloads on the wave properties of hexagonal lattices. *Smart Materials and Structures*, 25(5):054010, 2016.

[76] Neel Nadkarni, Chiara Daraio, and Dennis M Kochmann. Dynamics of periodic mechanical structures containing bistable elastic elements: From elastic to solitary wave propagation. *Physical Review E*, 90(2):023204, 2014.

[77] Jordan R. Raney, Neel Nadkarni, Chiara Daraio, Dennis M. Kochmann, Jennifer A. Lewis, and Katia Bertoldi. Stable propagation of mechanical signals in soft media using stored elastic energy. *Proceedings of the National Academy of Sciences*, 113(35):9722–9727, 2016.

[78] Michael J. Frazier and Dennis M. Kochmann. Band gap transmission in periodic bistable mechanical systems. *Journal of Sound and Vibration*, 388:315 – 326, 2017.

[79] Benjamin M. Goldsberry and Michael R. Haberman. Negative stiffness honeycombs as tunable elastic metamaterials. *Journal of Applied Physics*, 123(9):091711, 2018.

[80] Neel Nadkarni, Andres F. Arrieta, Christopher Chong, Dennis M. Kochmann, and Chiara Daraio. Unidirectional transition waves in bistable lattices. *Phys. Rev. Lett.*, 116:244501, Jun 2016.

[81] JJ Aklonis. Mechanical properties of polymers, 1981.

[82] Roderic Lakes. *Viscoelastic Materials*. Cambridge University Press, 2009.

[83] Jiangtao Wu, Chao Yuan, Zhen Ding, Michael Isakov, Yiqi Mao, Tiejun Wang, Martin L Dunn, and H Jerry Qi. Multi-shape active composites by 3d printing of digital shape memory polymers. *Scientific Reports*, 6:24224, 2016.

[84] Yin Fang, Yongliang Ni, Sin-Yen Leo, Curtis Taylor, Vito Basile, and Peng Jiang. Reconfigurable photonic crystals enabled by pressure-responsive shape-memory polymers. *Nature Communications*, 6:7416, June 2015.

[85] Andreas Lendlein, Hongyan Jiang, Oliver Jnger, and Robert Langer. Light-induced shape-memory polymers. *Nature*, 434:879, April 2005.

[86] R. Mohr, K. Kratz, T. Weigel, M. Lucka-Gabor, M. Moneke, and A. Lendlein. Initiation of shape-memory effect by inductive heating of magnetic nanoparticles in thermoplastic polymers. *Proceedings of the National Academy of Sciences*, 103(10):3540–3545, 2006.

[87] Tian Chen, Osama R Bilal, Kristina Shea, and Chiara Daraio. Harnessing bistability for directional propulsion of soft, untethered robots. *Proceedings of the National Academy of Sciences*, page 201800386, 2018.

[88] Andreas Lendlein and Robert Langer. Biodegradable, elastic shape-memory polymers for potential biomedical applications. *Science*, 296(5573):1673–1676, 2002.

[89] Yakacki Christopher M., Shandas Robin, Safranski David, Ortega Alicia M., Sassaman Katie, and Gall Ken. Strong, tailored, biocompatible shape-memory polymer networks. *Advanced Functional Materials*, 18(16):2428–2435, 2008.

[90] Yves Gnanou and Michel Fontanille. *Organic and physical chemistry of polymers*. John Wiley & Sons, 2008.

[91] A Brinkmeyer, M Santer, A Pirrera, and PM Weaver. Pseudo-bistable self-actuated domes for morphing applications. *International Journal of Solids and Structures*, 49(9):1077–1087, 2012.

[92] R Huang and Z Suo. Instability of a compressed elastic film on a viscous layer. *International Journal of Solids and Structures*, 39(7):1791–1802, 2002.

[93] R Huang and Z Suo. Wrinkling of a compressed elastic film on a viscous layer. *Journal of Applied Physics*, 91(3):1135–1142, 2002.

[94] Kashyap Alur and Julien Meaud. Nonlinear mechanics of non-dilute viscoelastic layered composites. *International Journal of Solids and Structures*, 72:130–143, 2015.

[95] Kashyap Alur, Thomas Bowling, and Julien Meaud. Finite-element analysis of rate-dependent buckling and postbuckling of viscoelastic-layered composites. *Journal of Applied Mechanics*, 83(3):031005, 2016.

[96] Viacheslav Slesarenko and Stephan Rudykh. Harnessing viscoelasticity and instabilities for tuning wavy patterns in soft layered composites. *Soft matter*, 12(16):3677–3682, 2016.

[97] Michael Smith. *ABAQUS/Standard User's Manual, Version 6.9*. Simulia, 2009.

[98] R Christensen. *Theory of viscoelasticity: an introduction; 2nd ed.* Academic Press, New York, 1982.

[99] Malcolm L Williams, Robert F Landel, and John D Ferry. The temperature dependence of relaxation mechanisms in amorphous polymers and other glass-forming liquids. *Journal of the American Chemical society*, 77(14):3701–3707, 1955.

[100] Kai Ming Yu, Qi Ge, and Hang Jerry Qi. Reduced time as a unified parameter determining fixity and free recovery of shape memory polymers. *Nature communications*, 5:3066, 2014.

[101] Alfio Quarteroni, Riccardo Sacco, and Fausto Saleri. *Numerical Mathematics (Texts in Applied Mathematics)*. Springer-Verlag, Berlin, Heidelberg, 2006.

[102] Michael W Barclift and Christopher B Williams. Examining variability in the mechanical properties of parts manufactured via polyjet direct 3d printing. In *International Solid Freeform Fabrication Symposium, August*, pages 6–8, 2012.

[103] MN Islam, Brian Boswell, and Alokesh Pramanik. An investigation of dimensional accuracy of parts produced by three-dimensional printing. In *Proceedings of the World Congress on Engineering*, volume 1, pages 3–5, 2013.

[104] R Udroiu and L Mihail. Experimental determination of surface roughness of parts obtained by rapid prototyping. In *8th WSEAS International Conference on Circuits, Systems, Electronics, Control and Signal Processing, Puerto De La Cruz, Tenerife, Canary Islands, Spain*, pages 283–286, 2009.

[105] Kaikai Che, Chao Yuan, Jiangtao Wu, H Jerry Qi, and Julien Meaud. Three-dimensional-printed multistable mechanical metamaterials with a deterministic deformation sequence. *Journal of Applied Mechanics*, 84(1):011004, 2017.

[106] Young Seok Oh and Sridhar Kota. Synthesis of multistable equilibrium compliant mechanisms using combinations of bistable mechanisms. *Journal of Mechanical Design*, 131(2):021002, 2009.

[107] Johannes TB Overvelde, Tamara Kloek, Jonas JA D'haen, and Katia Bertoldi. Amplifying the response of soft actuators by harnessing snap-through instabilities. *Proceedings of the National Academy of Sciences*, 112(35):10863–10868, 2015.

[108] Kaikai Che, Chao Yuan, H Jerry Qi, and Julien Meaud. Viscoelastic multistable architected materials with temperature-dependent snapping sequence. *Soft matter*, 14(13):2492–2499, March 2018.

[109] David Restrepo, Nilesh D Mankame, and Pablo D Zavattieri. Programmable materials based on periodic cellular solids. part i: Experiments. *International Journal of Solids and Structures*, 100:485–504, 2016.

[110] David Restrepo, Nilesh D Mankame, and Pablo D Zavattieri. Programmable materials based on periodic cellular solids. part ii: Numerical analysis. *International Journal of Solids and Structures*, 100:505–522, 2016.